IN SILICO DETERMINATION OF SARS-COV-2 E-PROTEIN INHIBITORS AND *IN VITRO* VALIDATION OF ANTIVIRAL ACTIVITY OF VARIOUS COMPOUNDS ON A MODEL CORONAVIRUS

Nina Kobe

Doctoral Dissertation
Jožef Stefan International Postgraduate School
Ljubljana, Slovenia

Supervisor: Dr. Polona Kogovšek, IPS and National Institute of Biology, Ljubljana, Slovenia

Evaluation Board:
Asst. Prof. David Dobnik, Chair, IPS and National Institute of Biology, Ljubljana, Slovenia
Asst. Prof. Andrej Steyer, Member, National Laboratory of Health, Environment and Food, Ljubljana, Slovenia
Prof. Dr. Igor Jurak, Member, Department of Biotechnology, University of Rijeka, Rijeka, Croatia

MEDNARODNA PODIPLOMSKA ŠOLA JOŽEFA STEFANA
JOŽEF STEFAN INTERNATIONAL POSTGRADUATE SCHOOL



Nina Kobe

IN SILICO DETERMINATION OF SARS-COV-2 E-PROTEIN INHIBITORS AND *IN VITRO* VALIDATION OF ANTIVIRAL ACTIVITY OF VARIOUS COMPOUNDS ON A MODEL CORONAVIRUS

Doctoral Dissertation

IN SILICO DOLOČITEV INHIBITORJEV SARS-COV-2 E-PROTEINA IN *IN VITRO* PREVERJANJE PROTIVIRUSNEGA DELOVANJA RAZLIČNIH SPOJIN NA MODELNEM KORONAVIRUSU

Doktorska disertacija

Supervisor: Dr. Polona Kogovšek

Ljubljana, Slovenia, May 2026

Acknowledgments

This work would not have been possible without the cooperation of many excellent researchers from various disciplines and institutions: the National Institute of Biology, Faculty of Chemistry and Chemical Technology Ljubljana, National Institute of Chemistry, Veterinary Faculty Ljubljana, Faculty of Biotechnology Ljubljana, Faculty of Health Sciences Primorska, and the International Centre for Genetic Engineering and Biotechnology (ICGEB).

I want to thank my supervisor, Polona Kogovšek, for accepting me as a PhD student and for her support in developing and realising my ideas and plans.

I would also like to thank many other collaborators: firstly, Lennart Dreisewerd, with whom I built a network that made this work possible, and for his constant support and the broad chemical knowledge he generously shared with me; Miha Lukšič, who supported and guided us, making challenges much more manageable; Magda Tušek Žnidarič, who was a skilled and inspiring teacher in TEM; Uroš Grošelj and Črtomir Podlipnik for their valuable help and support; the Italian team, for welcoming me into the group; Peter Hostnik and Urška Kuhar for introducing me to virology; Katja Kramberger and Darja Barlič-Maganja for sharing their valuable expertise on *Helichrysum italicum*; and the GEN department at NIB for their expert advice and support in cellular research. I am also grateful to my colleagues at NIB for their support, collaboration, and assistance throughout my work.

Lastly, I would like to thank my mother and friends for their support and encouragement; without them, this work would have been nearly impossible.

This research was funded by the Slovenian Research and Innovation Agency (research core funding Nos. P4-0463), the Erasmus+ Programme of the European Union (2023-1-SI01-KA131-HED-000122972), and the young researcher's programme. An AI-assisted language editing tool (Grammarly) was used solely for grammar correction and language refinement, and I retain full responsibility for the content of this dissertation.

Abstract

The emergence of SARS-CoV-2 variants underscores the need for antiviral strategies targeting conserved viral components. The SARS-CoV-2 envelope protein (Epro), a viroporin essential for viral assembly and release, represents a promising yet underexplored target. This doctoral research integrates computational modelling and experimental characterisation to identify novel Epro inhibitors and explore the antiviral potential of natural products.

A structure-based drug discovery platform was employed, including high-throughput virtual screening (HTVS) of nearly one billion compounds from the ZINC15 database, followed by molecular dynamics simulations, and molecular mechanics Poisson–Boltzmann surface area (MM-PBSA) analysis. Among the prioritised candidates, two of the eight candidates blocked the SARS-CoV-2 Epro ion channel for extended periods by forming hydrogen bonds with the amino acid residues GLU8, THR9, THR11, LEU12, and ASN15 within the N-terminal vestibule. However, *in vitro* testing of six structurally related, commercially available analogues showed no antiviral activity against a coronavirus surrogate, murine hepatitis virus (MHV), highlighting the importance of experimental validation.

Subsequently, a novel lead candidate (LC), (*S*)-*N*-(2-((1*S*,3*S*,5*S*,7*S*)-adamantan-2-yl)ethyl)-2-(butylamino)-3-(1*H*-indol-3-yl)propenamide, was identified from the Faculty of Chemistry and Chemical Technology (FKKT) compound library. It showed the highest predicted binding affinity and stable interactions within the N-terminal vestibule of Epro, forming hydrogen bonds with amino acid residues GLU8, THR11, ASN15, and LEU18. *In vitro* assays, including plaque reduction assays, qPCR, light microscopy, and transmission electron microscopy, confirmed potent antiviral activity against MHV by reducing viral infectivity, delaying RNA replication, and impairing virion egress, consistent with disruption of Epro function. These findings validate Epro as a viable antiviral target and support LC as a promising lead candidate.

In parallel, investigations into the antiviral activity of *Helichrysum italicum* revealed that the ethanolic extract exhibited strong selective activity against enveloped viruses, while no effect was observed against a non-enveloped virus. Chemical analysis by HPLC-MS/MS showed a phenolic-rich composition, and *in vitro* experiments confirmed that quercetin contributes to antiviral activity by acting at the entry stages of the viral life cycle. However, the overall effect most likely results from synergistic interactions between multiple constituents.

In conclusion, this doctoral thesis demonstrates the importance of integrating computational and experimental approaches in antiviral research and highlights the complementary potential of synthetic compounds and natural products. These findings contribute to the development of new antiviral strategies targeting conserved viral targets.

Povzetek

Pojav novih različic virusa SARS-CoV-2 poudarja potrebo po protivirusnih strategijah, usmerjenih proti ohranjenim virusnim komponentam. Ovojni protein E (Epro), viroporin, ki je ključen za sestavljanje in sproščanje virusnih delcev, predstavlja obetavno, vendar premalo raziskano tarčo. To doktorsko delo združuje računalniško modeliranje in eksperimentalno validacijo z namenom karakterizacije novih inhibitorjev Epro ter raziskovanja protivirusnega potenciala naravnih produktov.

Uporabljena je bila platforma za določanje in preverjanje učinkovin na osnovi strukture tarče, ki je vključevala visokozmogljivo virtualno presejanje (HTVS) skoraj ene milijarde spojin, sledilo pa je molekulsko sidranje, simulacije molekulske dinamike in analiza MM-PBSA. Med prednostno izbranimi kandidati sta dve spojini pokazali stabilno vezavo na ključne aminokislinske ostanke (GLU8, THR9, THR11, LEU12 in ASN15) znotraj N-terminalnega vestibula Epro. Vendar *in vitro* testiranje strukturno sorodnih, komercialno dostopnih analogov ni pokazalo protivirusne aktivnosti proti koronavirusnemu modelnemu virusu, virusu mišjega hepatitisa (MHV), kar poudarja pomen eksperimentalne validacije.

Nadalje je bila iz knjižnice spojin FKKT identificirana nova vodilna kandidatna spojina (LC), (*S*)-*N*-(2-((1*S*,3*S*,5*S*,7*S*)-adamantan-2-il)etil)-2-(butilamino)-3-(1*H*-indol-3-il)propenamid, ki je pokazala najvišjo afiniteto vezave ter stabilne interakcije znotraj N-terminalnega vestibula Epro z aminokislinskimi ostanki GLU8, THR11, ASN15 in LEU18. *In vitro* testiranja, vključno s testi redukcije plakov, qPCR, svetlobno mikroskopijo in transmisijsko elektronsko mikroskopijo, so potrdila protivirusno delovanje proti MHV. Spojina je omejila širjenje virusa izven okuženih celic in upočasnila pomnoževanje RNA, kar je skladno z motnjo delovanja Epro. Ti rezultati potrjujejo Epro kot ustrezno protivirusno tarčo in podpirajo LC kot obetavno spojino.

Vzporedno so raziskave protivirusnega delovanja rastline laški smilj, *Helichrysum italicum*, pokazale, da je etanolni ekstrakt izkazoval močno selektivno aktivnost proti virusom z ovojnico, medtem ko pri virusu brez ovojnice učinka ni bilo. Analiza HPLC-MS/MS je pokazala kemično sestavo, bogato s fenolnimi spojinami, pri čemer je med testiranimi spojinami k protivirusnemu delovanju prispeval kvercetin, ki je deloval v zgodnjih fazah virusnega cikla; celoten učinek izvlečka pa najverjetneje izhaja iz sinergističnih interakcij številnih spojin.

Doktorsko delo prikazuje pomen povezovanja računalniških in eksperimentalnih pristopov v protivirusnih raziskavah ter poudarja komplementarni potencial sintetičnih spojin in naravnih produktov. Ugotovitve prispevajo k razvoju novih protivirusnih strategij, usmerjenih proti ohranjenim virusnim tarčam.

Contents

List of Figures **xv**

List of Tables **xvii**

Abbreviations **xix**

Symbols **xxi**

1 Introduction **1**

1.1 The Challenge of SARS-CoV-2 and Antiviral Therapeutics 1

1.2 SARS-CoV-2 Envelope Protein 2

1.2.1 Integration of *in silico* and *in vitro* approaches in antiviral drug discovery 5

1.3 *Helichrysum italicum* 6

1.3.1 Botanical description of *Helichrysum italicum* 6

1.3.2 Medicinal use of *Helichrysum italicum* 7

1.3.3 Bioactive compounds in *Helichrysum italicum* extracts 8

1.3.4 Biological activities of *Helichrysum italicum* 10

1.4 Research Hypothesis 12

2 Materials and Methods **15**

2.1 Cultivation of Cells and Propagation of Viruses 15

2.1.1 L929 cell line 15

2.1.2 RAW 264.7 cell line 15

2.1.3 Vero E6 cell line 16

2.1.4 Seeding, subculturing, and maintaining cells 16

2.1.5 Murine hepatitis virus 17

2.1.6 Murine norovirus 17

2.1.7 Vesicular stomatitis virus 18

2.1.8 Virus propagation 18

2.2 Plant Material 19

2.3 Extracts and Compounds 19
2.4 Cytotoxicity Assay 21
2.5 Virological Methods 22
2.5.1 Determination of virus concentration using the endpoint dilution assay 22
2.5.2 Time-of-addition experiment 22
2.5.3 Plaque reduction assay 23
2.6 Tentative Identification of Phenolic Compounds by Mass Spectrometry 24
2.7 Light Microscopy and Transmission Electron Microscopy 24
2.8 qPCR and Digital PCR 24
2.8.1 Experimental set-up 24
2.8.2 RNA extraction and qPCR analysis 25
2.8.3 Data analysis 25
2.8.4 Droplet digital PCR (ddPCR) 26
2.9 Statistical Analyses 26
2.10 Computational Techniques 26
2.10.1 Candidate sourcing and databases 26
2.10.2 Molecular docking 27
2.10.3 Chemical space investigation and filtering 27
2.10.4 Molecular dynamics simulations 28

3 Results **29**

3.1 *In silico* Characterisation of the Candidates 29
3.1.1 Search for candidates from the ZINC15 database 29
3.1.2 Search for candidates from the FKKTLib 33
3.2 *In vitro* Characterisation of the Antiviral Activity of Candidate Compounds ... 36
3.2.1 Characterisation of candidates from the ZINC15 database 36
3.2.2 Characterisation of the lead candidate from the FKKTLib 36
3.2.3 Characterisation of *Helichrysum italicum* extract and active constituents 43

4 Discussion **49**

4.1 Characterisation of Antiviral Candidates 49
4.1.1 The ZINC15 database 50
4.1.2 FKKTLib 50

4.1.3 Antiviral potential of *Helichrysum italicum* 53

5 Conclusions **57**

Appendix A **59**

A.1 Supplementary Material for Section 2.3 59

A.2 Supplementary Material for Section 3.1.1 60

A.3 Supplementary Material for Section 3.1.2 64

A.4 Supplementary Material for Section 3.2.3.4 66

References **69**

Bibliography **89**

Publications Related to the Thesis 89

Journal Articles 89

Other Publications 89

Biography **91**

List of Figures

Figure 1: Structural proteins and intracellular localisation of the SARS-CoV-2 envelope protein (Epro)……2

Figure 2: Sequence and structural features of the SARS-CoV-2 envelope protein (Epro) ion channel……3

Figure 3: *Helichrysum italicum* growing in nature in a flowering phase.....7

Figure 4: Dried inflorescences of *Helichrysum italicum*.....8

Figure 5: Structures of the tested phenolic compounds.....20

Figure 6: Chemical structure of the lead candidate (LC).....21

Figure 7: Time-of-addition experiments scheme.....23

Figure 8: Chemical space analysis and lead compounds selection.....30

Figure 9: Binding poses and hydrogen-bond interactions of selected lead compounds. 32

Figure 10: Most representative clusters depicting hydrogen-bond interactions and binding poses……35

Figure 11: Antiviral activity and effect on viral replication of LC, HMA, and RMT.....38

Figure 12: Light microscopy of semi-thin sections.....39

Figure 13: Ultrastructural analysis of MHV infection in L929 cells by transmission electron microscopy (TEM)……41

Figure 14: Ultrastructural comparison of LC-treated infected and uninfected L929 cells by transmission electron microscopy (TEM).....42

Figure 15: Virus particles in MHV-infected L929 cells visualised by transmission electron microscopy (TEM), with or without LC.....43

Figure 16: Antiviral activity of the ethanolic extract against MHV and VSV. 45

Figure 17: Effect of the ethanolic extract on MHV RNA levels. 46

List of Tables

Table 1: SARS-CoV-2 E protein inhibitors confirmed by *in vitro* studies. 5

Table 2: Tested synthetic and reference compounds. 21

Table 3: MM-PBSA total binding free energies ($\Delta Gbind$) of SARS-CoV-2 Epro–ligand complexes..... 33

Table 4: Total binding free energies ($\Delta Gbind$) and duration of the MD simulation..... 34

Table 5: Dose-response results of the tested compounds in L929 cells infected with MHV..... 37

Table 6: Viral particle counts in infected untreated and LC-treated L929 cells (TEM)... 42

Table 7: Extract and compounds tested against enveloped and non-enveloped viruses. .. 44

Abbreviations

AMT	...	amantadine
ATCC	...	American Type Culture Collection
β-CoV	...	*Betacoronavirus*
BLS-2	...	biosafety level 2
CC_{50}	...	half-maximal cytotoxic concentration
CCK-8	...	Cell Counting Kit-8
CGA	...	chlorogenic acid
CoV	...	coronavirus
COVID-19	...	coronavirus disease 2019
CQA	...	caffeoylquinic acid
CTD	...	C-terminal domain
DMEM	...	Dulbecco's Modified Eagle Medium
EC_{50}	...	half-maximal effective concentration
EMEM	...	Eagle's Minimum Essential Medium
EO	...	essential oil
Epro	...	envelope protein
ER	...	endoplasmic reticulum
ERGIC	...	ER–Golgi intermediate compartment
FKKTLib	...	FKKT compound library
HIV-1	...	human immunodeficiency virus type 1
HMA	...	5-(*N*,*N*-hexamethylene)amiloride
HPLC	...	high-performance liquid chromatography
HSV-1	...	herpes simplex virus type 1
IAV	...	influenza A virus
LC	...	lead candidate
LO	...	lipoxygenase
MD	...	molecular dynamics
MM-PBSA	...	molecular mechanics Poisson–Boltzmann surface area
MNV	...	murine norovirus
MOI	...	multiplicity of infection
M2	...	matrix protein 2
NTD	...	N-terminal domain
NFκB	...	nuclear factor kappa-light-chain-enhancer of activated B cells
PALS-1	...	protein associated with LIN7-1
POPC	...	1-palmitoyl-2-oleoylphosphatidylcholine
RMSD	...	root mean square deviations
RMT	...	rimantadine
SARS-CoV-1	...	severe acute respiratory syndrome coronavirus 1
SARS-CoV-2	...	severe acute respiratory syndrome coronavirus 2
SI	...	selectivity index

SPR	...	surface plasmon resonance
$TCID_{50}$	...	50% tissue culture infective dose
TEM	...	transmission electron microscopy
TMD	...	transmembrane domain
TNF	...	tumour necrosis factor
VpU	...	viral protein U
VSV	...	vesicular stomatitis virus

Symbols

ΔG_{bind}^{res}	...	binding free energy of an individual protein residue
ΔG_{bind}	...	total binding free energy

Chapter 1

Introduction

1.1 The Challenge of SARS-CoV-2 and Antiviral Therapeutics

Viruses are the most abundant biological entities on Earth, a kind of "nanoparticle" in nature. They are everywhere, in our environment, the oceans, the soil, the air, and in every living thing. Viruses are infectious agents that are not cells, consist of DNA or RNA, in a protein coat, and can direct their reproduction and spread by co-opting the machinery inside the host cell they invade [1]. They come in a variety of sizes and shapes, from the smallest, measuring 17 nm, to the largest, discovered at 1,500 nm. Depending on the presence of an envelope, viruses may be enveloped or non-enveloped, also called "naked viruses" (e.g., poliovirus or norovirus) [2]. Viral envelopes consist of phospholipid bilayers that resemble cellular membranes. The lipid components are entirely derived from the host, whereas the protein components are encoded by the virus. Most envelope proteins are integral glycoproteins with essential roles in virus–host interactions. Like proteins on the outer surface of non-enveloped viruses, they serve as ligands for host receptors [3]. Enveloped viruses acquire their envelopes as they exit the host cell, which provides several advantages, including protection during budding and increased structural flexibility. However, this can also be detrimental to viral stability outside the host cell, as the lipid bilayer is susceptible to degradation under harsh physical or chemical conditions [4]. In contrast, non-enveloped viruses are generally more environmentally stable, more common in extreme environments, and more resistant to detergents, disinfectants, and heat [5]. Although human-to-human transmission is more likely with non-enveloped viruses, most viral epidemics in recent years, such as Ebola, measles, Zika, and coronavirus disease 2019 (COVID-19), have been caused by enveloped viruses [6], [7].

The global outbreak of COVID-19, caused by severe acute respiratory syndrome coronavirus 2 (SARS-CoV-2), was the most recent pandemic. In response, significant progress has been made in understanding the virus's pathogenesis, leading to the development of second- and third-generation vaccines and targeted small-molecule antivirals. These measures were initially effective in both the prevention and treatment of COVID-19. However, the emergence of the Omicron variant, which is characterised by numerous mutations, particularly in the spike protein, has compromised vaccine-induced immunity [8]. Several clinically approved antivirals are available for treating COVID-19; however, their effectiveness varies depending on factors such as timing of administration

and patient-specific variables [9], [10]. Remdesivir and molnupiravir are nucleoside analogue inhibitors targeting the viral RNA-dependent RNA polymerase (RdRp), thereby blocking viral replication [11]. Although remdesivir is restricted to hospitalised patients, its clinical efficacy remains a subject of debate, and recent studies have reported cases of resistance in immunocompromised patients receiving the drug [12], [13], [14], [15]. Molnupiravir increases mutations and is classified as a mutagen, making it unsuitable for use during pregnancy [16], [17]. Additionally, its potential toxicity to bone and cartilage limits its use in patients under the age of 18 [17]. Ritonavir-boosted nirmatrelvir, a main protease inhibitor, provides protection only when administered within 5 days of symptom onset. However, its use is complicated by drug-drug interactions, and a study by Duan *et al.* has identified several potential mutation sites that could enable SARS-CoV-2 to develop resistance to nirmatrelvir [18], [19]. Developing new antiviral strategies and identifying novel compounds is crucial to controlling viral replication, limiting transmission, and preventing resistance over the long term.

1.2 SARS-CoV-2 Envelope Protein

The genome of SARS-CoV-2 encodes four main structural proteins: spike (S), nucleocapsid (N), membrane (M), and envelope (E) protein (Figure 1A) [20]. Despite being the smallest with only 75 amino acids, E protein (Epro) plays a crucial role in the viral life cycle and is remarkably well conserved among all variants [21]. Comparative analyses show that the Epro has the lowest mutation rate among the structural proteins and exhibits a high degree of sequence conservation between SARS-CoV-1 and SARS-CoV-2, which share ~80% sequence identity [22]. It is noteworthy that their envelope proteins have only minor deviations in the amino acid sequence (Figure 2A) [21], [23], [24], [25].

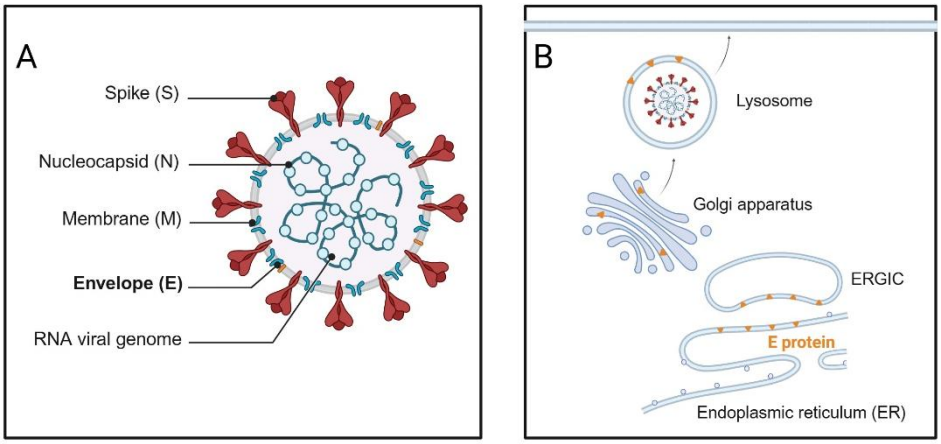


Figure 1: Structural proteins and intracellular localisation of the SARS-CoV-2 envelope protein (Epro). **(A)** The four structural proteins of SARS-CoV-2 are spike (S), membrane (M), nucleocapsid (N), and envelope (E). **(B)** Intracellular localisation of Epro viroporins in endoplasmic reticulum (ER), ER-Golgi intermediate compartment (ERGIC), Golgi apparatus, and lysosomes (marked with orange). The image was created with BioRender.com.

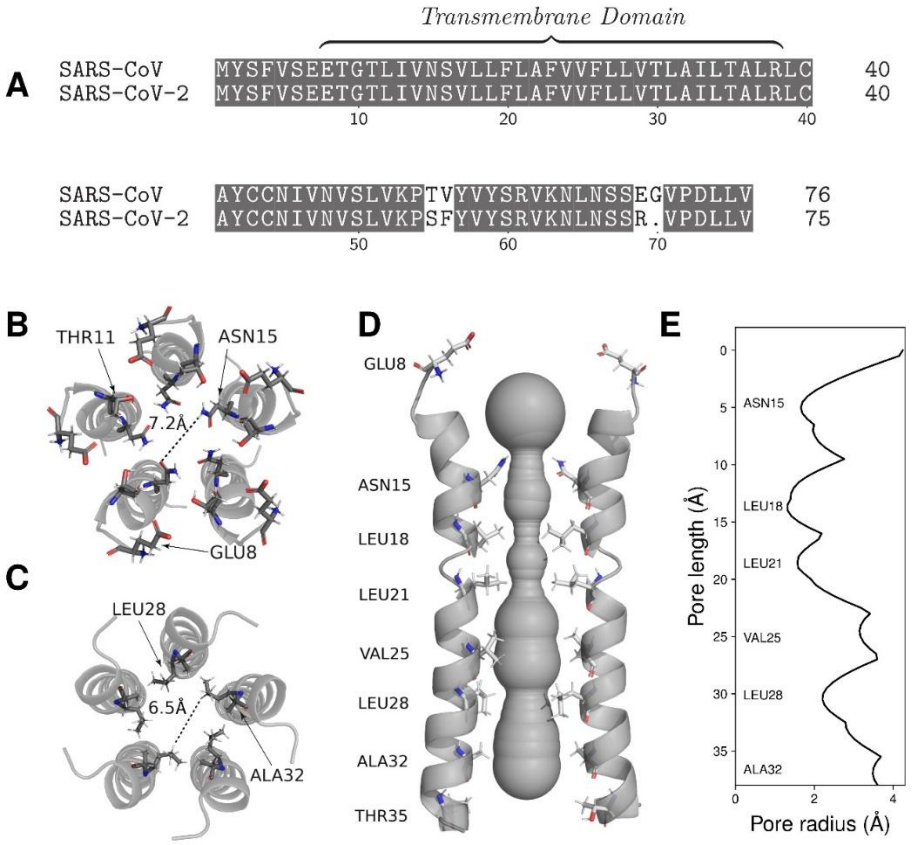


Figure 2: Sequence and structural features of the SARS-CoV-2 envelope protein (Epro) ion channel. **(A)** Sequence alignment of the SARS-CoV and SARS-CoV-2 Epros, respectively. Identical amino acids are highlighted in grey. **(B)** Transversal view onto the N-termini of the transmembrane domain of the Epro ion channel (PDB ID 7k3g) [26]. For each subunit, the amino acid residues of GLU8, THR11, and ASN15 are displayed, representing a relevant region for inhibitor binding and ion selectivity of the N-terminal vestibule. **(C)** Transversal view onto the C-termini of the Epro ion channel. For each subunit, LEU28 and ALA32 residues are displayed, which are inward-facing and channel-constricting amino acids. **(D)** Cross-sectional view of SARS-CoV-2 Epro showing the Caver 3.0-calculated volume of the ion channel, which extends along the longitudinal axis of the five SARS-CoV-2 Epro subunits, with amino acid residues listed on the left. **(E)** The pore radii along the longitudinal axis of the calculated volume of the ion channel [27].

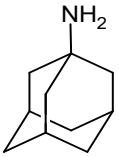
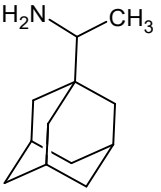
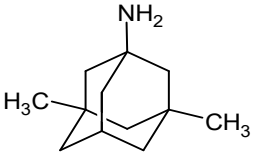
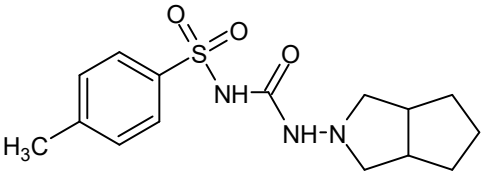
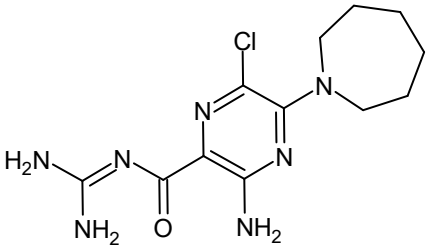
Structurally, Epro consists of three domains: a short, hydrophilic N-terminal domain (NTD), a central, hydrophobic transmembrane domain (TMD), and a longer, hydrophilic C-terminal domain (CTD) [20]. Epro monomers oligomerise into homopentameric ion channels (so-called viroporins) which are cation-selective and cause ionic imbalances, disrupting pH gradients in host cells (Figure 2B, C) [26], [28], [29]. Intracellularly, Epro is predominantly localised in the endoplasmic reticulum (ER), the Golgi apparatus, and the ER-Golgi intermediate compartment (ERGIC) (Figure 1B). These organelles are essential for the assembly, maturation, and release of newly formed virions – processes in which Epro has been shown to play a crucial role [30], [31], [32], [33]. Recombinant coronaviruses (CoVs) lacking Epro have lower viral titres and produce incompetent progeny, indicating the functional importance of Epro in CoVs pathogenesis despite not being strictly essential for viral replication [31], [34], [35].

Inhibition of SARS-CoV-2 Epro with the channel inhibitor BE-33 in transgenic mice infected with SARS-CoV-2 resulted in a significant reduction in viral load and

inflammatory cytokine levels in the lung, demonstrating the complex role of SARS-CoV-2 Epro in viral replication and cellular damage [36]. These processes contribute to clinical manifestations such as cytokine storms, which can significantly worsen disease progression and patient outcomes [36], [37], [38]. Other SARS-CoV-2 symptoms, extending beyond respiratory issues, such as neurological manifestations, have been linked to Epro expression, which promotes proliferation and inflammation in glioblastoma cells [39]. In addition, SARS-CoV-2 Epro has been shown to strongly upregulate tumour necrosis factor (TNF) production, a key cytokine predictive of COVID-19 severity and mortality [40]. Overexpression of TNF has been associated with taste disorders [41], suggesting that SARS-CoV-2 Epro may be a major contributing factor. Furthermore, its expression was found to play a crucial role in regulating metabolic activity and inducing ER stress by altering ER Ca^{2+} homeostasis, thereby affecting cellular repair mechanisms and homeostasis of most human tissues and organs [42]. Epro interacts with protein associated with LIN7-1 (PALS1), a tight junction-associated protein critical for maintaining epithelial polarity [43], [44]. This interaction has been linked to disruption of epithelial integrity in the lungs, contributing to enhanced inflammation and epithelial cell damage during infection [45], [46].

The functional significance of viral ion channels as antiviral targets is well documented for several RNA viruses, e.g., influenza A virus (IAV) and human immunodeficiency virus-1 (HIV-1), which express the matrix protein 2 (M2) and viral protein U (VpU) ion channels, respectively. Herein, the M2 and VpU ion channel activities are closely linked to key phases of the viral life cycle, as demonstrated by mutational studies and channel-blocking compounds [47], [48], [49], [50]. Similar findings have been obtained for the CoV Epro, for which inhibition of its viroporin activity has proven a promising antiviral strategy. Several *in silico* and *in vitro* drug-screening and NMR studies have identified a relevant ligand-binding region within the alpha-helical pentameric channel, providing a viable target for cation flow obstruction [26], [51], [52]. This region can be roughly localised to protein residues 15–32, which represent a hydrophobic, in-diameter-constricted stretch of the channel (Figure 2B–E). A small set of ligands including 5-(*N*,*N*-hexamethylene)amiloride (HMA) [53], [54], [55], [56], amantadine (AMT) [21], [57], [58], and rimantadine (RMT) [21], [58], [59], have been found to bind at or near this region. They have also shown beneficial effects in infected cells, as demonstrated by surface plasmon resonance (SPR), antiviral efficacy assays [52], and patch-clamp electrophysiology [59]. However, most Epro inhibitor candidates have been identified only through *in silico* studies [20], [60], and relatively few have been validated *in vitro* or *in vivo*, underscoring the importance of experimental exploration. An overview of SARS-CoV-2 Epro inhibitors confirmed *in vitro* is presented in Table 1. Each compound is listed alongside its chemical structure and proposed mechanism of action.

Table 1: SARS-CoV-2 E protein inhibitors confirmed by *in vitro* studies.

Name	Chemical structure	Potential mechanism
amantadine (AMT)		acting as a lysosomotropic agent and altering the Cathepsin L functional environment; inhibition of Epro and Orf10 ion channel activity [61], [62], [63], [64], [65]
rimantadine (RMT)		acting mainly at the viral post-entry level and partially at the viral entry level [59], [61]
memantine		inhibiting the release of the viral genome into the host cell cytoplasm, decreasing ACE2 receptor expression, and reducing oxidative stress and inflammation [61], [66], [67]
gliclazide		inhibiting the release of the viral genome into the host cell cytoplasm [66]
5-(*N*,*N*-hexamethylene)amiloride (HMA)		inhibiting ion channel opening, reducing viral replication, and virus-mediated inflammatory responses [59], [65], [68]

1.2.1 Integration of *in silico* and *in vitro* approaches in antiviral drug discovery

Effective antiviral development depends on integrating computational and experimental methods, particularly for challenging targets such as SARS-CoV-2 Epro. A defined workflow that combines structure-based discovery with biological validation enables rapid identification of promising molecules and confirmation of their antiviral efficacy and potential.

Building on the use of computational approaches in antiviral research, methods such as molecular docking, molecular dynamics (MD) simulations, pharmacophore modelling, quantitative structure-activity relationship (QSAR) modelling, and free energy calculations are now key tools in early-stage studies [69], [70], [71]. They help to quickly and efficiently screen millions of compounds, accelerating hit identification.

MD simulations and molecular mechanics Poisson–Boltzmann surface area (MM-PBSA) calculations represent an integrated workflow [72]. MD simulations reveal how protein–ligand complexes evolve, demonstrating their stability under conditions resembling

those in living systems. MM-PBSA calculations use these results to estimate binding free energies and rank new compounds before further laboratory testing.

Although computational methods facilitate early-stage discovery, predictive models alone are insufficient. Integrating computational predictions with experimental validation is necessary to address the complexity of biological systems. Computational models can overlook critical factors such as cellular uptake, solubility, metabolic stability, toxicity, off-target effects, and cellular interactions. For viroporin inhibitors, minor structural modifications can significantly alter antiviral activity, even when predicted binding affinities are similar. Research on SARS-CoV-2 Epro inhibitors has shown that compounds predicted to bind strongly to the ion channel do not necessarily exhibit antiviral activity in cell-based assays, as many reported inhibitors have been identified and prioritised solely through *in silico* studies without sufficient experimental validation [20]. Therefore, combining computational and experimental approaches is essential to establish biological relevance. Commonly employed *in vitro* techniques include plaque reduction assays, cytopathic effect (CPE) inhibition assays, quantitative polymerase chain reaction (qPCR), immunofluorescence, electrophysiological measurements, and transmission electron microscopy [21], [59], [73]. Time-of-addition experiments provide mechanistic insights by distinguishing compound activity at different stages of the viral life cycle, such as entry, replication, and release [74].

In addition to conventional antiviral drug discovery, natural product research benefits from integrating *in silico* and *in vitro* strategies. Plant-derived extracts are chemically complex mixtures, and their antiviral activity often results from synergistic interactions among multiple constituents rather than a single active compound [75], [76], [77]. While computational methods can predict potential molecular targets of individual phytochemicals, *in vitro* studies are essential to identify biologically relevant activity and clarify the contributions of complex extract compositions.

Taken together, the complementary use of *in silico* and *in vitro* methods constitutes an integrated, rational, and efficient workflow that provides a foundation for subsequent *in vivo* studies and accelerates the discovery of new treatments for urgent viral threats.

1.3 *Helichrysum italicum*

Medicinal plants have been used throughout history to improve human health and remain an important source of traditional remedies and modern pharmaceuticals [78]. Mediterranean plants are particularly rich in biologically active secondary metabolites produced in response to environmental stresses such as drought, high temperatures, salinity, and UV radiation [79]. These compounds, including antioxidant phenolic compounds, have important applications in medicine and industry and are abundant in plants such as *Helichrysum italicum* (immortelle).

1.3.1 Botanical description of *Helichrysum italicum*

Helichrysum italicum (Roth) G. Don is an aromatic Mediterranean plant widely recognised in traditional medicine, cosmetics, and Mediterranean cuisine [80], [81], [82]. The genus name *Helichrysum*, derived from the Greek *helios* (sun) and *chrysos* (gold), refers to its characteristic yellow, fade-resistant inflorescences, which are a known source of bioactive secondary metabolites. It belongs to the family Asteraceae (Compositae) and is an herbaceous perennial that grows as a semi-shrub, typically reaching 30–70 cm in height (Figure 3) [83]. The stem is woody at the base, and the leaves are arranged in a rosette,

with additional leaves spirally distributed along both vegetative and flowering stems. The leaves have numerous glandular trichomes, especially on the lower epidermis. At the top of the flowering stem, the plant forms a corymb-like inflorescence composed of multiple small capitula. It typically flowers from May to September, with peak flowering usually in June [84], [85].



Figure 3: *Helichrysum italicum* growing in nature in a flowering phase. Author of the photography, Nina Kobe.

The genus *Helichrysum* Mill. comprises approximately 600 species distributed worldwide, of which about 25 are native to the Mediterranean region. Among these, *Helichrysum italicum* is considered the most widespread species in this area [86]. In some regions, multiple subspecies occur together and spontaneously hybridise, further increasing plant diversity and complicating accurate taxonomic identification [84]. According to the current classification proposed by Herrando-Moraira *et al.* [87], *H. italicum* is divided into four subspecies:

- *H. italicum* ssp. *italicum* – the most widespread subspecies, occurring in Italy, Croatia, Slovenia, the French coast, Corsica, along the Adriatic coast, as well as on the Aegean islands and Cyprus.
- *H. italicum* ssp. *siculum* – endemic to Sicily.
- *H. italicum* ssp. *microphyllum* – endemic to Crete.
- *H. italicum* ssp. *tyrrhenicum* – found in southern Corsica, Sardinia, the coast of Mallorca, and the island of Dragonera.

1.3.2 Medicinal use of *Helichrysum italicum*

Helichrysum italicum has been used in traditional medicine and cosmetics [80]. The flowering tops are commonly used for their anti-inflammatory and anti-allergic properties

and are included in cosmetic preparations to treat sunburn and skin erythema [88], [89]. Decoctions made from the flowering tops have also been used for fumigation in the treatment of asthma [86]. The dried inflorescences of the plant have been used as a moth antifeedant (Figure 4) [88], [89].

The biological activities of *H. italicum* are mainly attributed to its essential oils (EOs), which are widely used in aromatherapy. Due to its cicatrizant properties, the EO is believed to promote skin regeneration and support wound healing. These regenerative effects have led to its widespread use in cosmetic formulations, particularly in anti-ageing creams and other skin care products containing *H. italicum* EO [86].



Figure 4: Dried inflorescences of *Helichrysum italicum*. Author of the photography, Nina Kobe.

1.3.3 Bioactive compounds in *Helichrysum italicum* extracts

The preparation of medicinal plants for research is a crucial step in obtaining reliable and reproducible results. This process involves the appropriate and timely harvesting of plant material, morphological identification and authentication by a qualified specialist, and subsequent drying and grinding before extraction. The extraction is then carried out, and the resulting extract may subsequently be fractionated to isolate individual bioactive compounds.

Plant extracts with complex chemical compositions are often preferred to isolated compounds, as they may enable synergistic interactions and polyvalent biological activity. In *H. italicum*, subspecies or genotype, as well as factors such as cultivation, harvest, drying, storage, and extraction procedures, can substantially influence chemical profiles and the quality of preparations, and consequently their biological effects [90], [91]. Among the major phytochemical classes, phenolic compounds are of particular interest due to their antioxidant properties and their potential role in infection- and inflammation-related processes [92], [93]. Reported phenolics include phenolic acids (hydroxybenzoic and hydroxycinnamic acids), coumarins, flavonoids, and related derivatives [92]. As phenolic compounds are more abundant in extracts obtained with organic solvents, terpenes are

typically characteristic of EO. Owing to this diverse chemical composition, *H. italicum* has been associated with a broad spectrum of biological activities [92].

1.3.3.1 Essential oils (EOs)

The EO of *H. italicum* is the most extensively studied plant product. It is generally obtained from the green aerial parts or the flowers by hydrodistillation or steam distillation [80], [92]. The EO consists predominantly of terpenes, particularly mono- and sesquiterpenes, while β-diketones (italidiones) represent another important group of compounds and are considered characteristic of *H. italicum* [3,22]. Major monoterpenes include α-pinene, limonene, nerol, neryl acetate, and neryl propanoate, whereas α- and β-selinene, γ-curcumene, and trans-β-caryophyllene are prominent sesquiterpenes [94], [95]. Despite the characteristic curry-like scent of the fresh plant, the essential oil itself often lacks this aroma [94], [96]. The compounds responsible for this scent are not fully understood, although curcumenes and 4,6-dimethyloctane-3,5-dione have been suggested to contribute to the curry-like odour [97].

1.3.3.2 Aqueous extracts

In addition to EOs, aqueous and organic solvent extracts of *H. italicum* have been widely investigated. Water extracts mainly contain polar phenolic compounds. Pereira *et al.* identified individual compounds present in infusions and decoctions of different *H. italicum* plant parts. Decoctions, particularly those prepared from flowers, contained higher levels of total phenolics, with chlorogenic, quinic, and dicaffeoylquinic acids, as well as the flavonoids pinocembrin and gnaphalin A, being the predominant constituents [98]. Kramberger *et al.* reported a similar composition, observing the predominance of caffeoylquinic acids and flavonoids, followed by pyrones. By comparison, extracts obtained by cold-water maceration with ultrasound contained primarily phenolic acids [99].

1.3.3.3 Organic solvent extracts

Among organic solvents, ethanol is one of the most used for extracting *H. italicum*. Early studies reported the isolation of various flavonoids from ethanolic extracts, including apigenin, luteolin, gnaphalin, and naringenin, together with their glycosides [88], [89]. Other studies identified hydroxycinnamic acids, such as caffeic, p-coumaric, and ferulic acid, and their derivatives, including caffeoylquinic and dicaffeoylquinic acids [100], [101].

Methanol extracts have also been extensively studied. Sala *et al.* isolated flavonoids such as pinocembrin, tiliroside, and gnaphalin, as well as acetophenone derivatives, which showed high biological activity [102], [103]. De La Garza *et al.* identified numerous phenolic acids and flavonoids, including gallic, caffeic, and chlorogenic acids, as well as naringenin and its glycosides, kaempferol derivatives, myricetin glycoside, methoxyluteolin, and epigallocatechin-3-O-gallate [104]. Mari *et al.* reported similar results, also detecting quercetin, kaempferol, and isorhamnetin glycosides, as well as drimane sesquiterpenes and gnaphaliol [105].

A characteristic compound of *H. italicum* is arzanol, a prenylated heterodimeric phloroglucinol α-pyrone, first isolated from an acetone extract [94]. Arzanol exhibits pleiotropic biological activity, and other pyrones such as helipyrone and micropyrone have also demonstrated biological effects [94], [106]. In addition to pyrones, acetone extracts contain various tremetones [94], [106]. Tagliatela-Scafati *et al.* further identified several less polar constituents, including neryl acetate, ω-oleoyloxylinalool, the triterpenoid ursolic acid, and a unique class of lipids known as santinols. Santinols are angeloylated glycerides with branched acyl or keto-acyl chains, representing a novel class of compounds isolated

exclusively from *H. italicum*, and were named in honour of Leonardo Santini, one of the pioneers in the study of this plant [107].

1.3.4 Biological activities of *Helichrysum italicum*

H. italicum is recognised as a rich source of phytochemicals with diverse biological activities. Numerous *in vitro* and *in vivo* studies have reported antioxidant, anti-inflammatory, antimicrobial, antiviral, and other pharmacological effects associated with different extracts and isolated compounds from this plant. These biological properties are primarily attributed to phenolic compounds, flavonoids, acetophenones, pyrones, and other secondary metabolites present in the plant tissues [80], [88], [92], [94], [100], [108], [109].

1.3.4.1 Antioxidant activity

The antioxidant potential of *H. italicum* extracts has been extensively investigated, mainly because the plant is rich in phenolic compounds known for their ability to neutralise reactive oxygen species. In contrast, EOs generally exhibit weaker antioxidant activity due to the limited presence of compounds containing electron-donating functional groups [92].

Dzamic *et al.* investigated extracts obtained from residual water after EO distillation. They found that the aqueous extract exhibited the strongest antioxidant activity, followed by the methanol extract, while the EO showed the weakest activity [110]. The aqueous extract also contained the highest concentration of total phenolic compounds, suggesting their contribution to antioxidant activity. Similar findings were reported by Kazazic *et al.*, who analysed aqueous extracts of several medicinal plants and observed that *H. italicum* possessed very high total phenolic contents and strong antioxidant activity [111].

Antioxidant activity has also been demonstrated for several isolated compounds from *H. italicum*. Studies on individual flavonoids revealed that tiliroside exhibited particularly strong antioxidant activity, significantly reducing enzymatic and non-enzymatic lipid peroxidation and achieving 50% inhibition of the 2,2-diphenyl-1-picrylhydrazyl (DPPH) radical [103]. Additionally, pyrones such as arzanol and helipyrone have been shown to prevent the oxidation of linoleic acid and protect cellular membranes from oxidative stress [106]. Arzanol has also been reported to inhibit the formation of cholesterol oxidation products and to protect low-density lipoproteins (LDL) from oxidative modification induced by copper ions [112].

Antioxidant and anti-inflammatory activities are often closely linked, as inflammatory processes are frequently associated with oxidative stress and lipid peroxidation. Consequently, the antioxidant properties of *H. italicum* extracts are thought to contribute significantly to their overall pharmacological effects.

1.3.4.2 Anti-inflammatory activity

Inflammation is a complex biological process involving the activation of different enzymes and signalling pathways. Several bioactive compounds isolated from *H. italicum* have been linked to anti-inflammatory activity. Arzanol's activity is primarily attributed to inhibition of key enzymes in inflammatory pathways, particularly microsomal prostaglandin E synthase (mPGES) [113]. mPGES, cyclooxygenase-1 and -2 (COX-1 and COX-2), and 5-lipoxygenase (5-LO), are involved in the synthesis of prostaglandins, thromboxanes, and leukotrienes, which are important mediators of inflammation [114]. In addition to enzyme inhibition, arzanol suppresses activation of the key transcription factor, nuclear factor kappa-light-chain-enhancer of activated B cells (NFκB) [94], [114], which regulates immune and inflammatory responses by promoting the expression of pro-inflammatory mediators,

including cytokines and chemokines [84], [115]. Furthermore, it has been reported to bind strongly to serum albumin and protect proteins from denaturation, providing an additional mechanism contributing to its anti-inflammatory activity [116].

Other phytochemicals present in *H. italicum* also contribute to the modulation of inflammatory pathways. The flavonoids gnafalin and pinocembrin, isolated from methanol extracts of *H. italicum*, inhibit the formation of the inflammatory mediator leukotriene B_4. Another compound, helipiron, has also been reported to inhibit NFκB activation, further supporting the role of multiple secondary metabolites in regulating inflammatory responses [94].

Phenolic acids such as chlorogenic and caffeic acids have demonstrated inhibitory effects on inflammatory mediators. For example, chlorogenic acid reduced COX-2 activity and decreased a prominent pro-inflammatory cytokine, tumour necrosis factor-α (TNF-α), production in lipopolysaccharide-stimulated RAW264.7 mouse macrophages [117], [118].

In addition to polar extracts, anti-inflammatory activity has also been reported for the EO of *H. italicum*. In BV-2 mouse microglial cells, EO showed a moderate inhibitory effect on 5-LO and arachidonic acid metabolism [119]. This activity is largely attributed to monoterpenes present in the EO, particularly α-pinene and limonene, both of which have demonstrated anti-inflammatory properties [120], [121].

Overall, the anti-inflammatory effects of *H. italicum* appear to result from the combined action of several classes of bioactive compounds that modulate inflammatory signalling pathways.

1.3.4.3 Antimicrobial activity

The antimicrobial activity of the EO of *H. italicum* has been extensively investigated. It has demonstrated activity, particularly against Gram-negative bacteria, largely due to its terpene constituents [122], [123], [124], [125], [126], [127]. For example, geraniol, one of the major EO components, has been shown to enhance antibiotic efficacy by inhibiting bacterial efflux pumps [126]. Furthermore, Nostro *et al.* reported that diethyl ether extracts inhibited the growth of several *Staphylococcus aureus* strains, including methicillin-resistant (MRSA) and methicillin-susceptible (MSSA) strains. Diethyl ether extracts also inhibited enzymes associated with bacterial virulence, including coagulase, DNase, thermonuclease, and lipase, and the antibacterial activity was attributed to the combined action of terpenes and flavonoids [128]. They also confirmed the antibacterial activity of ethanol extracts against *Streptococcus mutans*, a major causative agent of dental caries [129]. Methanol extracts exhibited the strongest activity against Gram-positive bacteria, particularly *Micrococcus luteus* [130]. Research on isolated constituents demonstrated that arzanol derivatives exhibited inhibitory effects against *S. aureus* isolates [107].

In addition to antibacterial activity, *H. italicum* extracts have shown antifungal properties. EO demonstrated activity against the *Candida albicans* and *Saccharomyces cerevisiae* yeasts [127], and methanol extracts were effective against the phytopathogenic fungus *Pythium ultimum* [130]. Furthermore, phloroglucinol and acetophenone derivatives isolated from *H. italicum* exhibited antifungal activity against several *Penicillium* species [131].

1.3.4.4 Antiviral activity

Although the pharmacology of *H. italicum* is relatively well studied [80], research on its antiviral activity remains scarce. Nostro *et al.* reported the activity of a diethyl ether extract from *H. italicum* against herpes simplex virus type 1 (HSV-1) at concentrations of 100–400 µg/mL [109], and ethanolic extracts of other *Helichrysum* species have exhibited variable activity against enveloped viruses, including HSV-1, parainfluenza virus type 3

(PIV-3), and IAV [132], [133], [134]. Several flavonoids commonly found in *H. italicum*, including quercetin, apigenin, and luteolin, have demonstrated anti-HSV activity, suggesting their contribution to the observed effects [75], [76], [77], [135], [136]. Arzanol, a characteristic phloroglucinol from *H. italicum*, has also been shown to inhibit human immunodeficiency virus type 1 (HIV-1) replication in T cells [94] and to exert anti-inflammatory and antioxidant effects [106], [112], [114], [137]. However, a comparative evaluation of different *H. italicum* preparations and systematic assessments of their antiviral activity against viruses with distinct structural features remain scarce.

Prior to the work presented in this thesis, preliminary experiments investigating the effects of *H. italicum* extracts against murine hepatitis virus (MHV, *Coronaviridae*) were conducted in our laboratory and reported in a completed master's thesis [139]. Four previously described and characterised preparations (hot-water extract, ethanolic extract, essential oil, and hydrosol) [138] were evaluated against MHV. Of these, the ethanolic extract exhibited antiviral activity, supporting the antiviral potential of *H. italicum*. Furthermore, among five compounds commonly present in *H. italicum* extracts (caffeic acid, quinic acid, myricetin, arzanol, and quercetin), quercetin demonstrated antiviral activity with a selectivity index (SI) of 54 [139].

1.4 Research Hypothesis

The purpose of this dissertation is twofold: first, to provide a reliable platform for antiviral research by evaluating and integrating different *in silico* and *in vitro* techniques to assess antiviral activity and mechanisms of action; and second, to investigate the antiviral potential of selected synthetic and natural compounds (or plant extracts). The information gained from this interdisciplinary research will help expand approaches and knowledge that will further support the discovery of new antiviral drugs.

The main goals of this doctoral thesis were:

1. Development of an optimised platform for evaluating the antiviral activity of synthetic and natural compounds, providing reproducible results.
2. Evaluation of the antiviral activity of selected compounds and plant extracts and exploration of their mechanisms of action.
3. Compare the performance and results of different *in vitro* and *in silico* techniques used for antiviral evaluation, including plaque assays, quantitative PCR (qPCR), transmission electron microscopy (TEM), and computational methods (molecular dynamics simulations and MM-PBSA analyses).
4. Determine whether the identified antiviral compounds or extracts have virus-specific activity against murine hepatitis virus (MHV) *in vitro* or exhibit broad-spectrum antiviral properties.

We have tested the following hypotheses:

1. An optimised antiviral testing platform will provide reproducible results and be suitable for the evaluation of selected synthetic and natural compounds.
2. An antiviral compound identified by *in silico* analyses as a potential SARS-CoV-2 inhibitor will show *in vitro* antiviral activity against murine hepatitis virus (MHV).

3. The integration of results from different approaches, such as *in vitro* assays and computational techniques, will allow the characterisation of the compound and provide insights into its antiviral mechanism of action.

4. The extract of *Helichrysum italicum* will show antiviral activity against enveloped virus(es).

Chapter 2

Materials and Methods

2.1 Cultivation of Cells and Propagation of Viruses

2.1.1 L929 cell line

The L929 cell line is a continuous mammalian cell line derived from normal connective (areolar) and adipose tissue in the subcutaneous layer of a 100-day-old male mouse of the C3H/An strain. Originally established in 1940 by Earle *et al.*, it is one of the earliest permanently maintained cell lines used in experimental biology [140]. Due to its long history of laboratory use and well-characterised growth behaviour, L929 has become a widely used model system in many areas of biomedical research. The cell line is particularly valued for its robustness, ease of cultivation, and reproducible growth characteristics *in vitro* [141].

Morphologically, L929 cells display a spindle-shaped, fibroblast-like appearance and grow as adherent cells forming a monolayer on the surface of culture vessels. Under standard culture conditions, they proliferate relatively rapidly and tolerate a wide range of experimental manipulations, which further contributes to their widespread use in laboratory studies [141]. L929 cells are commonly used as a standard model for evaluating the biocompatibility of biomaterials and the toxic effects of chemical compounds. It is recommended in several standardised methods for *in vitro* cytotoxicity testing [142].

The L929 cell line is also an important experimental model in virology. These cells can serve as hosts for various viruses, enabling studies of viral infection, replication mechanisms, and antiviral drug discovery. Their susceptibility to viral infection enables the propagation and investigation of different viruses under controlled laboratory conditions. For example, the compound PHA767491 has been shown to effectively inhibit HSV-1 replication in L929 cells, highlighting the usefulness of this cell line for evaluating antiviral compounds [143]. Owing to their stable growth characteristics, sensitivity to viral infection, and compatibility with multiple experimental assays, L929 cells (ATCC CCL-1) remain an important *in vitro* model in virology, pharmacology, and biomedical research, and were therefore used in our study as well.

2.1.2 RAW 264.7 cell line

The RAW 264.7 cell line is a murine macrophage-like cell line widely used as an *in vitro* model for studying macrophage biology, inflammation, and host–pathogen interactions. This cell line was originally derived from a tumour induced by the Abelson murine leukaemia virus in BALB/c mice and was established by Ralph A. Raschke and colleagues in 1978 [144]. Since then, RAW 264.7 has become one of the most frequently used macrophage cell lines in immunology and biomedical research due to its stable phenotype, ease of cultivation, and functional similarity to primary macrophages.

This cell line grows as adherent cells with a round-to-irregular morphology typical of macrophages and displays many characteristic features of the monocyte–macrophage lineage. It is commonly used to investigate the molecular mechanisms of inflammation and innate immune responses, as well as to study macrophage polarisation, antimicrobial defence mechanisms, and cytokine regulation [145]. RAW 264.7 cells (ATCC TIB-71) can be infected by several viruses (murine hepatitis virus, murine norovirus, etc.) and intracellular pathogens, allowing investigation of host–pathogen interactions and immune signalling mechanisms, making it a valuable experimental model in immunology, pharmacology, and infectious disease research [146], [147].

2.1.3 Vero E6 cell line

The Vero E6 cell line is a continuous epithelial cell line derived from African green monkey kidney cells. The parental Vero cell line was established in 1962 from normal kidney tissue [148]. The Vero E6 subline (ATCC CRL-158) was later obtained through clonal selection for improved adherence and growth properties, making it particularly suitable for virological assays and was therefore used in our study.

Vero E6 cells grow as adherent monolayers with epithelial-like morphology and are highly permissive to infection by a wide range of viruses. This permissiveness is largely due to a genetic defect in the production of type I interferons (IFN-α and IFN-β), resulting in a limited innate antiviral response [149]. Because of these characteristics, Vero E6 cells are widely used for virus isolation, propagation, and titration, as well as for studies of virus–host interactions and antiviral drug screening [150].

2.1.4 Seeding, subculturing, and maintaining cells

L929, HeLa, and Vero E6 cells were maintained as adherent cultures under standard cell culture conditions in a humidified incubator at 37 °C and 5% CO_2. Cells were grown in T25 or T75 culture flasks using complete growth media appropriate for each cell line. HeLa cells were cultured in Eagle's minimum essential medium (EMEM, ATCC, cat. no. 30-2003) supplemented with 10% foetal bovine serum (FBS, ThermoFisher, cat. no. A5256501) and 1% antibiotic solution (ATB), containing 10,000 units/mL penicillin and 10,000 µg/mL streptomycin (ThermoFisher, cat. no. 15140122). L929 cells were cultured in EMEM supplemented with 10% horse serum (HS, ThermoFisher, cat. no. 16050122) and 1% ATB, and Vero E6 cells in Dulbecco's modified Eagle medium (DMEM, ATCC, cat. no. 30-2002) supplemented with 10% FBS and 1% ATB.

For optimal cell maintenance, adherent cultures were routinely monitored and subcultured during the logarithmic phase of growth, at approximately 90% confluence, typically every 2–3 days. Excessive confluence may lead to contact inhibition, altered cellular metabolism, nutrient depletion, and eventual cell detachment. Each subculture procedure constituted one additional passage number.

Subculturing was performed under aseptic conditions in a laminar airflow (LAF) cabinet. Spent medium was removed and replaced with fresh complete growth medium. Cells were mechanically detached using a cell scraper, resuspended with a serological pipette, and transferred to a 50 mL centrifuge tube. Cell aggregates were disrupted into a single-cell suspension using a syringe and needle (0.5 × 25 mm). Preparing a uniform single-cell suspension before seeding is essential to ensure even cell distribution and reproducible growth.

Cell concentration was determined manually using a Bürker–Türk counting chamber. Cell suspension was first mixed 1:1 with 0.4% Trypan Blue solution (Thermo Scientific,

cat. no. 15250061), which selectively stains non-viable cells with compromised membrane integrity, while viable cells remain unstained. The mixture was loaded into the counting chamber, and cells were counted under an inverted microscope at 400× magnification.

The average number of cells counted across the quadrants was calculated and corrected for the 1:1 Trypan Blue dilution using a dilution factor (R) of 2. As the chamber volume was 100 nL (1.0 mm × 1.0 mm × 0.1 mm), the value was multiplied by 10,000 to obtain the final cell concentration expressed as cells/mL. The viable cell concentration (cells/mL) was therefore calculated as $n/N \times R \times 10{,}000$.

For subculturing, the cell concentration was adjusted to ~10^5 cells/mL before reseeding. Appropriate seeding density is critical for maintaining cell viability and ensuring sufficient space and nutrients for continued proliferation. Cell suspensions (5–10 mL for T25 flasks and 20–25 mL for T75 flasks) were transferred into new culture flasks and incubated under standard growth conditions. Regular microscopic observation was performed to monitor cell morphology, attachment, and proliferation.

Mycoplasma monitoring was routinely performed to ensure culture integrity and experimental reliability. Mycoplasmas are common contaminants of cell cultures and can significantly alter cellular physiology and experimental outcomes without producing visible signs of contamination. Infections can seriously affect the reliability, reproducibility, and consistency of results obtained with these cultures and can easily spread within the culture environment. As they compete with cells for nutrients in the culture medium, one of the first signs is a reduction in the rate of cell proliferation and slight changes in cellular responses. They may evade standard contamination control measures and spread undetected through cell cultures [151], [152]. Therefore, newly introduced cultures and established cell stocks were regularly tested for mycoplasma contamination using the MycoAlert Mycoplasma Detection Kit (Lonza, cat. no. LT07-318), which detects mycoplasma-specific enzymatic activity.

2.1.5 Murine hepatitis virus

Murine hepatitis virus (MHV) strain A59 (ATCC VR-764) is an enveloped, positive-sense, single-stranded RNA virus belonging to the genus *Betacoronavirus* within the family *Coronaviridae*. MHV is one of the most extensively studied experimental coronaviruses and has long served as a model for investigating coronavirus replication, pathogenesis, and host–virus interactions [153], [154]. The viral genome is approximately 31 kb in length and encodes structural and non-structural proteins responsible for viral replication, transcription, and virion assembly [154].

The MHV-A59 strain is commonly used in laboratory research due to its ability to efficiently infect murine cell lines and produce a pronounced cytopathic effect. Infection often results in the formation of multinucleated syncytia and extensive cell death, allowing convenient monitoring of viral replication and plaque formation *in vitro* [153]. In cell culture experiments, MHV-A59 is frequently propagated in the L929 cell line, where the virus replicates efficiently and produces high viral titres. Because it shares important structural and replication characteristics with other coronaviruses, exhibits comparable infection-related pathogenic processes, and can cause similar severe pathological outcomes, it has been widely used as a surrogate model to study coronavirus biology and to evaluate antiviral compounds *in vitro* [155], [156], [157].

2.1.6 Murine norovirus

Murine norovirus (MNV) is a non-enveloped, positive-sense, single-stranded RNA virus belonging to the genus *Norovirus* within the family *Caliciviridae*. It was first identified in laboratory mice in 2003 and is the first norovirus that can be efficiently propagated in cell

culture, making it an important experimental model for studying norovirus biology and antiviral responses [158]. The viral genome is approximately 7.5 kb in length and encodes a polyprotein that is cleaved into several non-structural proteins involved in viral replication, as well as structural proteins that form the viral capsid [159].

Unlike many viruses used in experimental antiviral studies, MNV lacks a lipid envelope, which contributes to its high environmental stability and resistance to physical and chemical inactivation. For this reason, it is widely used as a surrogate model for studying the persistence and transmission of non-enveloped enteric viruses, including human noroviruses [158], [160]. *In vitro*, MNV-1 replicates efficiently in macrophage and dendritic cell lines. In laboratory experiments, the virus is commonly propagated in the RAW 264.7 cell line, where infection results in productive viral replication and measurable cytopathic effects [159]. Because of its ability to replicate in cultured cells and its genetic and structural similarity to human noroviruses, MNV-1 has become a widely used model virus for studies of antiviral compounds, viral inactivation, and host–virus interactions. In our study, the MNV-1 strain CW1 (number CR-1937) was used.

2.1.7 Vesicular stomatitis virus

Vesicular stomatitis virus (VSV) is an enveloped, negative-sense, single-stranded RNA virus belonging to the genus *Vesiculovirus* within the family *Rhabdoviridae*. The virus is characterised by its distinctive bullet-shaped virion morphology and a genome of approximately 11 kb that encodes five structural proteins involved in viral transcription, replication, and virion assembly [161]. VSV can infect a broad range of mammalian and insect cells, contributing to its extensive use as a model system in virology.

Because of its relatively simple genome organisation and rapid replication cycle, VSV has long been used to study fundamental processes of RNA virus replication, gene expression, and virus–host interactions [162]. Infection typically leads to rapid viral amplification and pronounced cytopathic effects in susceptible cell lines, making the virus particularly suitable for plaque assays and antiviral screening experiments. *In vitro*, VSV is commonly propagated in the Vero E6 cell line, where it replicates efficiently and produces high viral titres [163]. Due to these characteristics, VSV has become an important experimental model for investigating viral entry mechanisms, host immune responses, and the antiviral activity of compounds [164]. In our study, the VSV strain Indiana Lab [V-520-001-522] (number VR-1238) was used.

2.1.8 Virus propagation

For virus propagation, cells were cultured in T25 flasks until approximately 80% confluence. The spent medium was removed, and cells were infected with 50 µL of virus stock suspension (viral titre of 10^6 plaque-forming units (PFU)/mL) diluted in 4 mL of complete growth medium. Cultures were incubated at 37 °C until cytopathic effects (CPE) developed, typically after 72 h. To facilitate the release of intracellular virus particles, cultures underwent two consecutive freeze–thaw cycles, with overnight freezing at −80 °C and −20 °C, and intermediate thawing at room temperature. Cells were then detached using a sterile scraper, resuspended, and centrifuged at 100 × g for 5 min to pellet cellular debris. The virus-containing supernatant was collected, filtered through a 0.22 µm filter, aliquoted into sterile microcentrifuge tubes, and stored at −80 °C until further use.

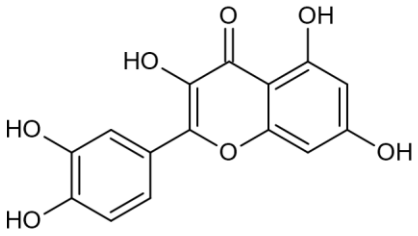
2.2 Plant Material

Plant material used in this study was *Helichrysum italicum* ssp. italicum from the commercial herbal estate in the Primorska region of Slovenia (coordinates: 45°27'05''N, 13°41'31''E). The area has a Mediterranean climate (Csa/Csb in the Köppen classification) with some continental influence from nearby inland regions, and Mediterranean-type soils influenced by karstic geology and proximity to the Adriatic coast. The soils are slightly alkaline to neutral due to high calcium content from limestone and are well-suited for cultivating Mediterranean herbs. Aerial parts of the plants were harvested at the stage of development of generative shoots, before their full flowering period, in June 2024, and air-dried. Dried plant material was then stored at room temperature in a dark, dry place until further use.

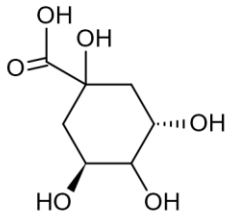
2.3 Extracts and Compounds

Plant-derived extract and chemical compounds used in this study were prepared or obtained as follows:
(a) Plant extract and phenolic compounds.
An ethanolic extract was prepared using a 50:50 (v/v) ethanol–water mixture. Briefly, 2.5 g of the dried, ground plant material was extracted with 50 mL of solvent at room temperature in the dark for 5 days. The extract was filtered through Whatman No. 41 filter paper and concentrated using a rotary evaporator (Rotavapor® R-300; BÜCHI Labortechnik AG) [165]. The dried residue was reconstituted in 5 mL of the original solvent mixture (ethanol–water, 50:50) and stored at −20 °C until use.

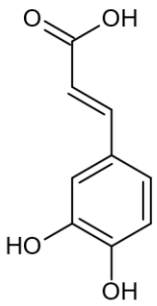
Phenolic compounds used for testing – quercetin (cat. no. Q4951), caffeic acid (cat. no. C0625), quinic acid (cat. no. PHR1468), and chlorogenic acid (cat. no. C3878) – were obtained from Sigma-Aldrich (Figure 5). All compounds were dissolved in DMSO and stored at −20 °C until use.



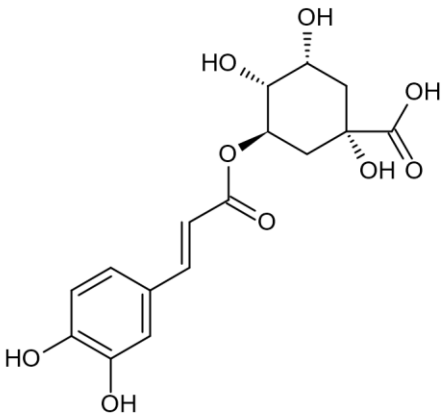
Quercetin



Quinic acid



Caffeic acid



Chlorogenic acid

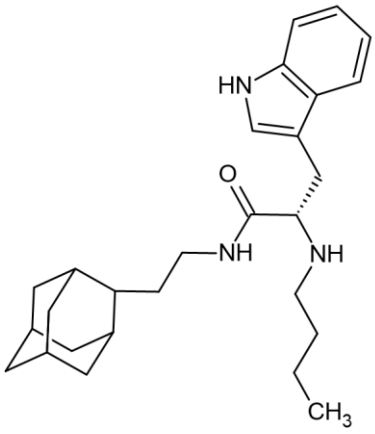
Figure 5: Structures of the tested phenolic compounds.

(b) Synthetic and reference antiviral compounds.

The lead candidate (LC), (*S*)-*N*-(2-((1*S*,3*S*,5*S*,7*S*)-adamantan-2-yl)ethyl)-2-(butylamino)-3-(1*H*-indol-3-yl)propenamide, was synthesised as previously described [166]. 5-(*N*,*N*-hexamethylene)amiloride (HMA, cat. no. A9561) and rimantadine hydrochloride (RMT, cat. no. PHR3267) were obtained from Sigma-Aldrich. In addition, six candidate compounds identified through virtual screening were obtained from MolPort. LC, HMA, and MolPort compounds were dissolved in DMSO, while RMT was dissolved in water. All compounds were stored at −20 °C until use. Full names and chemical structures of the compounds are shown in Table 1, Table 2, Figure 6, and Supplementary Table 1.

Table 2: Tested synthetic and reference compounds.

Compound abbreviation or Molport ID	**Full name**
LC	(*S*)-*N*-(2-((1*S*,3*S*,5*S*,7*S*)-adamantan-2-yl)ethyl)-2-(butylamino)-3-(1*H*-indol-3-yl)propenamide
HMA	5-(*N*,*N*-hexamethylene)amiloride
RMT	rimantadine; 1-(1-adamantyl)ethanamine
MolPort-027-939-308	2-(adamantan-1-yl)-*N*-(1*H*-indazol-3-yl)acetamide
MolPort-038-394-572	(1S,3S)-3-(2-amino-6-{[3-(pyridin-3-yl)propyl]amino}pyrimidin-4-yl)cyclobutan-1-ol
MolPort-038-419-202	1-methyl-2,4-dioxo-*N*-[1-(pyrimidin-2-yl)piperidin-3-yl]-1,2,3,4-tetrahydropyrimidine-5-carboxamide
MolPort-046-573-024	(1R,2S)-1-phenyl-2-{[3-(pyrrolidine-1-carbonyl)pyridin-2-yl]amino}propan-1-ol
Molport-027-882-992	5-[(3R,4R)-3-(hydroxymethyl)-4-[(4-methyl-1,4-diazepan-1-yl)methyl]pyrrolidine-1-carbonyl]pyrazin-2-ol
MolPort-027-939-308	sodium (5-{2-[(5-chloro-2-methoxyphenyl)formamido]ethyl}-2-methoxybenzenesulfonyl)(methylcarbamothioyl)azanide



Lead candidate

Figure 6: Chemical structure of the lead candidate (LC).

2.4 Cytotoxicity Assay

The Cell Counting Kit-8 (CCK-8, Abcam, cat. no. ab228554) assay was performed according to the manufacturer's protocol. L929 and Vero cells (3×10^5 cells/mL) or RAW 264.7 cells (7×10^5 cells/mL) were seeded in 96-well plates and incubated for 24 h at 37 °C before treatment with different concentrations of compounds or extracts. Negative controls (complete growth medium), solvent controls (depending on the tested material),

and assay-specific positive controls were included in all experiments. After 48 h at 37 °C, 10 µL of CCK-8 reagent was added to each well, and the plates were incubated in the dark at 37 °C for 1.5 h. Absorbance was measured at 460 nm using a Cytation 5 microplate reader (Agilent BioTek). Relative cell viability was calculated using the following formula: Cell viability (%) = (OD of sample / mean OD of negative control) × 100. N = 3 biological replicates were performed for each compound and extract, with n = 5 technical wells per condition.

2.5 Virological Methods

2.5.1 Determination of virus concentration using the endpoint dilution assay

After propagation and harvesting (Section 2.1.8), the virus concentration or titre was determined as 50% tissue culture infective dose ($TCID_{50}$). This indicates the concentration of virus in suspension at which 50% of the cells in a monolayer, grown in a 96-well microtiter plate, are infected and display cytopathic effects.

The day before, L929 and Vero cells (3×10^5 cells/mL) or RAW 264.7 cells (7×10^5 cells/mL) were seeded in a 96-well microtiter plate and incubated overnight until reaching 90% confluency. The following day, serial 10-fold dilutions of the virus suspension in culture medium were prepared in a new 96-well microtiter plate, with each column containing a separate dilution, and the last two columns containing culture medium alone as negative controls. The spent medium was removed from the confluent cells, and the prepared virus dilutions were immediately added to prevent cell desiccation. The plates were then incubated and monitored for the appearance and progression of cytopathic effects over 48–72 h.

After cytopathic effects appeared, the medium was removed, the cells were fixed with 4% formaldehyde for 20 minutes, and stained with 1% crystal violet for 15 minutes. The presence or absence of cytopathic effects was then assessed using an inverted microscope at 400x magnification. Using the distribution of infected and uninfected wells across the dilutions, the $TCID_{50}$ was calculated according to the Reed–Muench method [167].

2.5.2 Time-of-addition experiment

L929 and Vero cells (3×10^5 cells/mL) or RAW 264.7 cells (7×10^5 cells/mL) were seeded in 12-well culture plates and incubated at 37 °C for 24 h. Each compound, or combination of compounds (at the highest non-cytotoxic concentrations), was added in two technical replicates to the MHV (0.001 MOI), MNV (0.02 MOI), or VSV (0.0005 MOI) and/or cells at different time points in relation to virus inoculation as previously described (Figure 7) [74], [168]. For the virus inoculation, medium (EMEM or DMEM) without serum was always used.

(a) Pre-treatment: cells were pre-treated with each compound for 2 h to assess induction of an antiviral state. Following removal of the treatment medium and PBS washing, cells were inoculated with the virus for 1 h. Unbound virus was then removed by washing with PBS, and cells were incubated for 48 h.

(b) Co-treatment: virus was pre-incubated with each compound or extract for 1 h, after which the virus–compound/extract mixtures were inoculated onto cells to assess potential virucidal activity or interference with early stages of infection. Following 1 h of adsorption, the inoculum was removed, cells were washed with PBS to eliminate residual virus and

compounds/extracts, and fresh medium was added for a 48-h incubation. Direct virucidal activity was further evaluated for the ethanolic extract and quercetin by incubating MHV with the respective treatments for 1 h, then diluting 100-fold before infection. This dilution reduced the compound/extract concentration below active levels, allowing exclusion of reversible binding effects.
(c) Post-treatment: cells were inoculated with virus in the absence of compound to assess post-entry antiviral activity. After 1 h of viral adsorption, the inoculum was removed, and cells were washed with PBS to eliminate unbound virus. Cells were then incubated for 48 h in the presence of the compound.

Controls included mock-treated cells (non-infected, non-treated), vehicle-treated infected cells (depending on the tested material), and HMA as a positive control. Cell culture supernatants collected after 48 h were used to determine plaque numbers by plaque assay. For each treatment and compound/extract combination, three independent biological replicates (N = 3) were performed.

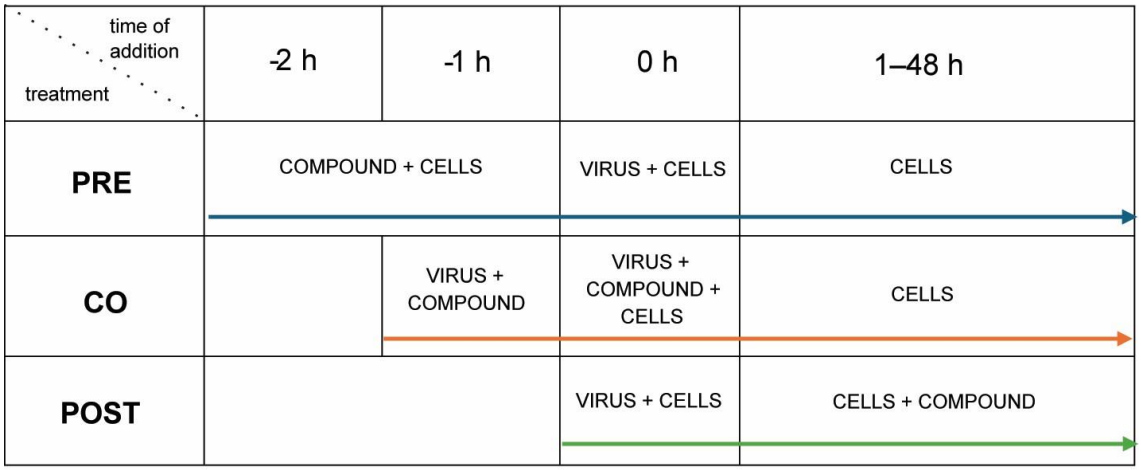


Figure 7: Time-of-addition experiments scheme.

2.5.3 Plaque reduction assay

L929, Vero cells (3×10^5 cells/mL), or RAW 264.7 cells (7×10^5 cells/mL) were seeded in 12-well culture plates and incubated at 37 °C for 24 h. Cells were then infected with supernatant from virus-infected samples (10^{-2} and 10^{-3} dilutions in medium) in two technical replicates (n = 2) for 1 h at 37 °C and 5% CO_2. Following infection, cells were washed with PBS and overlaid with 0.8% methyl cellulose overlay medium (prepared as a 1:1 mixture of 2 × EMEM and 1.6% methyl cellulose, with a viscosity of 4000 cP; Sigma-Aldrich). After 24–48 h, the overlay was removed, and cells were washed with PBS, fixed with 3.7% paraformaldehyde for 15 min, and stained with 1% crystal violet for 20 min. Plates were washed with distilled water, plaques were counted, and values were normalised to the vehicle control (infected cells treated with medium). Per cent inhibition was calculated using the formula: (mean plaques $_{\text{vehicle}}$ − mean plaques $_{\text{compound}}$) / mean plaques $_{\text{vehicle}}$ × 100%.

2.6 Tentative Identification of Phenolic Compounds by Mass Spectrometry

Ethanolic extract was characterised by high-performance liquid chromatography (HPLC) and mass spectrometry to identify the most abundant phenolic compounds. The identification of phenols was performed using tandem mass spectrometry (MS/MS; LTQ XL; Thermo Scientific) in negative ion mode, with parameters as previously reported [170]. Data were acquired using Xcalibur 2.2 software (Thermo Scientific). Compound identification was based on a combination of fragmentation pattern analysis and comparison with external standards.

2.7 Light Microscopy and Transmission Electron Microscopy

The effects of MHV infection and lead candidate (LC) treatment on L929 cells were observed using light microscopy and transmission electron microscopy. Four samples were prepared in parallel. The first sample (L929) served as the uninfected control and was cultured for 72 h. The second sample (L929+MHV) was cultured under identical conditions for 24 h, then infected with MHV at an MOI of 0.001 for 1 h, and incubated for an additional 48 h. The third and fourth samples were treated with LC under post-treatment conditions: L929+LC (LC-treated, uninfected cells) and L929+MHV+LC (LC-treated cells infected with MHV at an MOI of 0.001 for 1 h). All samples were prepared in duplicate. At 48 h post-infection (hpi), cultures were harvested by scraping and immediately fixed in 3% glutaraldehyde in 0.1 M phosphate-buffered saline (PBS), post-fixed in 1% osmium tetroxide for 1 h, dehydrated with ethanol, and finally embedded in Agar 100 resin. Semithin and ultrathin sections were prepared using an Ultracut UC7 (Leica) with glass and diamond knives, respectively. Semithin sections were stained with toluidine blue and examined with a light microscope (Zeiss AxioSkop Opton) equipped with a digital camera (Leica DFC290HD; Leica Application Suite 4.0.0). Ultrathin sections were stained with 1% (w/v) aqueous solution of uranyl acetate and lead citrate. The grids were then examined with a transmission electron microscope, the TALOS L120C (Thermo Scientific), operating at 100 kV and equipped with a Ceta 16M camera.

2.8 qPCR and Digital PCR

2.8.1 Experimental set-up

L929 cells were used to assess the effect of treatments on MHV replication under two experimental conditions:
(a) Co-incubation assay (for ethanolic extract).
L929 cells (3×10^5 cells/mL) were seeded in 12-well plates and incubated at 37 °C with 5% CO_2 for 24 h. The following day, MHV at a multiplicity of infection (MOI) of 0.001 was incubated with different concentrations of the ethanolic extract for 1 h (co-incubation). The mixtures were then added to the cells. After 1 h of viral adsorption, the cells were washed with PBS to remove unbound virus and extract, and complete EMEM was added; the cells were then cultured at 37 °C. Positive controls were infected, untreated cells (virus incubated with medium only), while negative controls were neither infected nor treated. Supernatants were collected at 1, 12, 24, and 48 h post-infection. Experiments were

performed in two biological replicates (N = 2), with two technical replicates per condition (n = 2).
(b) Post-treatment assay (for LC, HMA, and RMT).
L929 cells were seeded in 12-well plates and, after 24 h, inoculated with MHV (MOI 0.001) for 1 h at 37 °C and 5% CO_2. The inoculum was then replaced with complete EMEM containing either the highest non-toxic concentration of the inhibitor (LC, HMA, or RMT) or the corresponding vehicle (0.5% DMSO) for infected untreated controls. Negative control samples were neither infected nor treated. Cells were detached by trypsinisation (3 min) and combined with the corresponding supernatant. Samples (cells and supernatants) were collected at 0, 24, and 48 h post-treatment. Experiments were performed in two biological replicates (N = 2) for HMA and RMT, and three biological replicates (N = 3) for LC, with three technical replicates per condition (n = 3).

2.8.2 RNA extraction and qPCR analysis

The presence and amount of MHV RNA were monitored at different time points, depending on the treatment. RNA was extracted from all collected samples, and MHV and mouse GAPDH RNA levels were quantified by qPCR. Each RNA sample was analysed in triplicate, with each sample originating from two or three technical replicates on the plate (as described in Section 2.8.1). Consequently, the average copy number was calculated from the mean Cq values obtained from a total of six (n = 6) or nine (n = 9) technical replicates, respectively.

RNA was extracted from 140 µL of harvested material using the QIAamp Viral RNA Mini Kit (QIAGEN, cat. no. 52906) according to the manufacturer's instructions. A negative extraction control (nuclease-free water) was included to monitor potential cross-contamination. RNA was eluted in 80 µL and stored at −80 °C until analysis.

RNA samples were analysed either undiluted or after 10-fold dilution in RNase-free water (Thermo Fisher Scientific, cat. no. 4388514). Each sample was tested in two or three technical replicates.

Quantification of MHV RNA and mouse GAPDH RNA was performed by one-step RT-qPCR using the AgPath-ID One-Step RT-PCR Kit (Applied Biosystems, cat. no. 4387391). The 10 µL reaction mixture contained MHV-specific primers (900 nM; MHV-A59-FP: GGA ACT TCT CGT TGG GCA TTA TACT; MHV-A59-RP: ACC ACA AGA TTA TCA TTT TCA CAA CAT A) and probe (200 nM; MHV-A59-Probe: FAM/ACA TGC TAC GGC TCG TGT AAC CGA ACT GT/BHQ) [171] or a mouse GAPDH assay (Thermo Fisher Scientific, cat. no. 4352339E), and 2 µL of RNA template. Negative controls of amplification (NTC; nuclease-free water) and positive controls (RNA extracted from MHV stock) were included in each run.

Thermal cycling was performed on a 7900HT Fast Real-Time PCR System (Applied Biosystems) under the following conditions: 48 °C for 10 min, 95 °C for 10 min, followed by 45 cycles of 95 °C for 15 s and 60 °C for 60 s. All qPCR experiments followed MIQE 2.0 guidelines.

2.8.3 Data analysis

qPCR data were analysed using SDS software (version 2.4.1, Applied Biosystems). Amplification curves and controls were first evaluated to confirm assay validity. Cq values were exported to MS Excel, where mean Cq values of technical replicates were calculated and used to determine viral RNA copy numbers.

Quantification was performed using a standard curve generated from 10-fold serial dilutions (10^{-1} to 10^{-7}) of RNA extracted from MHV stock ($10^{5.5}$ $TCID_{50}$/mL). In the co-

incubation experiments, samples with a single positive replicate and Cq > 37.0 (based on the dilution curve) were considered negative.

For statistical comparisons, average viral RNA copy numbers were calculated from all biological and technical replicates for each condition.

2.8.4 Droplet digital PCR (ddPCR)

The number of viral RNA copies in the MHV stock solution was determined by droplet digital PCR (ddPCR) using the MHV-specific assay [171] and previously described conditions [172]. The 20 µL reaction mixture consisted of 2 × One-Step RT-ddPCR Advanced Kit for Probes (Bio-Rad, cat. no. 1864021), primers (900 nM), probe (250 nM), and 4 µL of RNA template. Four consecutive 10-fold dilutions of viral RNA were analysed, and the average copy number was calculated. Acceptance criteria included more than 10,000 positive droplets and no signal in the NTC.

2.9 Statistical Analyses

For plaque reduction assay data, sigmoidal dose–response curves (variable slope) were used to calculate the half-maximal effective concentration (EC_{50}) and cytotoxic concentration (CC_{50}). The selectivity index (SI) was determined as the ratio of CC_{50} to EC_{50}. All data were plotted and analysed using GraphPad Prism software (version 10.4.0, GraphPad Software), and results are presented as mean ± standard deviation (SD).

For qPCR data, statistical significance was evaluated between treatment groups and their corresponding controls using two-way analysis of variance (ANOVA) followed by a multiple comparison test, as specified below:
(a) Plant extract and phenolic compounds.
Treatment groups (infected samples treated with extract or phenolic compounds) were compared to control samples consisting of infected cells treated with the corresponding vehicle (0.5% DMSO or medium; vehicle control). Dunnett's multiple comparison test was applied. Significance levels were defined as p-values ≤ 0.03 (*), ≤ 0.002 (**), ≤ 0.0002 (***), and ≤ 0.0001 (****).
(b) Synthetic and reference antiviral compounds.
Treatment groups (infected samples treated with compounds) were compared to control samples consisting of infected cells treated with the corresponding vehicle (0.5% DMSO; vehicle control). Šidák's multiple comparison test was applied. Significance levels were defined as p-values < 0.05 (*), < 0.01 (**), < 0.001 (***), and ≤ 0.0001 (****).

2.10 Computational Techniques

2.10.1 Candidate sourcing and databases

Candidate compounds were screened using two approaches:

(a) ZINC15 database.
The ZINC15 database [173], comprising 997,402,117 molecules, was downloaded and used for large-scale virtual screening.
(b) FKKT Compound Library (FKKTLib).
The FKKT Compound Library (FKKTLib; Faculty of Chemistry and Chemical Technology, University of Ljubljana) currently contains 3,428 unique, literature-

documented synthetic compounds [174]. The library was searched for adamantane substructures to identify candidates containing this scaffold.

2.10.2 Molecular docking

The NMR structure of the SARS-CoV-2 Epro reported by Mandala *et al.* (PDB ID: 7K3G; resolution 2.1 Å) was selected as the target structure [26]. Protein preparation was performed using the Schrödinger Protein Preparation Wizard [175], [176], including restrained energy minimisation and optimisation of the hydrogen-bonding network. A receptor grid was then generated for docking.

(a) ZINC15 database.
Initially, a high-throughput virtual screening (HTVS) was performed, using a large set of compounds from the ZINC15 database. Docking was performed at the N-terminal binding site of the SARS-CoV-2 Epro ion channel. Post-docking, six molecular descriptors were generated for each molecule. To discriminate for molecules with higher druglikeness and oral bioavailability, a strict (so-called Lipinski) filter–tolerating one violation per molecule– was applied [177], [178]. Specifically, compounds were excluded if they exceeded two or more of the following thresholds: molecular weight > 500 g/mol, logP > 5, more than 5 hydrogen bond donors, more than 10 hydrogen bond acceptors, more than 10 rotatable bonds, or a topological polar surface area (TPSA) above 140 Å^2. This step was followed by the detection and exclusion of motifs resembling pan-assay interference compounds (PAINS) [179] and moieties that could be toxic or reactive (REOS) [180]. In the subsequent re-docking campaign, the filtered compounds were docked into the prepared receptor using Schrödinger Glide [176], [181], [182]. A hierarchical docking workflow was applied, consisting of HTVS, followed by standard precision (SP) and extra precision (XP) docking steps, using default settings. The top-ranking compounds from this workflow were selected for further analysis.
(b) FKKTLib.
After substructural screening and lead candidate (LC) extraction, docking was performed for the LC and positive control (RMT) at the C- and N-terminal binding sites of the SARS-CoV-2 Epro ion channel, yielding three complexes: RMT-C-Epro, RMT-N-Epro, and LC-N-Epro. The docking step was carried out using Schrödinger software with an extra-precision step via Glide, applying standard settings [183].

2.10.3 Chemical space investigation and filtering

(a) ZINC15 database.
To gain further insight into the chemical space of the filtered dataset, MACCS keys [172] were generated using RDKit software, and low-variance features were removed from the dataset. In contrast to path-based fingerprints, MACCS keys are structural keys that encode the presence of specific functional groups for an organic molecule in a binary vector. Optimised for bioactive substances, MACCS keys provide a global overview of the biologically relevant functional group space and allow discrimination between molecules based on their predominant functional groups. Two dimensionality-reduction techniques – PCA and PaCMAP – were used to group the molecules based on the generated structural keys. The retained principal components were submitted to the PaCMAP algorithm using default parameters. After clustering, eight lead candidates were selected based on docking score and structural diversity. The protein-ligand interactions were visualised using PyMOL [173] and BioRender, and the volume of the SARS-CoV-2 Epro channel was calculated using Caver 3.0 software [184].

2.10.4 Molecular dynamics simulations

(a) ZINC15 database and (b) FKKTLib.
The three ligand-protein complexes from the FKKTLib (RMT-C-Epro, RMT-N-Epro, and LC-N-Epro) and nine ligand-protein complexes from the ZINC15 database (L1–L8 and RMT) were used as inputs for classical MD simulations. Each complex was embedded in a 1-palmitoyl-2-oleoylphosphatidylcholine (POPC) lipid bilayer (the total number of lipid molecules in both layers was ∼778) located in a rectangular simulation box (edge lengths of the box 165 × 165 × 97 Å). The assembled ligand-protein-lipid systems were solvated with ∼46,490 TIP3P water molecules. ∼126 Na^+ and ∼127 Cl^- ions were added to neutralise the system and mimic a physiological 0.150 mol/L NaCl solution. The complexes were embedded in the membrane, and the system was solvated using the CHARMM-GUI web server [185], [186], [187], [188], [189], [190], [191], [192]. Each system consisted of a total of ∼325,000 atoms. GROMACS software [193] was used to perform the molecular dynamics simulations of the equilibrated SARS-CoV-2 Epro ligand complexes at 37 °C and 1 bar. Amber FF19SB was used to describe the protein [194], and the membrane was described with the Lipid21 force field [195]. GAFF2 was used to describe ligands, which were parametrised using the Amber21 module ANTECHAMBER [196], [197]. The protein-ligand binding free energy and the per-residue contributions were calculated via single-trajectory Molecular Mechanics Poisson-Boltzmann Surface Area (MM-PBSA) calculations using gmxMMPBSA [198].

Chapter 3

Results

3.1 *In silico* Characterisation of the Candidates

We identified novel inhibitors of the SARS-CoV-2 envelope protein (Epro) using two complementary *in silico* strategies: the large-scale ZINC15 database and the focused FKKTLib compound library. The ZINC15 database enabled us to screen virtually across an extensive chemical space of nearly one billion molecules, while FKKTLib allowed us to target structurally relevant adamantane-based compounds. After molecular docking (and filtering, clustering, and ligand prioritisation of the ZINC15 candidates), we further characterised the selected candidates using molecular dynamics simulations and MM-PBSA binding free energy analysis. In this results section, we present the identification of the most promising compounds, their binding modes within the Epro ion channel, and their predicted stability and affinity compared with the known inhibitor rimantadine.

3.1.1 Search for candidates from the ZINC15 database

3.1.1.1 High-throughput virtual screening (HTVS)

HTVS of nearly 1 billion compounds from the ZINC15 database yielded a smaller subset of 9,911 ligand molecules (0.001‰ of the top-scoring molecules). Of these, 3,916 (43.0%) passed the subsequent filtering step, during which a total of 44 Lipinski, 51 PAINS, and 5,959 REOS violations were recorded (previously described in Section 2.10.2).

3.1.1.2 Chemical space visualisation

To further explore the remaining chemical space of the filtered ZINC15 database, MACCS keys were generated from the filtered dataset, and clustering was performed. This process resulted in six distinct clusters (Figure 8A), each characterised by recurring functional-group motifs. Cluster A consists of molecules containing halide groups, while Cluster B consists mainly of tetrahydrofuran-containing compounds. Cluster C represents molecules with sulfone groups. Cluster D includes compounds featuring functional groups such as amides and five-membered heteroaromatic rings, including isoxazoles, oxazoles, and thiazoles. Cluster E consists of nitrogen-containing functional groups, such as cyclic amines, triazoles, and tetrazoles, and Cluster F primarily contains molecules bearing diamides and triamides, often in combination with groups such as spiro compounds, ethers, alcohols, and amines. An interactive visualisation of chemical space is available at https://sars-cov-2-envelope-protein.gitlab.io/eprotein-data/.

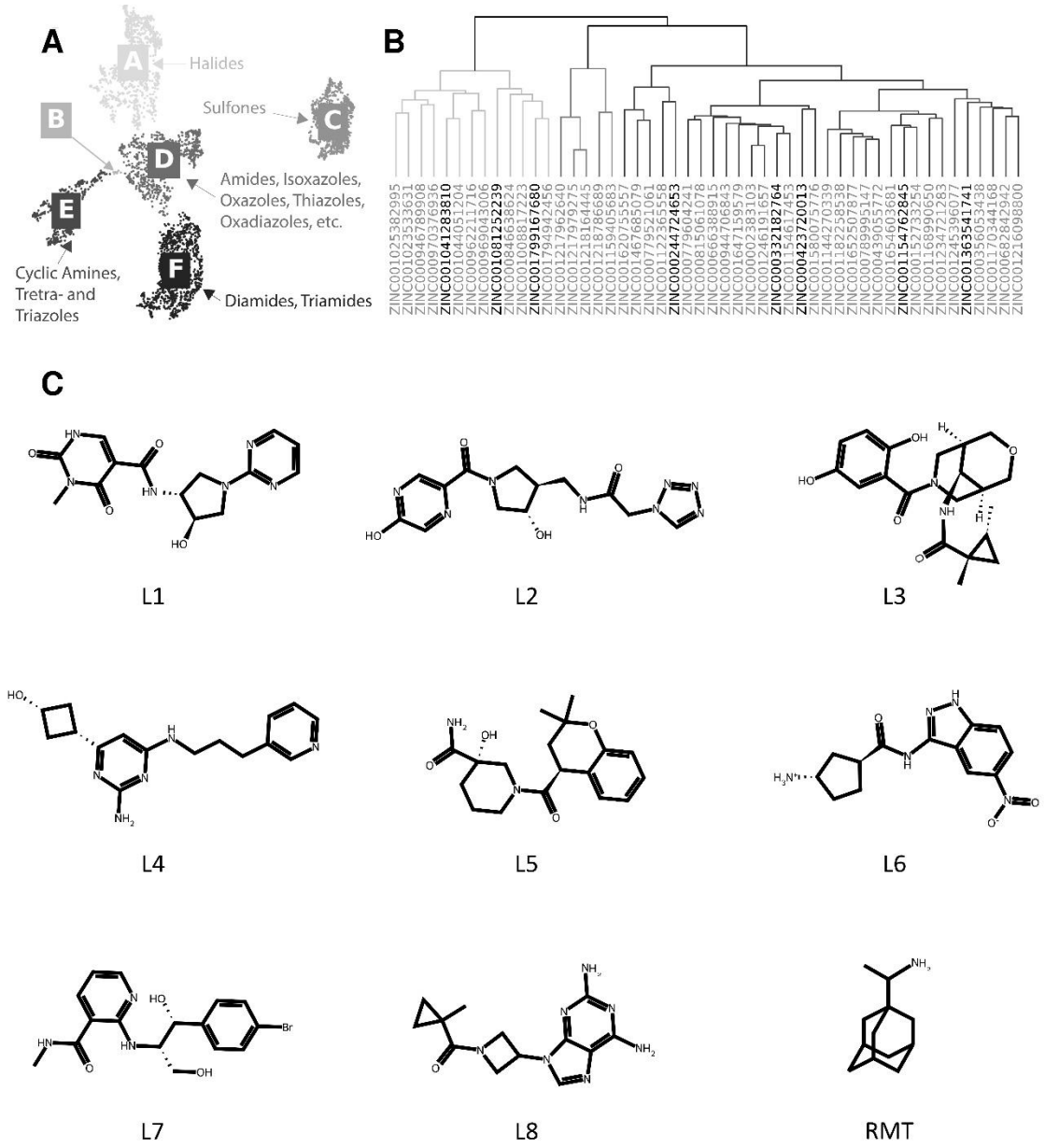


Figure 8: Chemical space analysis and lead compounds selection. **(A)** Chemical space of the filtered dataset after dimensionality reduction and clustering, displaying five clusters (A–F). Each cluster represents recurring functional-group motifs. An interactive plot can be found under: https://sars-cov-2-envelope-protein.gitlab.io/e-protein-data/. **(B)** Hierarchical clustering of the top 50 scoring compounds of the re-docking step. Prioritised compounds are highlighted in black. **(C)** Selection of lead compounds (L1–L8) and rimantadine (RMT). The selected compounds L1–L8 correspond to the highlighted compounds in the dendrogram (panel **B**) in descending order from left to right [27].

3.1.1.3 Re-docking and ligand prioritisation

The remaining 3,916 compounds from the HTVS and filtering steps were re-docked, and the top 50 compounds were identified for further evaluation. Hierarchical clustering was performed for these compounds, resulting in three main branches (Figure 8B). The leftmost

branch contains molecules with bridged bicyclic motifs, *rac*(3*R*,4*S*)-4-aminopyrrolidin-3-ol moieties, and indane derivatives such as indoles. The middle branch contains ellagic acid, salicylfluorone, and 5-chloropyrimidine-4,6-diamine motifs. The rightmost branch contains chromane derivatives as well as many heterocycle-substituted indene moieties. Eight structurally diverse ligand candidates (L1–L8) with high docking scores were selected from these clusters for a further MD study. Their structures are shown in Figure 8C.

3.1.1.4 MD simulations and MM-PBSA analysis

The eight selected candidates were subjected to 200 ns of MD simulations, and the system with RMT was simulated for 125 ns. The root-mean-square deviations (RMSDs) calculated for the C-α atoms of SARS-CoV-2 Epro reach a stable state after ∼100 ns, except for L7, for which the MD simulation was extended to 300 ns (Supplementary Figure 1). In the case of RMT, the RMSD was already stable after 50 ns, and the simulation time was therefore shortened to 125 ns. The average plateau RMSD values ranged from 0.48 to 0.58 nm (Supplementary Figure 1), reflecting moderate structural flexibility characteristic of proteins with flexible loops and solvent-exposed regions. However, we note that this flexibility does not impair channel integrity or compromise ligand stability. In addition, slight movements of the pentameric domains and ligand-induced conformational changes also contribute to the overall RMSD. Nevertheless, the protein's secondary-structure elements were well conserved throughout the MD simulations. The radius of gyration remained consistently stable over the simulated time, indicating a stable assembly of the SARS-CoV-2 Epro ion channel (Supplementary Figure 2). Three candidates formed stable complexes within the N-terminal vestibule of SARS-CoV-2 Epro. These include L2, L3, and L5, while others dissociated from the active site during the simulation. The dissociation of certain candidates is mainly attributed to shallow channel binding, weak hydrogen bonds, and limited van der Waals interactions with the amino acid residues (Supplementary Figures 3 and 4). The channel is mainly a hydrophobic stretch, and only a few amino acid residues are responsible for the ligand-protein interaction (Figure 2B–E, Supplementary Table 2). In addition, the channel offers limited space, leading to steric clashes between residues and certain tested ligands. The number of hydrogen bonds varied considerably for each candidate during the simulation (Supplementary Figure 3), indicating an overall dynamic binding regime.

An MM-PBSA analysis was performed to evaluate the binding affinity of each ligand. The total binding free energies are listed in Table 3. Ligand L3 exhibits the strongest binding, followed by ligands L2 and L5. The ΔG_{bind} in case of RMT was ∼1.7-fold (L5) to ∼2.5-fold (L3) lower than that of our lead compounds. At the amino acid residue level, GLU8, THR11, LEU12, and ASN15 were found to be major contributors to binding for the top three candidates (see Supplementary Figure 4 for the per-residue contributions). Throughout the simulation, L3 showed significant binding with three ASN15 and one THR11 side chain from adjacent SARS-CoV-2 Epro monomers (Supplementary Table 2). L3's strong binding interactions with ASN15 and THR11 residues are supported by analysis of the most populous cluster (Figure 9B), showing a total of five hydrogen bonds among three adjacent ASN15 residues. These interactions involve the ether group of L3. In addition, the 2-formylhydroquinone moiety of L3 participates via one of its hydroxyl groups and its carbonyl group, with the first acting as a single donor and the latter as a triple acceptor for the three adjacent ASN15 residues. Furthermore, the second hydroxyl group of the 2-formylhydroquinone moiety acts as a hydrogen-bond donor to a THR11 residue. The 2-formylhydroquinone moiety of L3 penetrates deepest into the channel. At the same time, the bridged cycle above exhibits a space-demanding, rigid geometry, in which L3 adopts an almost plug-like conformation within the channel.

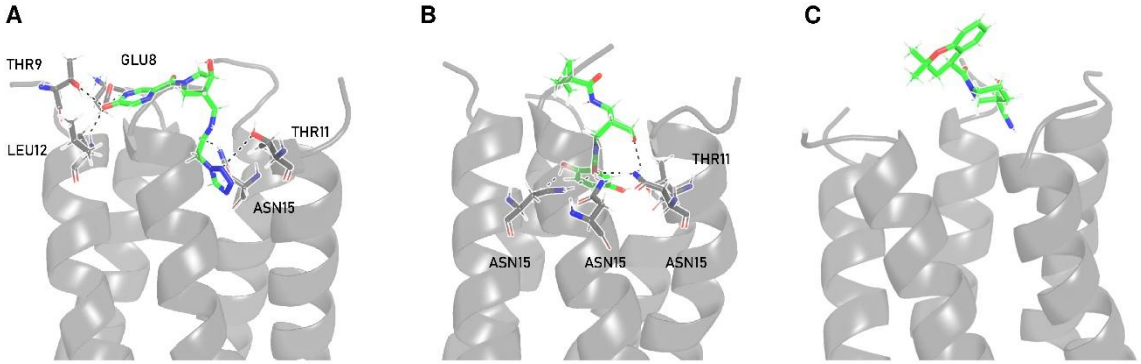


Figure 9: Binding poses and hydrogen-bond interactions of selected lead compounds. (**A**–**C**) corresponds to L2, L3 and L5, respectively. Protein moieties are depicted in grey. The ligand is depicted in green. Nitrogen and oxygen atoms are depicted in blue and red, respectively. Hydrogen bonds are shown as dashed black lines [27].

L2, the second-highest-scoring candidate, exhibits significant binding to the adjacent residues LEU12 and GLU8 (Supplementary Table 2). Overall, ASN15 and THR11 still contribute to binding (Supplementary Figure 4), but their effect is less pronounced than that of L3. The highest populated cluster (Figure 9A) reveals hydrogen bond interactions between one aromatic nitrogen of the pyrazine moiety and a GLU8 residue, along with an additional hydrogen bond and polar interactions involving the same GLU8 and a THR9 and LEU12 from an adjacent monomer, mediated by the hydroxyl group of the pyrazine moiety. On the opposite side, a THR11 residue exhibits a polar interaction with one nitrogen atom of the tetrazole moiety of L2. Additionally, ASN15 from an adjacent monomer acts as a hydrogen bond donor to the carbonyl oxygen of the neighbouring amide group. In total, six hydrogen bonds and polar interactions involving five residues are observed. L2 spans the entire channel lumen, with its tetrazole group extending deepest into the channel.

For L5, the candidate with the lowest binding free energy score showed no significant interactions with any residue above the threshold of 1.8 kcal/mol (Supplementary Table 2). Clustering analysis of the highest populated cluster (Figure 9C) confirms this observation. Overall, L5 occupies about one-third of the pore, possibly providing enough space for ions to pass through the channel. Its relatively simple structure and lack of significant binding may indicate that L5 is not a highly specific ligand.

For RMT, a known inhibitor of SARS-CoV-2 Epro, no significant interactions with any residue above the threshold of 1.8 kcal/mol were observed (Supplementary Table 2). Clustering analysis of the highest populated cluster (Supplementary Figure 6) confirms this observation, with no hydrogen bonds present. Overall, RMT exhibits a space-demanding, rigid geometry, similar to L3, and effectively occupies space in the channel. RMT's interactions appear to be dominated by its apolar adamantane core, while contacts via its amino group remain transient. We note that although RMT exhibits a weaker ΔG_{bind} than L5, it appears to occlude the pore more efficiently.

Table 3: MM-PBSA total binding free energies (ΔG_{bind}) of SARS-CoV-2 Epro–ligand complexes. For candidates that have dissociated from the protein during the MD simulation time, ΔG_{bind} is not reported [27].

Candidate	ΔG_{bind} [kcal/mol]
L1	dissociated
L2	-30.1 ± 3.6
L3	-32.3 ± 2.0
L4	dissociated
L5	-21.7 ± 6.1
L6	dissociated
L7	dissociated
L8	dissociated
RMT N-terminal	-13.2 ± 2.6

3.1.2 Search for candidates from the FKKTLib

3.1.2.1 MD simulations and MM-PBSA analysis

The adamantane substructure query returned a focused set of FKKTLib entries containing the targeted scaffold. From these, we prioritised a lead candidate (LC), based on (i) unambiguous substructure match quality, (ii) availability of solid sample material for confirmation studies, and (iii) presence of coherent supporting annotations, yielding a well-characterised adamantane derivative as the most promising hit for subsequent evaluation.

Herein, docking at the C- and N-terminal binding side of the SARS-CoV-2 Epro ion channel for LC and RMT yielded three complexes: RMT-C-Epro, RMT-N-Epro, and LC-N-Epro. We note that docking of LC to the C-terminal of Epro did not yield any results to incorporate, due to the ligand's unfavourable steric properties. Specifically, LC appeared unable to access the binding pocket because of its excessive size, limited flexibility, and steric clashes with the receptor. Consequently, LC was found to bind exclusively in the N-terminal vestibule (LC-N-Epro) and was subjected to three independent 350 ns-long MD replicas. RMT in the C-terminal vestibule (RMT-C-Epro) was simulated in three independent 200 ns-long replicas.

The RMSD of the C-α atoms of Epro reaches a stable value after ~75 ns. In the case of RMT-N-Epro, the RMSD was already stable after 50 ns. The average plateau RMSD values ranged from 3.9 to 5.3 Å (Supplementary Figure 7), reflecting moderate structural flexibility characteristic of proteins with flexible loops and solvent-exposed regions. Importantly, this flexibility did not compromise channel integrity or ligand stability. Minor motions of the pentameric domains and ligand-induced conformational changes contributed to the overall RMSD, yet the protein's secondary-structure elements remained well conserved throughout the simulations. The radius of gyration remained stable throughout the simulation, indicating a stable assembly of the Epro ion channel (Supplementary Figure 8). The number of hydrogen bonds varied considerably among candidates during the simulation (Supplementary Figure 9), indicating an overall higher number of hydrogen bonds for the LC throughout the simulation.

An MM-PBSA analysis was performed to rank the ligands' binding affinities. The total binding free energies are listed in Table 4. LC consistently exhibits the strongest binding, followed by the RMT-C-Epro complexes. The ΔG_{bind} in the case of RMT was ~1.7-fold (C-terminal) lower than that of our lead candidate. At the amino acid residue level, GLU8

and THR11 were found to be major contributors to binding for LC (see Supplementary Figure 10 for the per-residue contributions), while the three runs showed differing extents of residue involvement.

Table 4: Total binding free energies (ΔG_{bind}) and duration of the MD simulation.

MD Run	ΔG_{bind} (kcal/mol)	Duration (ns)
LC N-terminal replica 1	-35 ± 4	350
LC N-terminal replica 2	-35 ± 7	350
LC N-terminal replica 3	-44 ± 4	350
RMT C-terminal replica 1	-22 ± 1	200
RMT C-terminal replica 2	-25 ± 2	200
RMT C-terminal replica 3	-21 ± 2	200

In two of the three simulations, LC displayed significant binding to a GLU8 side chain (Supplementary Table 3); notably, this interaction was ~6.7- and 2.2-fold stronger in the first run than in the second and third runs, respectively. Furthermore, the third replica reports significant binding to two ASN15 residues and a LEU18 residue. Analysis of the highest populated clusters supports these findings (Figure 10A–C), with the first and third replicas (rep-1 and rep-3) displaying hydrogen bonds between an ASN15 amine group and the carbonyl and secondary amine of LC's amide group, respectively. The second replica (rep-2) displays a hydrogen bond between a GLU8 carboxy group and the amine of LC's amide group. Despite the small differences between the three replicas, the MM-PBSA binding free energies for LC remain overall similar, indicating a small ensemble of distinct but comparably stable binding modes in which either C=O $\cdots$ H_2N@ASN15, NH $\cdots$ O=C@ASN15, or NH $\cdots$ O=C@GLU8 contacts serve as the primary anchor. Herein, the per-residue contributions for rep-1 and rep-3 point to a more mixed binding mode, with residues such as GLU8, THR9, THR11, and LEU18 contributing to binding. In contrast, rep-2 is strongly dominated by GLU8 (Supplementary Figure 10), whose persistent interaction across all runs further suggests a retainer-like role for GLU8 in suppressing axial drift and preventing dissociation from the N-terminal vestibule. We further note that in all replicas, LC's indole group and aliphatic chain face outwards from the channel, restricting hydrogen bonding to LC's amide and secondary amine. The adamantane moiety of LC penetrates the deepest into the channel and exhibits a space-demanding, rigid geometry, in which LC adopts an almost plug-like conformation within the channel. For RMT, no significant interactions with any residue above the threshold of 1.8 kcal/mol were observed at the C-terminal vestibule (Supplementary Table 3). MM-PBSA analysis suggests relevant interactions with LEU28, ALA32, and THR35 residues. The structures of the highest populated clusters (Figure 10D–F) do not show any hydrogen bonding for RMT at the C-terminal vestibule. Overall, RMT exhibits a space-demanding, rigid geometry, similar to LC, and effectively occupies space in the channel. In both cases, interactions appear to be dominated by their hydrophobic adamantane cores, with burial values indicating moderate channel penetration depths of (8 ± 2) Å and (6 ± 3) Å across runs for LC and RMT, respectively. While for RMT contacts via its amine group remain transient, LC seems to stabilise its binding via its amide group. In all simulations, the C-terminal ARG38 residues of the Epro homopentamer are consistently oriented towards the lipid–water interface and form salt bridges between their positively charged guanidinium groups and the negatively charged phosphate headgroups of the POPC bilayer. These

interactions persisted throughout the simulated timeframe and were observed across all monomers. Notably, in the C-terminal vestibule, the positively charged ligand RMT remained stably bound near ARG38 throughout the simulations. It did not dissociate from its binding site, despite the expected electrostatic repulsion between the positively charged groups.

In the initial ZINC15 screening study, RMT was evaluated in the N-terminal vestibule, where all prioritised ligands were predicted to bind. During the 125 ns MD simulation, RMT remained associated with the N-terminal site and did not dissociate, thereby enabling MM-PBSA calculations and comparisons with the ZINC15 candidates. Under these conditions, L2, L3, and L5 showed more favourable calculated binding free energies than RMT. However, in the subsequent FKKTLib study, extended simulations revealed that RMT dissociated from the N-terminal vestibule in the latter stage of the simulation, suggesting that this site may not represent its most stable binding mode. This prompted additional docking and simulation of RMT in the C-terminal vestibule, where stable binding was observed across three independent 200 ns replicas, as described above. Consequently, in the second study, RMT was treated as a C-terminal binder, and only the C-terminal MM-PBSA values were used for comparison with the lead candidate (LC). Nevertheless, the top ZINC15 candidates L2 and L3 still exhibited more favourable calculated binding free energies than C-terminal RMT by ~1.3-fold (L5) to 1.4-fold (L3), while L5 showed a comparable but slightly weaker binding free energy. Direct comparison between LC and the earlier N-terminal RMT values from the ZINC15 study should be interpreted with caution, as the later results indicate that the C-terminal vestibule is likely the more relevant reference binding site for RMT.

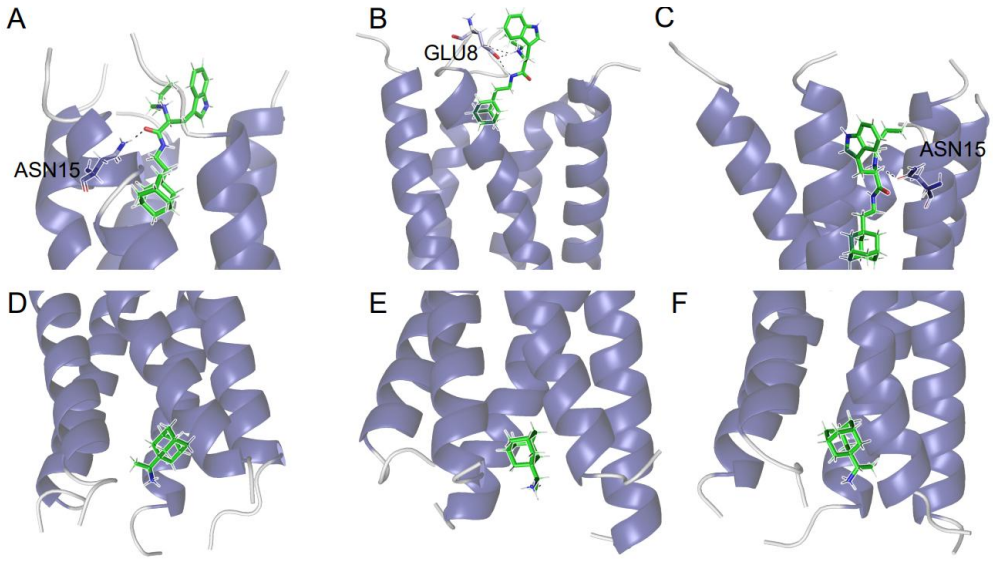


Figure 10: Most representative clusters depicting hydrogen-bond interactions and binding poses. The final compound selection of LC-N-Epro (replicas 1–3 corresponding to **A**–**C**) and RMT-C-Epro (replicas 1–3 corresponding to **D**–**F**), respectively. Protein moieties are depicted in blue (α-helix) and white (disordered). The ligand is depicted in green. Nitrogen and oxygen atoms are depicted in blue and red, respectively. Hydrogen bonds are shown as dashed black lines [169].

3.2 *In vitro* Characterisation of the Antiviral Activity of Candidate Compounds

Following *in silico* identification of selected compounds, we characterised their antiviral activity *in vitro* using different techniques. Structurally related, commercially available ZINC15-derived analogues of the prioritised *in silico* hits were first evaluated to assess whether the predicted antiviral activity against SARS-CoV-2 could be transferred to the MHV biological system. The study then focuses on the lead candidate (LC), from the FKKTLib library, for which cytotoxicity, antiviral efficacy against MHV, effects on viral replication, and associated cellular and ultrastructural changes were systematically investigated. Finally, the antiviral activity of *Helichrysum italicum* ethanolic extract and its major constituents was characterized *in vitro* against different viruses to explore mechanisms of action and identify natural compounds contributing to the observed antiviral effect.

3.2.1 Characterisation of candidates from the ZINC15 database

Based on *in silico* analyses, a set of structurally related, commercially available compounds highly similar to the prioritised candidates was selected for experimental validation. Six such compounds were obtained and tested for antiviral activity against the model coronavirus MHV.

Before antiviral evaluation, the cytotoxicity of all compounds was assessed to determine their half-maximal cytotoxic concentration (CC_{50}) values (Supplementary Table 1). The highest non-cytotoxic concentrations were then used in plaque reduction assays performed under different treatment conditions, including time-of-addition experiments. None of the tested compounds reduced plaque formation under the conditions applied; therefore, no further testing was conducted.

These results suggest that, despite their structural similarity to the computationally prioritised candidates, the commercially available analogues either do not interact effectively with the viral target or exhibit activity highly specific to subtle structural features not preserved in the tested compounds. Alternatively, they may not be active against MHV under the experimental conditions employed.

3.2.2 Characterisation of the lead candidate from the FKKTLib

3.2.2.1 Cytotoxicity and antiviral activity against MHV

In cytotoxicity assays, the lead candidate (LC) exhibited cytotoxicity at concentrations above 30 µM, with a CC_{50} of 43 µM. The positive control HMA showed a comparable CC_{50} of 41 µM, while RMT was less cytotoxic, with a more than twofold higher CC_{50} of 96 µM (Table 5). Cytotoxic effects were evident at concentrations above 20 µM for HMA and 40 µM for RMT; however, the increase in cytotoxicity was more gradual for RMT compared to LC and HMA (Figure 11A–F).

LC and the positive controls reduced MHV infectivity when added after viral infection of cells (post-treatment) (Figure 11A–C), with LC showing a half-maximal effective concentration (EC_{50}) of 12.7 µM and a selectivity index (SI) of 3.4. HMA and RMT showed EC_{50} values of 7.6 µM and 26 µM, yielding SIs of 5.4 and 3.7, respectively (Table 5). When administered simultaneously with the virus (co-treatment), only LC and HMA showed antiviral activity (Figure 11D–F). LC showed an EC_{50} of 12 µM and an SI of 3.6, which is

very close to its efficacy under post-treatment conditions. HMA showed lower antiviral activity during co-treatment (EC_{50} = 14 µM and a corresponding SI of 3.0) and was about half as effective as in post-treatment conditions. In contrast, RMT showed no activity at the concentrations tested under co-treatment conditions. Importantly, none of the compounds reduced MHV infectivity when administered before virus infection under pre-treatment conditions. High repeatability (low variability) was observed in all three biological repetitions (Table 5).

Table 5: Dose-response results of the tested compounds in L929 cells infected with MHV. Mean of half-maximal effective (EC_{50}) and cytotoxic (CC_{50}) values with standard deviations (SD) are presented, calculated from three biological replicates (N = 3); the selectivity index (SI) was calculated as CC_{50}/EC_{50}. Cells were treated with the lead candidate (LC), or reference compounds 5-(*N*,*N*-hexamethylene)amiloride (HMA) and rimantadine (RMT) under post-treatment (post), co-treatment (co), and pre-treatment (pre) conditions [169].

COMPOUND (treatment)	CC_{50} (µM) (mean ± SD)	EC_{50} (µM) (mean ± SD)	SI
LC (post)	43 ± 1	12.7 ± 0.8	3.4
LC (co)		12 ± 1	3.6
LC (pre)		non-effective	/
HMA (post)	41 ± 2	7.6 ± 0.4	5.4
HMA (co)		14 ± 1	3.0
HMA (pre)		non-effective	/
RMT (post)	96 ± 5	26 ± 2	3.7
RMT (co)		non-effective	/
RMT (pre)		non-effective	/

To evaluate the specificity of the LC's proposed mechanism, we performed a counter-screen using murine norovirus (MNV), a non-enveloped virus that does not encode a classical viroporin. Plaque assays and time-of-addition assays were performed with MNV (MOI 0.02) and RAW 264.7 cells, using the same three experimental conditions as for MHV (pre-, co-, and post-incubation). Importantly, LC exhibited no detectable antiviral activity in this system, supporting the conclusion that its antiviral effect is not nonspecific but rather dependent on the presence of a (coronavirus) viroporin.

3.2.2.2 The effect of the lead candidate on the viral replication of MHV

To follow viral replication, we performed quantitative PCR (qPCR) analysis following post-treatment with LC, HMA, and RMT. Total RNA was extracted from combined cell lysates and supernatants collected at 0, 24, and 48 h post-treatment.

Quantification of MHV RNA was enabled by a standard curve generated from a dilution series of a known viral RNA sample (6.5×10^5 copies/µL in the undiluted sample, corresponding to $10^{5.5}$ $TCID_{50}$/mL). The resulting standard curve showed a wide dynamic

range over six orders of magnitude (slope = –3.35; intercept = 37.2; $R^2 = 0.999$), enabling accurate quantification of viral RNA in experimental samples. Expression of the GAPDH gene was monitored in all samples to assess cellular RNA integrity, relative content, extraction efficiency, and possible amplification inhibition. Mean GAPDH Cq values were consistent across experiments (mean Cq = 23.8, SD = 1.9), confirming the comparability of RNA input and quality.

As expected, the viral RNA levels in the infected cells increased over time. At 1 h post-infection (time point 0 h post-treatment), MHV RNA levels were near the limit of detection (~1 copy/µL) for all treatments. By 24 h post-treatment, viral RNA levels increased by more than four orders of magnitude, reaching 5×10^4–4×10^6 copies/µL in the positive controls (untreated infected samples). Importantly, treatment with LC resulted in a significant ~100-fold (2 $\log_{10}$) decrease in viral RNA levels at 24 h post-treatment compared to the positive control. A significant difference compared to the positive control was also observed for HMA and RMT at this time point. However, at 48 h post-treatment, RNA levels in the treated samples did not differ significantly from those of the positive control and peaked at 2×10^7 copies/µL (Figure 11G–I).

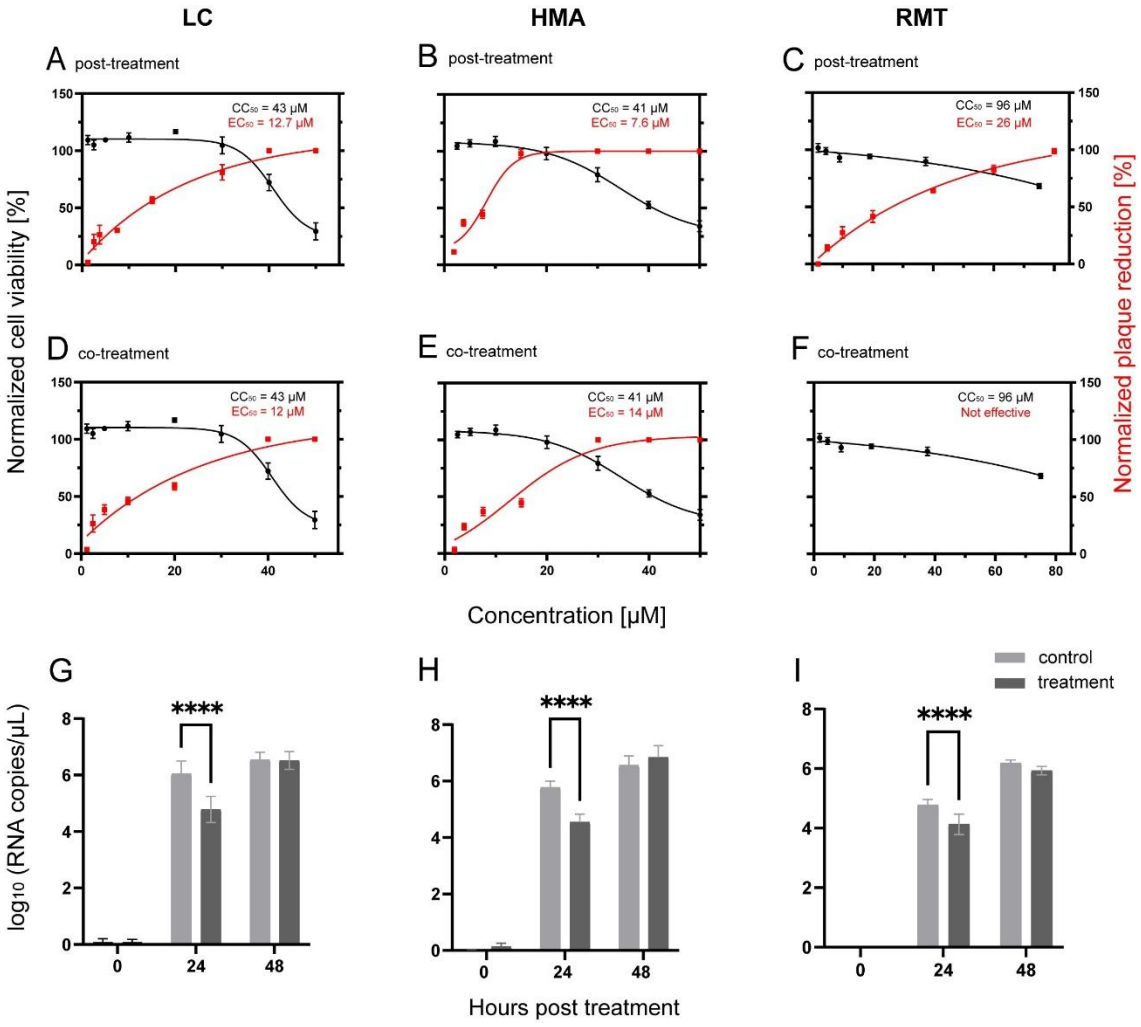


Figure 11: Antiviral activity and effect on viral replication of LC, HMA, and RMT. **(A–F)** Results of plaque reduction assay and time-of-addition (ToA) assay for the lead candidate (LC; A, D) and the reference compounds 5-(*N*,*N*-hexamethylene)amiloride

(HMA; B, E), and rimantadine (RMT; C, F), shown under post-treatment (upper panels) and co-treatment (lower panels) conditions. **(G–I)** Viral replication for the tested compounds (LC: G, HMA: H, RMT: I) at 0, 24, and 48 h post treatment in $\log_{10}$(RNA copies/µL). $^{****}P \leq 0.0001$ (two-way ANOVA, followed by Šidák's test) [169].

3.2.2.3 Effects of the lead candidate on cell morphology and ultrastructure in MHV-infected cells

We analysed the effects of LC on MHV infectivity using light microscopy and transmission electron microscopy (TEM) 48 h post-infection (72 h after seeding), comparing four conditions: untreated cells (L929), infected cells (L929+MHV), LC-treated uninfected cells (L929+LC), and LC-treated infected cells (L929+MHV+LC).

3.2.2.3.1 Light microscopy

Light microscopy of semi-thin sections provided a general overview of the cell morphology (Figure 12). Because cells were harvested by scraping, the typical spindle-shaped morphology was lost; instead, cells appeared round to oval in all observed samples. In the L929 sample, cell boundaries were clearly defined, and cell death was minimal (Figure 12A). In contrast, in the L929+MHV sample, most cells were dead, appearing as light-coloured patches, although the overall cell shape was largely preserved (Figure 12B). Cell viability was markedly improved in infected cells treated with LC (L929+MHV+LC) (Figure 12D). Treatment with LC, either alone or in the presence of infection, resulted in cell morphology largely similar to that of the uninfected control (L929). We note that LC-treated samples frequently showed cell–cell fusions, producing large multinucleated cells, which may result from cytopathic effects at the concentration tested. Notably, this dose did not appear cytotoxic in the standard CCK-8 viability assay, which reflects cellular metabolic activity (Figure 12C, D).

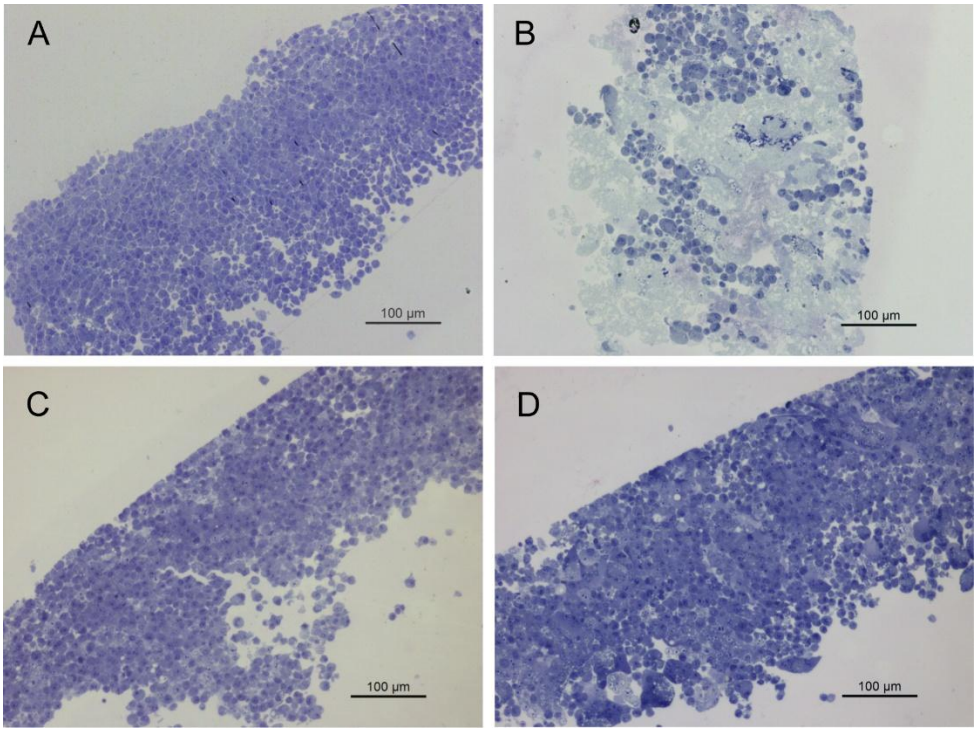


Figure 12: Light microscopy of semi-thin sections. **(A)** Untreated and uninfected cells (L929). **(B)** Infected cells (L929+MHV); dead cells are lighter and semi-transparent; viable

cells are darker. **(C)** Uninfected cells treated with the LC (L929+LC) and **(D)** infected cells treated with the LC (L929+MHV+LC) [169].

3.2.2.3.2 Transmission electron microscopy

Ultrastructural analysis by TEM provided further insights into viral replication and cellular response. Untreated and uninfected cells (sample L929) had an electron-dense cytoplasm, numerous microvilli protruding from the entire surface, well-preserved mitochondria, endoplasmic reticulum (ER), and Golgi complexes. Membrane vesicles with myelin-like structures were observed only occasionally (Figure 13A). Infected cells (sample L929+MHV) showed extensive viral replication with widespread cytopathic effects. Numerous round to slightly oval virus particles with a diameter of about 65–80 nm were visible by TEM and were distributed both intracellularly and in the extracellular space (Figure 13B–D). The spike proteins were not always clearly recognisable on the virion surface. Dead cells and cell debris, often interspersed with virus particles, predominated over viable cells. Despite the cytopathic damage, the cytoplasm of the infected cells remained electron-dense, with mitochondria preserved in large numbers. The cell nuclei were often more amoeboid in shape compared to those of uninfected cells. Infected cells often contained abundant vesicles with viral particles, many of which appeared to originate from the ER. The size and morphology of these vesicles varied considerably across sections, ranging from small, spherical structures to large, round or tubular vesicles. In most cells, the ER appeared dilated. In addition, perinuclear regions resembling viral replication complexes or "viral factories" were frequently observed [199], [200]. These structures, typically ~1 µm in diameter, had no bounding membrane and consisted of dense networks of short, disorganised tubes within a highly electron-dense matrix (Figure 13C).

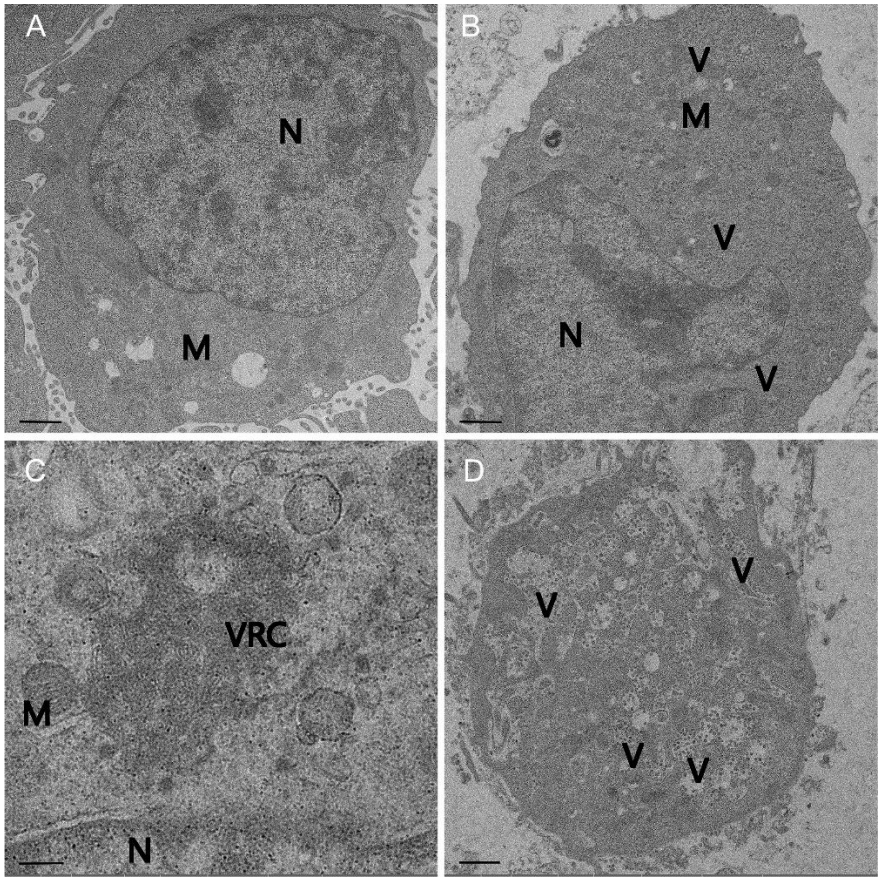


Figure 13: Ultrastructural analysis of MHV infection in L929 cells by transmission electron microscopy (TEM). **(A)** Uninfected, untreated cells (L929), scale bar 1 µm. **(B)** Untreated infected cells (L929+MHV), scale bar 1 µm. **(C)** Untreated infected cells (L929+MHV), scale bar 200 nm. **(D)** Untreated infected cells (L929+MHV), scale bar 1 µm. N: nucleus; V: viral particles; M: mitochondria; VRC: viral replication complex [169].

ER-derived myelin-like membrane whorls were observed within intracellular vesicles in all samples. These structures, typically associated with nascent virions and indicative of virus-induced membrane remodelling [73], [201], [202], [203], were present at low frequency in untreated cells (L929) but occurred more frequently following treatment with LC (L929+LC) (Figure 14A). Their abundance increased under both viral infection and inhibitor exposure alone, suggesting that different forms of cellular stress can independently promote their formation, as previously reported [73], [200].

In contrast, double-membrane vesicles (DMVs), which serve as sites for early stages of viral replication [200], [204], [205], [206], were not detected at 48 hpi. This may be because DMVs are not always present as discrete structures, but rather form part of an interconnected reticulovesicular network derived from the ER, which later fuses to form larger cytoplasmic vacuoles containing assembled virions [204], [207].

Treatment with LC (L929+LC) led to the appearance of myelin-like membrane whorls within the intracellular vesicles, which occurred more frequently than in untreated cells (sample L929) (Figure 14A). In LC-treated infected cells (L929+MHV+LC), viral replication was still evident as shown by the presence of replication complexes and vesicle-associated virus particles (Figure 14B–D). The virus-induced changes in the cells were similar to those observed in untreated infected cells (L929+MHV). In contrast to L929+MHV, virus particles in LC-treated infected cells were primarily intracellular, whereas extracellular virions were rarely detected (Figure 13D and Figure 14B–C).

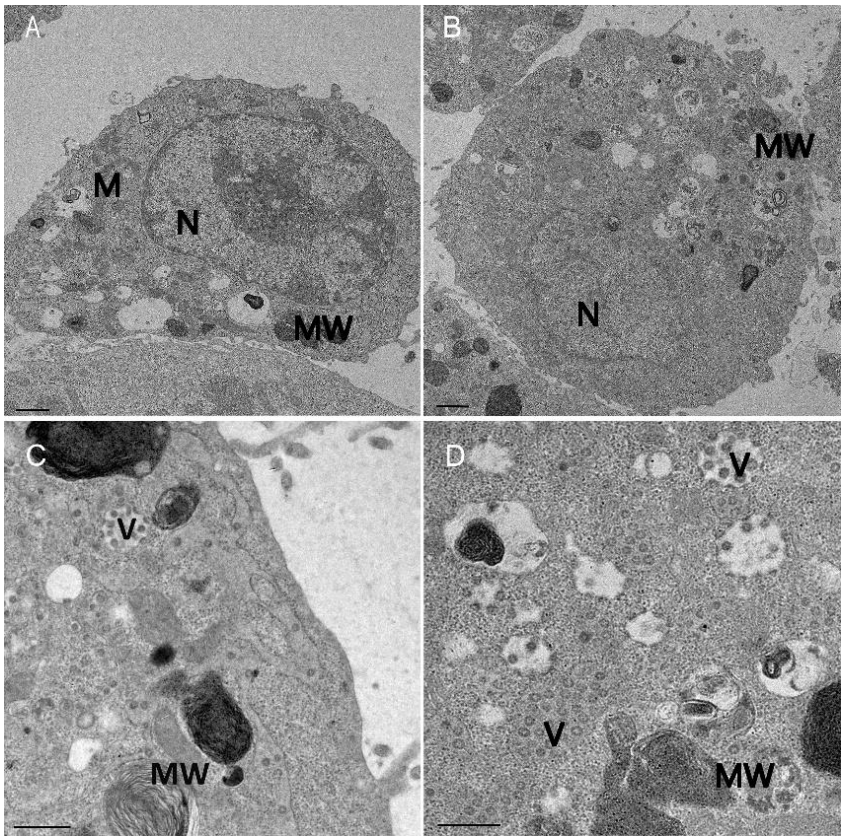


Figure 14: Ultrastructural comparison of LC-treated infected and uninfected L929 cells by transmission electron microscopy (TEM). **(A)** Uninfected cells treated with the lead candidate (LC) (L929+LC), scale bar 1 µm. **(B)** LC-treated infected cells (L929+MHV+LC), scale bar 1 µm. **(C, D)** LC-treated infected cells (L929+MHV+LC), scale bar 500 nm. N: nucleus; V: viral particles; M: mitochondria; MW: myelin-like whorls [169].

Virus particles were counted in intracellular and extracellular compartments from representative TEM sections of L929 cells infected with MHV in the absence or presence of LC (Table 6 and Figure 15). Counts were obtained from seven independent TEM images of different cells for each condition. Due to the two-dimensional nature of ultrathin sections, the orientation of the cutting plane, and variability in the cellular area captured, these values represent a semi-quantitative estimate rather than absolute numbers of virus particles per cell. Areas exhibiting disintegration, particularly in infected samples in the absence of LC (L929+MHV), were excluded from the analysis. Disintegrated cells were rarely observed in LC-treated samples, consistent with light microscopy observations (Figure 12). The data support a reduction in extracellular virions in LC-treated samples, with very few virus particles detected outside cells. We, however, note that these values represent a semi-quantitative estimate rather than the absolute number of virus particles per cell.

Table 6: Viral particle counts in infected untreated and LC-treated L929 cells (TEM). Number of intracellular and extracellular virus particles in untreated infected cells (L929+MHV) and LC-treated infected cells (L929+MHV+LC) across seven independent TEM images per condition [169].

Treatment condition	Intracellular virus particles	Extracellular virus particles
L929+MHV	253	83
L929+MHV+LC	180	3

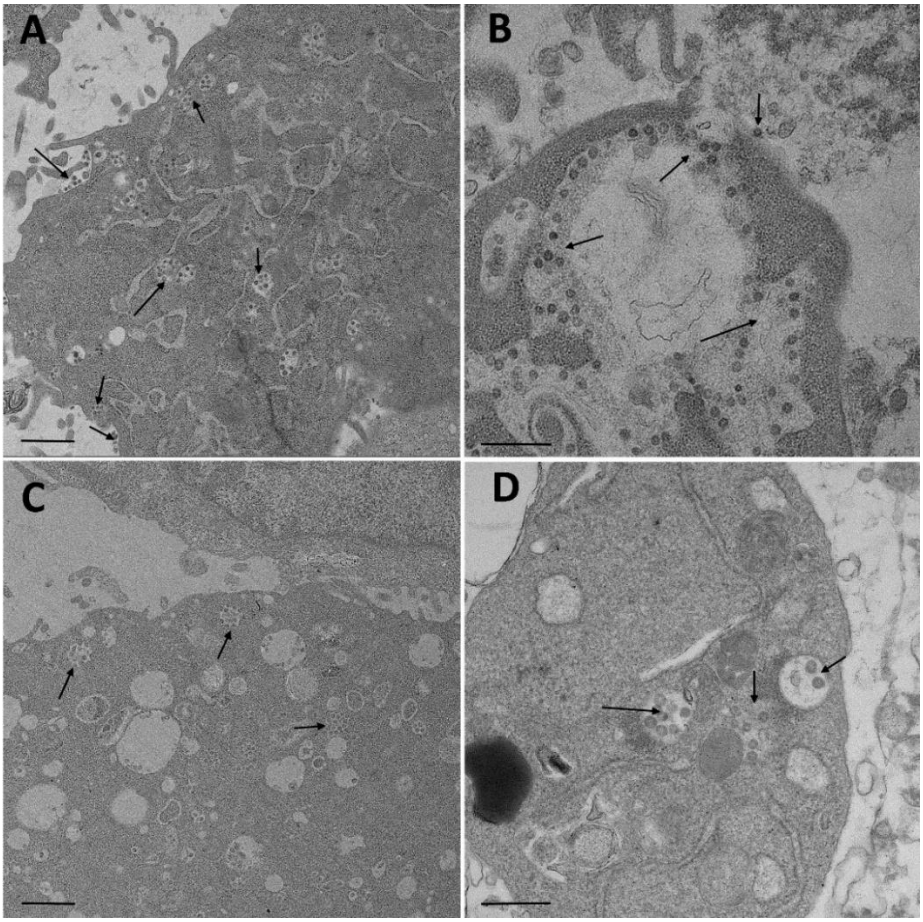


Figure 15: Virus particles in MHV-infected L929 cells visualised by transmission electron microscopy (TEM), with or without LC. **(A)** Untreated infected cells (L929-MHV), scale bar 1 µm. **(B)** Untreated infected cells (L929+MHV), scale bar 500 nm. **(C)** LC-treated infected cells (L929+MHV+LC), scale bar 1 µm. **(D)** LC-treated infected cells (L929+MHV+LC), scale bar 500 nm. Arrows indicate virus particles [169].

3.2.3 Characterisation of *Helichrysum italicum* extract and active constituents

3.2.3.1 Cytotoxicity and antiviral activity of *Helichrysum italicum* ethanolic extract against MHV, VSV, and MNV

H. italicum ethanolic extract was tested against MHV under three different conditions (pre-, co-, and post-treatment). It exhibited potent antiviral activity and low cytotoxicity (EC_{50} = 0.22 µg/ml; CC_{50} > 500 µg/ml; SI > 2300) (Table 7, Figure 16A), outperforming the positive control, 5-(*N*,*N*-hexamethylene)amiloride (HMA) (SI = 3). Time-of-addition (ToA) experiments demonstrated the ethanolic extract's effect under co-treatment conditions, indicating either direct interaction with virus particles in a virucidal manner or interaction with the virus at entry stages of the viral life cycle [168]. Subsequent experiments designed to distinguish between these possibilities demonstrated that viral

infectivity was not reduced by ethanolic extract when virus–extract mixtures were diluted before infection. This finding indicates that the ethanolic extract interferes with early virus–cell interactions and excludes virucidal activity.

Ethanolic extract also exhibited antiviral activity under co-treatment conditions against the enveloped VSV with an SI approximately 2-fold lower compared to SI for MHV (EC_{50} = 0.42 µg/ml; CC_{50} > 500 µg/ml; SI > 1180), pointing to its more potent activity against MHV (Table 7, Figure 16B). No antiviral activity was observed against non-enveloped MNV. High repeatability (low variability) was observed over all three biological replicates of the experiments (Table 7).

Table 7: Extract and compounds tested against enveloped and non-enveloped viruses. Murine hepatitis virus (MHV), vesicular stomatitis virus (VSV), and murine norovirus (MNV) were used as model viruses. Half-maximal effective concentrations (EC_{50}) with standard deviations (SD) are presented; the selectivity index (SI) is calculated as CC_{50}/EC_{50}. N = 3 biological replicates. n.t.: not tested.

	Viruses		
	MHV	VSV	MNV
Extract			
ethanolic extract	EC_{50} = 0.22 ± 0.08 µg/ml SI > 2300	EC_{50} = 0.42 ± 0.1 µg/ml SI > 1180	non-effective
Compounds			
chlorogenic acid	non-effective	n.t.	n.t.
quinic + caffeic acid	non-effective	n.t.	n.t.

3.2.3.2 Cytotoxicity and antiviral activity of compounds from *Helichrysum italicum* ethanolic extract against MHV

Based on the tentative MS/MS identification of compounds in the ethanolic extract (Section 3.2.3.4), the antiviral activity of individual compounds was evaluated. Important compounds commonly identified in *H. italicum* extracts, such as quercetin, myricetin, arzanol, quinic acid, and caffeic acid, have already been evaluated against MHV under three different conditions (pre-, co-, and post-treatment) in our laboratory and reported in a master's thesis [139]. Among the tested phenolics, only quercetin exhibited antiviral activity against MHV (EC_{50} = 0.95 µM; SI = 54). As observed for the ethanolic extract, tested in this doctoral thesis, the antiviral effect of quercetin was restricted to co-treatment conditions [139].

For this doctoral thesis, additional experiments were conducted to investigate the mechanism of action of quercetin and to evaluate the antiviral activity of chlorogenic acid and a combination of quinic and caffeic acids.

Additional experiments, analogous to those conducted with the ethanolic extract, showed that diluting virus–quercetin mixtures before infection did not reduce viral infectivity, thereby excluding a virucidal mechanism. These findings indicate that quercetin, like the ethanolic extract, interferes with early virus–cell interactions. In contrast, chlorogenic acid showed no antiviral activity, nor did a combination of quinic and caffeic acid.

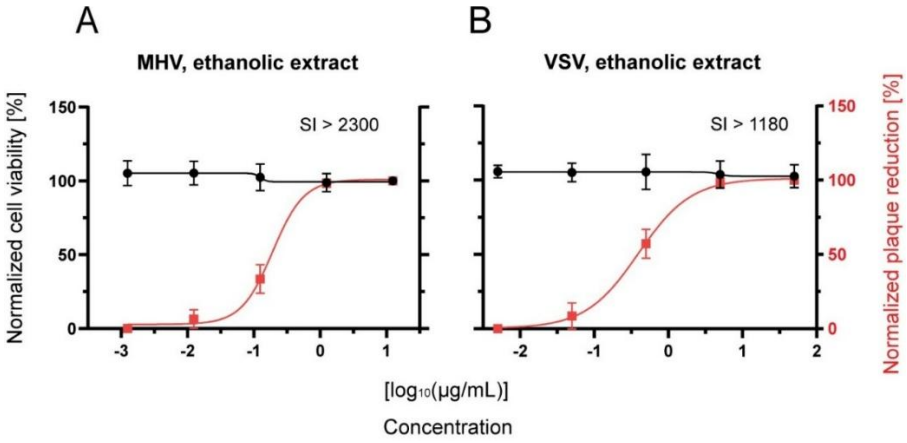


Figure 16: Antiviral activity of the ethanolic extract against MHV and VSV. Results of plaque reduction assays and time-of-addition (ToA) assays following infection with murine hepatitis virus (MHV) (MOI = 0.001) **(A)** or vesicular stomatitis virus (VSV) (MOI = 0.0005) **(B)**. Cells were treated with serial dilutions of the ethanolic extract under co-treatment conditions. Plaque reduction (red squares) was normalised to the mean infection ratio of vehicle-treated infected cells (medium). Cell viability (black dots) was normalised to untreated cells. Error bars represent the standard deviation (SD) of three biological replicates (N = 3). The selectivity index (SI) is indicated for each treatment.

3.2.3.3 The effect of the ethanolic extract on the viral replication of MHV

As the ethanolic extract showed potent antiviral activity when co-treated with MHV, we monitored viral replication by quantitative PCR (qPCR). Total RNA was extracted from supernatants collected at 1, 12, 24, and 48 h post-infection (hpi).

Quantification of MHV RNA was enabled by a standard curve generated from a dilution series of a known viral RNA sample (described in Section 3.2.2.2).

As expected, the viral RNA levels in the infected cells increased over time (Figure 17). At 1 hpi, MHV RNA levels were close to the limit of detection (~1 copy/µL) for all the treatments. By 12 hpi, viral RNA levels in the positive control (untreated infected samples) had increased by approximately two orders of magnitude, reaching up to 6.6×10^3 copies/µL. Viral RNA continued to accumulate over time, rising to 6.6×10^6 copies/µL at 24 hpi and 5.1×10^7 copies/µL at 48 hpi in the positive control. Treatment with the ethanolic extract at both high (50 µg/mL) and moderate (5 µg/mL) concentrations significantly reduced MHV RNA levels compared with the positive control at all time points except 1 hpi, when all samples were near the detection limit. Treatment at the high concentration maintained RNA levels near the detection limit throughout, whereas the moderate concentration showed a gradual increase in MHV RNA levels over time. In contrast, treatment with the low concentration (0.5 µg/mL) of the ethanolic extract resulted in higher viral RNA levels that did not differ significantly from those of the positive control (Fig. 17).

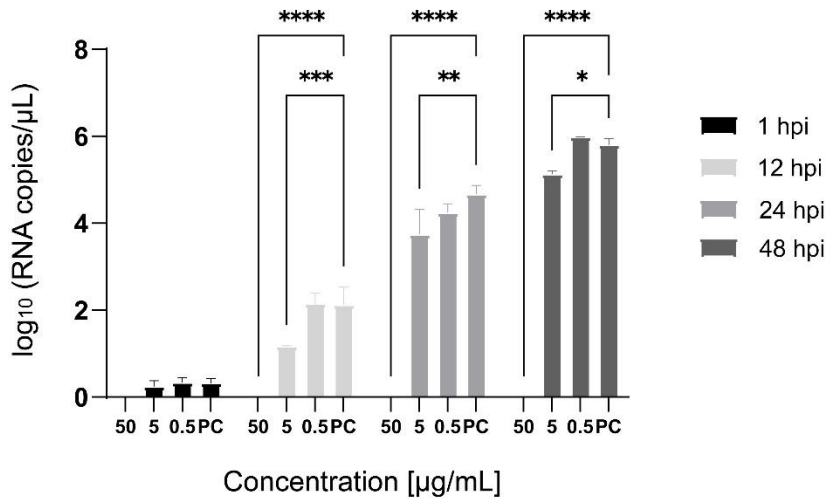


Figure 17: Effect of the ethanolic extract on MHV RNA levels. Viral replication of murine hepatitis virus (MHV) was monitored at 1, 12, 24, and 48 h post-infection (hpi). MHV (MOI 0.001) was co-incubated with the ethanolic extract (50, 5, and 0.5 µg/mL) before cell inoculation. Medium-treated infected cells served as the positive control (PC). Columns represent the mean $\log_{10}$(RNA copies/µL), and error bars indicate standard deviation (SD) of two biological replicates (N = 2), each measured in two technical replicates (n = 2). *P ≤ 0.03, **P ≤ 0.002, ***P ≤ 0.0002, ****P ≤ 0.0001 (two-way ANOVA followed by Dunnett's test).

3.2.3.4 Tentative identification of compounds by mass spectrometry

MS/MS analysis of the *H. italicum* ethanolic extract revealed a phenolic-rich profile, dominated by hydroxycinnamic acid derivatives and flavonoids (Supplementary Table 4 and Supplementary Figure 11), consistent with chemical patterns reported for *H. italicum* ethanolic extracts and distinct from the terpenoid-rich essential oil and hydrosol fractions [92], [99].

3.2.3.4.1 Hydroxycinnamic acids (chlorogenic acid derivatives)

Chlorogenic acids (CGAs) form a large and structurally diverse class of phenolic compounds, with caffeoylquinic acids (CQAs) as their most characteristic representatives. CQAs are conjugates of tetrahydroxy-cyclohexane carboxylic acid (quinic acid) and 3,4-dihydroxycinnamic acid (caffeic acid). Quinic acids can form mono-, di-, or tri-esters, resulting in di- or tri-caffeoylquinic acids, or they can esterify with other trans-hydroxycinnamic acids [99], [208].

Based on fragment ion abundances and comparison with literature data, compound 1 was tentatively identified as 3-O-CQA isomer (neochlorogenic acid) and compound 2 as 5-O-CQA (chlorogenic acid), the most abundant CGA found in nature [99], [209], [210]. Another compound (5) with the same pseudomolecular ion (*m/z* 353) exhibited markedly different fragmentation behaviour. In this case, fragment ions at *m/z* 173 and 179 were highly abundant, a pattern characteristic of 4-O-CQA. Previous studies have reported that CGAs readily interconvert, particularly during extraction processes at elevated temperatures and in aqueous media. Chlorogenic acid (5-O-CQA) not only isomerises to 3- and 4-O-CQA but also undergoes other transformations, such as esterification and hydrolysis [211].

Dicaffeoylquinic acids (di-CQAs) were detected at longer retention times and were characterised using established identification keys and previously published data [116], [209], [212]. Di-CQAs exhibited a pseudomolecular ion at *m/z* 515 and produced characteristic fragment ions at *m/z* 353, 191, 179, and 173, corresponding to the successive loss of caffeoyl moieties. The relative intensities of the fragment ions – particularly at *m/z* 191, 179, and 173 – enabled differentiation among positional isomers such as 1-, 3-, and 4-di-CQAs. Compounds 15–17 were tentatively assigned as 1,3-diCQA derivatives, while compound 8 was identified as 3,4-diCQA, consistent with reports on *H. italicum* alcoholic extracts [99], [101], [213].

Several uncommon CQA derivatives were identified as well. Compound 20 was assigned as tricaffeoylhexaric acid based on its molecular ion at *m/z* 695 and characteristic product ions at *m/z* 533 and 371. This tentative identification is consistent with previous reports describing these rare derivatives in Asteraceae species [99], [214], [215]. Similarly, compounds 9 and 10, which exhibited a molecular ion at *m/z* 533, were putatively identified as dicaffeoylhexaric acids, while compound 7 was identified as caffeoylhexaric acid. Compound 19 was characterised as another CQA derivative with a pseudomolecular ion $[M–H]^-$ at *m/z* 601 and major fragment ions at *m/z* 577, 395, 191, 179, and 173, and was identified as 1,3-dicaffeoylquinic acid malonyl [216].

3.2.3.4.2 Flavonoids and their glycosides

Compound 11 was tentatively identified as myricetin 3-*O*-glucoside based on fragment ions at *m/z* 317 and 316, which indicate the neutral loss of a hexoside moiety and produce fragments characteristic of the myricetin aglycone. Compound 12 was assigned as isorhamnetin 3-*O*-glucoside, supported by its pseudomolecular ion at *m/z* 477 and a dominant MS^2 fragment at *m/z* 315. Similarly, compound 14 was identified as quercetin 3-*O*-glucoside, as indicated by the characteristic MS^2 fragment at *m/z* 301 corresponding to the quercetin aglycone. Compound 21 exhibited a pseudomolecular ion at *m/z* 463 and a major fragment at *m/z* 301, consistent with the loss of a coumaroyl-hexose moiety, and was therefore tentatively identified as quercetin-*O*-coumaroylglucoside. All of these flavonoid glycosides have previously been reported in *H. italicum* extracts [98], [99], [105], [116], [217].

Chapter 4

Discussion

Despite advances in antiviral development, the rapid evolution of SARS-CoV-2 continues to compromise drug efficacy, emphasising the need for therapeutics less susceptible to antiviral resistance. Among the structural proteins, SARS-CoV-2 Epro has the lowest mutation frequency and the greatest resistance to mutagenic pressure [23], [24], [25], [218], and represents a promising yet under-investigated antiviral target. We combined *in silico* approaches, such as molecular docking and molecular dynamics simulations, with *in vitro* characterisation to better assess the antiviral potential of selected candidates and address the limitations of computational predictions alone.

In addition to synthetic small molecules, we explored the antiviral potential of *Helichrysum italicum* extract as an alternative source of antivirals, particularly given the known biological activity of its phenolic constituents. The following discussion evaluates these findings and considers their relevance for the future development of broad-spectrum antiviral strategies.

4.1 Characterisation of Antiviral Candidates

Currently, the number of SARS-CoV-2 Epro inhibitors confirmed *in vitro* and *in vivo* is limited [21], [36], [59], and there are no approved COVID-19 drugs targeting this protein (Table 1) [219]. One reason for this is the limited attention it has received in the past, which has left researchers with only a few compounds to work with. Additionally, many compounds exhibit cytotoxicity [21], thereby excluding them from further clinical development. This limitation was observed for HMA, which has otherwise been shown to act against several viroporin-forming viruses, including HIV-1, IAV, hepatitis C virus, and coronaviruses [53], [54], [55], [56], [65]. An interesting chemical is amantadine (AMT), a drug approved for the treatment of Parkinson's disease. It was previously used for IAV infections until widespread resistance in viral strains limited its effectiveness. Interestingly, its antiviral effect is mediated by inhibition of the influenza A matrix protein 2 (M2), an ion channel involved in the release of the viral genome into the host cell [220], [221]. Rimantadine (RMT) is also a well-characterised inhibitor of the M2 protein of IAV; however, widespread resistance due to M2 mutations has led to its discontinuation as a therapeutic option for IAV [222]. Nevertheless, AMT and RMT showed *in vitro* activity against SARS-CoV-1 and SARS-CoV-2 by inhibiting Epro [21], [59], [62], [64], [65]. Although smaller studies initially suggested that AMT and RMT could be suitable candidates for the treatment of SARS-CoV-2 infections [223], [224], a more recent large-scale observational study found no significant clinical benefit of them for COVID-19 patients with early-stage SARS-CoV-2 infection [225]. These findings point to the need for novel inhibitors with improved antiviral properties.

4.1.1 The ZINC15 database

Our proposed ligands are from a set of candidates we identified during screening of the entire ZINC15 database, which at that time contained 997,402,117 molecules. We hereby covered a large chemical space spanning multiple classes of small molecules, including metabolites, drugs, and natural products [173]. In the subsequent filtering step, we selected druglike molecules and excluded compounds with known cytotoxic motifs and those exhibiting promiscuous binding behaviour [177], [178], [179], [180]. We have used a visualisation approach that focuses on common functional-group motifs, allowing us to explore the biologically relevant chemical space and monitor subsequent actions that lead to the selection of final candidates. Our filtered molecules underwent re-docking, followed by classical MD simulations and MM-PBSA analysis, on three selected top-scoring candidates.

Clustering and MM-PBSA analysis of the candidates revealed intermolecular interactions with the residues ASN15, ALA12, THR11, and GLU8 of the SARS-CoV-2 Epro pentameric viroporin. Previous studies underscore the importance of ASN15, the first pore-facing and channel-restricting amino acid at the N-terminus. It has been shown to interact with several experimentally confirmed inhibitors, including HMA, AMT [26], [59], and procyanidin [52]. Notably, ASN15ALA mutations in SARS-CoV-1 Epro abolished ion conductance [26], [226], [227], highlighting the importance of this residue in the channel's ion transport mechanism. Interactions with THR11 were also observed experimentally for HMA and procyanidin, with THR11ALA mutants of SARS-CoV-2 Epro exhibiting significantly reduced viral replication and virulence due to the absence of Epro ion-channel currents [36]. Finally, GLU8, an exposed amino acid at the N-terminus, was found to interact with procyanidin [52]. In addition, the flexible ring formed by the five GLU8 residues is thought to be an important regulatory part of the channel's cation selectivity filter [26]. Our MD simulations indicate that two of the eight candidates block the SARS-CoV-2 Epro ion channel for extended periods by forming hydrogen bonds with ASN15 and THR11. Binding affinities were calculated for these candidates, with L3 and L2 emerging as the most promising, showing more favourable binding than RMT at the C- and N-terminal vestibule under the present simulation conditions.

Despite their structural similarity to the computationally prioritised candidates, the tested commercially available analogues did not exhibit detectable antiviral activity *in vitro*. This suggests that the predicted interactions within the E protein channel may be highly specific and sensitive to subtle structural features not retained in the commercially available analogues. Alternatively, these compounds may not be active against MHV under the tested conditions. These findings highlight the limitations of structure-based virtual screening in predicting functional antiviral activity and underscore the importance of experimental validation.

4.1.2 FKKTLib

In this part of the thesis, we identified a novel SARS-CoV-2 Epro inhibitor using an *in silico* approach and further characterised its antiviral activity against a model coronavirus (MHV) *in vitro*, showing EC_{50} values in the same general micromolar range as those of the known broad-spectrum coronavirus inhibitors HMA and RMT.

4.1.2.1 The lead candidate forms a stable complex with the SARS-CoV-2 Epro N-terminal vestibule with high binding affinity

As a starting point for this search, we performed *in silico* analyses to explore the potential of our lead candidate (LC), a functionalised adamantane connected to an indole group and an aliphatic chain via an amide linker. LC and RMT were subjected to classical MD simulations and MM-PBSA analysis. Clustering and MM-PBSA analysis of the SARS-CoV-2 Epro–ligand trajectories revealed that LC primarily engages residues located in the N-terminal vestibule, including GLU8, THR9, THR11, ASN15, and LEU18. Several of these residues (GLU8, THR11, and ASN15) were previously identified as key determinants of ion channel function and inhibitor binding (Section 4.1.1) [26], [36], [52], and their involvement here further supports the N-terminal region as a primary binding site. In particular, ASN15 and THR11, which are central to pore constriction and ion conductance, form persistent interactions with LC, consistent with their established functional importance [26], [36], [226], [227]. In addition to these well-characterised residues, LC also interacts with THR9, a residue at the dynamic N-terminus. THR9 was found to strongly interact with HMA [26], supporting its importance as an inhibitor-binding residue. LEU18, a hydrophobic residue that forms a narrow stretch (pore radius of ~2 Å) of the channel along with LEU21, VAL25, and LEU28 [26], was found to interact strongly with other adamantanes such as adapalene and RLA-3107 as well as with artefenomel [60]. RMT predominantly interacts with residues located in the C-terminal vestibule, including LEU28, ALA32, and THR35, consistent with previous observations for memantine and dopamantine (two adamantane derivatives) [60].

We further note that the persistent interactions of ARG38 with POPC headgroups suggest that the C-termini act as membrane anchors, helping stabilise the position and orientation of the Epro ion channel within the bilayer. By forming strong salt bridges with the lipid phosphate groups, ARG38 may effectively "lock" the C-terminal region at the membrane interface and pre-organise the C-terminal vestibule. Similarly, other viroporins are well known to anchor to the lipid bilayer by terminal positively charged residues such as lysine or arginine [228]. In this context, the stable binding of the positively charged RMT ligand in the immediate vicinity of ARG38, despite potential electrostatic repulsion, indicates that the overall local environment – comprising ARG38, nearby residues, and the lipid headgroups – creates a net stabilising interaction network. Thus, ARG38–lipid contacts may not only anchor the protein but also indirectly support the retention of positively charged ligands, such as RMT, at the C-terminal binding site. A mutational study by Steinmann *et al.* on the hepatitis C virus p7 viroporin has highlighted a similar role for conserved basic residues at the membrane interface, stabilising the proper protein's orientation in the membrane via electrostatic interactions with the negatively charged phosphate groups of lipid headgroups. Upon replacement with neutral amino acids, production of infectious viral particles was dramatically suppressed, suggesting an important role for basic amino acid motifs positioned near the lipid headgroups at the membrane interface [229]. We note that the present simulations employ a simplified membrane model consisting of a homogeneous POPC bilayer. Real ERGIC/Golgi membranes are compositionally complex and may contain other components such as cholesterol and anionic lipids [230] that influence membrane properties and protein conformational equilibria. While such effects are not explicitly captured here, the chosen model enables controlled, reproducible comparison of ligand binding in a consistent environment. The incorporation of lipid heterogeneity thus represents an important direction for future studies.

The MD simulations indicate that LC blocks the SARS-CoV-2 Epro ion channel for an extended period by forming stable complexes in the N-terminal vestibules. Binding

affinities were calculated for LC, showing a more favourable binding affinity than for RMT in the C-terminal vestibule under the present simulation conditions, by a factor of 1.7. We note that the C- and N-terminal vestibules face the cytoplasm and ERGIC lumen, respectively; thus, binding-site preference could modulate both blockade efficacy and compartmental access. However, a detailed elucidation of its pharmacodynamic implications is outside the scope of this study.

4.1.2.2 The lead candidate inhibits MHV infectivity

MHV is used as a surrogate because it is a close phylogenetic relative of SARS-CoV-2; both viruses share similar structural features, exhibit comparable infection-related pathogenic processes, and can cause similar severe pathological outcomes [155], [156], [157]. LC reduced MHV infectivity *in vitro* in a dose-dependent manner and exhibited strong antiviral activity, with an EC_{50} of 12 μM, as confirmed by plaque reduction assays. LC exhibited selectivity indexes (SIs) of a similar order to those of RMT and HMA in this assay system, highlighting its efficacy as a competitive antiviral candidate. ToA experiments indicated that all three compounds act in the late stages of the MHV life cycle, which is consistent with previous findings and the known role of Epro [61], [68]. In addition, the potent activities of LC and HMA at co-treatment suggest that they either interfere with the entry stages of the viral cycle or interact with virus particles in a virucidal manner, possibly inactivating the virus before cellular infection [168].

Regarding the antiviral efficacy of HMA and RMT, our results are consistent with previous reports describing similar efficacy values [55], [231]. Breitinger *et al.* [21], [59] also showed that HMA, RMT, and AMT inhibit both SARS-CoV-1 and SARS-CoV-2 Epro *in vitro*, with HMA found to be the most potent – a trend reflected in our results as well. The ratio of RMTs' and HMAs' EC_{50} values in our study (3.4) is comparable to previously reported ratios for SARS-CoV-2 Epro (6) and SARS-CoV-1 Epro (4). It underscores consistency across coronaviruses and experimental systems, despite methodological differences [21], [59]. Furthermore, RMT was found to be less cytotoxic than HMA, consistent with previous studies showing that adamantanes such as RMT and AMT generally have lower cytotoxicity [21], [232], [233].

4.1.2.3 The lead candidate transiently delays MHV RNA replication

We observed that MHV RNA replication was delayed in infected cells treated with LC. Significantly lower RNA levels were detected at 24 h post-treatment compared to untreated infected controls. We observed similar results for HMA and RMT, indicating that Epro plays a role in viral replication, although the tested inhibitors did not completely block viral replication. Kuo *et al.* [30] and DeDiego *et al.* [234] reported that MHV and SARS-CoV-1 E-gene deletion mutants had infectious titres three orders of magnitude lower, as demonstrated *in vitro* and *in vivo*, concluding that Epro is critical but not essential for viral replication [30], [234]. Previous studies show that SARS-CoV-1 Epro contributes to virulence, particularly through the PDZ-binding motif (PBM), a C-terminal domain that mediates protein–protein interactions and modulates signalling pathways implicated in pathogenesis [235]. Alvarez *et al.* [236] reported that SARS-CoV-2 PBM mutants exhibit delayed replication (at 24 and 32 h post-infection) *in vitro* and cause less weight loss, lower viral load, significantly attenuated inflammatory responses, and milder respiratory damage *in vivo* [236]. Similarly, reduced lung inflammation was reported *in vivo* for SARS-CoV-1 Epro mutants [234]. Taken together, these results suggest that Epro's contribution to

virulence cannot be explained by replication efficiency alone and is closely linked to inflammation.

4.1.2.4 Lead candidate prevents cell lysis by attenuating MHV release

Light microscopy and TEM analysis showed that LC strongly reduces virion release and consequently prevents cell lysis. Consistent with our qPCR results, LC did not have a strong effect on viral genome replication at 48 h post-treatment, as we observed virus-induced changes comparable to those at the positive control. Similarly, Ortega *et al.* [237] reported that, despite successful viral genome replication, deletion of Epro in transmissible gastroenteritis coronavirus (TGEV) led to two distinct effects: blockade of viral transport across the membranes of the secretory pathway and impaired virion maturation. As in our study, an accumulation of virions in intracellular compartments was observed, supporting a role of Epro in virus post-replication phases. Recent work also shows that β-CoVs use lysosomes for egress, with Epro migrating from the Golgi to the lysosomes, where its viroporin activity inhibits acidification and promotes efficient virus release [238], [239], [240], [241]. According to Pearson *et al.* [239], mutations in the C-terminal region of SARS-CoV-2 Epro cause it to remain in the endoplasmic reticulum, thereby hindering its transport to the lysosomes. The conserved hydrophobic residues in the C-terminal region suggest that ER export is a universal CoV mechanism that enables viral assembly [239]. Despite evidence showing that Epro cooperates with M protein to ensure efficient assembly [242], studies have shown that expression of Epro alone can drive vesicle formation and induce membranous structures resembling those in infected cells, suggesting that it can act independently of other viral components [32], [243], [244], emphasising the essential role of Epro in morphogenesis, maturation, assembly, and release of the virions.

There are still groups at risk of developing life-threatening COVID19 complications, such as cancer patients, for whom the Omicron strain was the deadliest in the US compared to all previous SARS-CoV-2 strains [245]. Herein, SARS-CoV-2 Epro is an antiviral target that plays an important role in viral replication and pathogenesis. The consistency of our study with experimental findings from previous studies emphasises the relevance of our findings and the potential antiviral properties of the LC. Taken together with the suspected presence of other viroporins in SARS-CoV-2 [246] and the frequent occurrence of viroporins across a diverse range of viruses, these findings may point to pathways for developing antiviral drugs with pan-corona or even broad-spectrum activity. Many pathomechanistic details of SARS-CoV-2 are still being uncovered, such as recent findings suggesting that several variants can form stable complexes with monoamine oxidase enzymes (MAOs) [247], potentially disrupting their function and contributing to oxidative stress and neurodegenerative processes in COVID-19-related neurological complications [248], [249], [250], [251], [252], [253]. Other examples include evidence that SARS-CoV-2 Epro alters ER calcium homeostasis by interfering with the function of the sarco/endoplasmic reticulum calcium ATPase, thereby mimicking host regulins and reducing ER Ca^{2+} reuptake [254]. This illustrates the need for further research to elucidate the full spectrum of virus–host interactions and their implications for long-term disease outcomes and the design of novel therapeutic strategies.

4.1.3 Antiviral potential of *Helichrysum italicum*

Natural products are an important complementary source of antiviral compounds, particularly as plant-derived extracts contain diverse bioactive molecules that may act through multiple mechanisms. In this context, we investigated *Helichrysum italicum* for its antiviral potential against both enveloped and non-enveloped viruses, with particular attention to the activity of its ethanolic extract and major phenolic constituents. The

following discussion examines the observed antiviral effects in relation to extract composition, potential mechanisms of action, and the contributions of individual compounds, such as quercetin.

4.1.3.1 *H. italicum* ethanolic extract inhibits MHV and VSV infectivity

The differences in the extracts' activity can be attributed to their chemical composition. The ethanolic extract's potent antiviral activity can be explained by the fact that ethanol, as a solvent, efficiently extracts both polar and moderately lipophilic phenolic compounds, including flavonols such as quercetin and a wide range of hydroxycinnamic acid derivatives [99]. Hot-water extracts primarily extract highly polar constituents such as chlorogenic acid and quinic acid. Still, they may promote the degradation or isomerisation of labile compounds due to elevated temperatures, thereby reducing antiviral potency [98], [99]. Essential oils and hydrosols, by contrast, are dominated by volatile terpenes and contain low amounts of non-volatile phenolics, which are increasingly recognised as contributors to virucidal and entry-inhibitory effects against viruses, especially the enveloped ones [92], [99], [255], [256].

Previous reports indicate that the antiviral activity of ethanolic extracts varies across *Helichrysum* species. Kutluk *et al.* reported that, among seven *Helichrysum* species ethanolic extracts, only *H. arenarium* and *H. armenium* DC exhibited virucidal activity against HSV-1 and parainfluenza virus type 3 (PIV-3) at concentrations of 2–32 and 4–64 µg/mL, respectively [134]. Lall *et al.* reported that *H. melanacme* ethanolic extract exhibited antiviral activity against IAV with an IC_{50} of 10 µg/mL, which is comparable to results for PIV-3 [133], [134]. Ethanolic extracts of *H. cymosum* (L.) Less. (Compositae) and *H. foetidum* (L.) Moench var. microcephalum A. Rich. (Compositae) were active against several enveloped viruses, including HSV-1, and Semliki Forest virus A7 (SFA7), but not against the enveloped measles virus strain Edmonston A (MV-EA) and the vesicular stomatitis virus T2 (VSVT2), and non-enveloped polio type 1 and coxsackie B2 viruses [132].

In the studies mentioned [132], [133], [134], virucidal activity was primarily inferred from co-incubation assays of the virus with the extract before infection. While such assays are suitable for detecting inhibitory effects before or during early infection, they do not necessarily distinguish between true virucidal activity and interference with early entry processes. In contrast, the additional dilution-based experiments performed in the present study enabled differentiation between these mechanisms. They provided further insight into the mode of antiviral action during early steps of the MHV life cycle.

The strong antiviral activity observed against both enveloped viruses tested in our study, together with the lack of effect on non-enveloped MNV, indicates envelope-dependent susceptibility. Phenolic-rich plant extracts frequently exhibit greater antiviral activity against enveloped viruses compared to non-enveloped viruses, a trend consistently reported in comparative antiviral screening studies [257], [258], [259]. This selectivity could be attributed to interactions with the viral envelope or envelope glycoproteins, leading to membrane destabilisation or inhibition of viral attachment and fusion. Non-enveloped viruses may nevertheless be affected by phenolic-rich extracts. For example, polyphenol-rich grape seed extract and persimmon tannin-rich extract have been shown to inactivate poliovirus and norovirus by inducing viral protein aggregation [260], [261], [262], supporting mechanisms distinct from envelope disruption.

4.1.3.2 *H. italicum* ethanolic extract suppresses MHV RNA replication

Our qPCR results demonstrate that the ethanolic extract exhibits dose-dependent antiviral activity against MHV, with complete suppression of viral RNA at high concentration (50 µg/mL) and significant inhibition at moderate concentration (5 µg/mL). As experiments were conducted under co-treatment conditions, these findings suggest that the ethanolic extract acts at an early stage of the viral replication cycle, likely by preventing viral attachment or entry, or by directly inactivating virions. This interpretation is supported by the significant reduction in viral infectivity observed in the plaque reduction assay and time-of-addition assay under co-treatment conditions. Our results are consistent with previous reports on ethanolic extracts of *Helichrysum* species [133], [134]. Similar early suppression of coronavirus replication has been reported for several plant extracts quantified by qPCR, suggesting either virucidal activity or interference with early stages of viral entry. Extracts rich in flavonoids, terpenoids, and polysaccharides may interact with viral proteins, inhibit viral attachment or membrane fusion [263], or compromise envelope integrity, as demonstrated for SARS-CoV-2 and influenza virus treated with *Prunus mume* fractions [264]. However, the molecular mechanisms underlying the inhibition of viral RNA replication by plant extracts remain largely unknown.

4.1.3.3 Quercetin inhibits MHV at the early entry stages of the viral cycle

Quercetin, like the ethanolic extract, exerts antiviral activity against MHV by interfering with the early stages of virus–cell interaction, such as viral attachment or entry. This flavanol is found in various plants and has well-documented antiviral potential [265], [266], [267]. Previous *in vitro* studies have confirmed its virucidal activity and inhibition of influenza viral entry [265], [266]. Against SARS-CoV-2, quercetin showed virucidal activity, reduced viral replication *in vitro* (SI = 17) [267], and involved the envelope protein [59], while *in silico* studies suggested interactions with the spike and membrane proteins [268], [269]. The mechanisms of action include inhibition of viral entry into cells, binding of capsid proteins to genomic nucleic acids, and inhibition of viral polymerases and other proteins [268], [270]. In a study by Chiow *et al.*, quercetin unexpectedly showed poor virucidal activity against MHV (strain unspecified) in the CCL9.1 cell line (SI = 0.93), as determined by a neutralisation test under the same co-treatment conditions as in our study [271].

However, the other five tested compounds (quinic acid, caffeic acid, chlorogenic acid, arzanol, myricetin), which had been evaluated in our laboratory and reported in an earlier master's thesis [136] and in the present doctoral thesis, showed no antiviral activity. A combination of quinic and caffeic acid was also inactive, suggesting that, beyond quercetin, the antiviral effect of the ethanolic extract may result from multiple synergistic interactions, chemical modifications, or additional constituents not detected by the analytical approach used [272], [273], [274]. Identification of the key contributors to antiviral activity would require bioactivity-guided fractionation and isolation of individual compounds detected by mass spectrometry.

Chapter 5

Conclusions

In this work, we combined computational and experimental approaches to investigate antiviral strategies targeting the coronavirus viroporin and characterised natural product extracts using comprehensive experimental methods.

We performed *in silico* analyses to compare candidate compounds targeting the SARS-CoV-2 E protein (Epro) ion channel. High-throughput virtual screening followed by rigorous filtering initially identified several promising ligands. Among these, molecular dynamics (MD) and molecular mechanics Poisson–Boltzmann surface area (MM-PBSA) analyses identified compounds L2 and L3 as the most favourable, exhibiting intermolecular interactions within the N-terminal vestibule of the Epro pentameric viroporin with the amino acid residues GLU8, THR9, THR11, LEU12, and ASN15. However, the absence of antiviral activity against a surrogate virus, murine hepatitis virus (MHV), observed *in vitro* for structurally related, commercially available analogues underscores the limitations of structure-based predictions and highlights the sensitivity of Epro inhibition to subtle structural features. These findings emphasise the necessity of integrating experimental validation early enough in the drug discovery pipeline.

Extending this approach, the current lead candidate (LC), (*S*)-*N*-(2-((1*S*,3*S*,5*S*,7*S*)-adamantan-2-yl)ethyl)-2-(butylamino)-3-(1*H*-indol-3-yl)propenamide, from the Faculty of Chemistry and Chemical Technology compound library (FKKTLib) demonstrated the highest predicted binding affinity among all candidates evaluated, forming stable interactions within the N-terminal vestibule of the Epro involving key amino acid residues GLU8, THR11, ASN15, and LEU18. Importantly, the computational approach was supported by *in vitro* results on MHV, using techniques such as plaque reduction assays, quantitative PCR, light microscopy, and transmission electron microscopy. EC_{50} of approximately 12 µM was within the same micromolar range as those observed for the reference Epro inhibitors 5-(*N*,*N*-hexamethylene)amiloride (HMA) and rimantadine (RMT). LC reduced viral egress and protected infected cells from virus-induced cytopathic effects. These observations are consistent with impaired Epro channel function, leading to disrupted viral egress and attenuated infectivity. The convergence of *in silico* and *in vitro* findings strengthens the case for LC as a promising compound and further supports viroporin inhibition as a viable antiviral strategy. Given the high structural conservation of E proteins across β-coronaviruses, such inhibitors may offer potential for broad-spectrum antiviral development.

Complementary to the targeted drug discovery approach, we also investigated the antiviral potential of a complex natural product extract. The ethanolic extract of *Helichrysum italicum* exhibited selective antiviral activity against the enveloped viruses MHV and vesicular stomatitis virus (VSV), while no effect against a non-enveloped murine norovirus (MNV) was observed, indicating an envelope-dependent mechanism. Chemical profiling revealed a phenolic-rich composition, and *in vitro* experiments confirmed that quercetin contributes to antiviral activity by acting at the entry stages of the viral life

cycle. However, the extract's overall potency appears to arise from synergistic interactions among multiple constituents, highlighting the complexity and therapeutic potential of plant-derived mixtures.

Future work should focus on further validation and optimisation of these findings. For Epro inhibitors, this includes synthesis and testing of prioritised compounds, electrophysiological characterisation, and evaluation in SARS-CoV-2 system and *in vivo* models to establish efficacy, pharmacokinetics, and safety. For *H. italicum*, bioactivity-guided fractionation and combination studies will be essential to identify active components, define synergistic effects, and ensure reproducibility through extract standardisation.

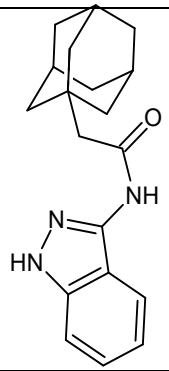
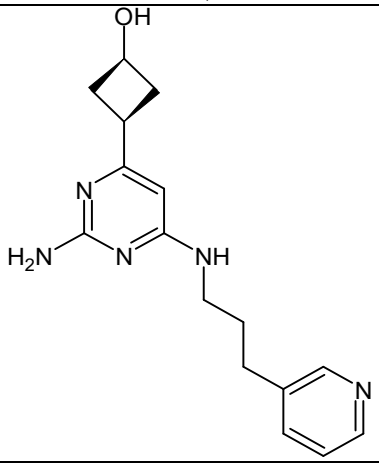
Overall, this thesis underscores the importance of integrating computational techniques with experimental validation. It also highlights the complementary potential of synthetic and natural product-based approaches. Together, these strategies help expand the currently limited repertoire of antiviral agents and support the ongoing development of innovative therapeutics against SARS-CoV-2 and other emerging viral pathogens.

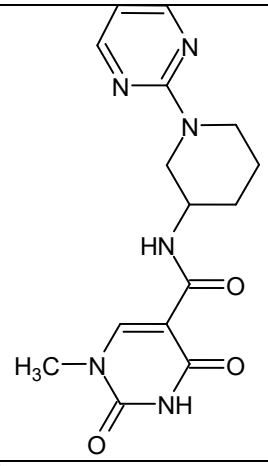
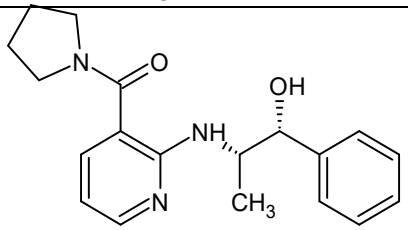
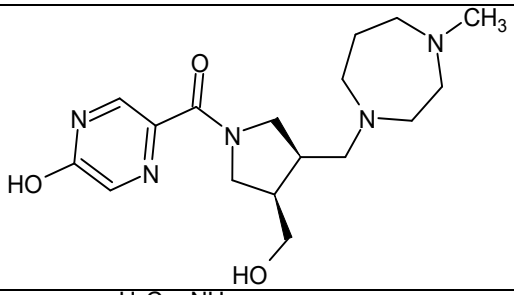
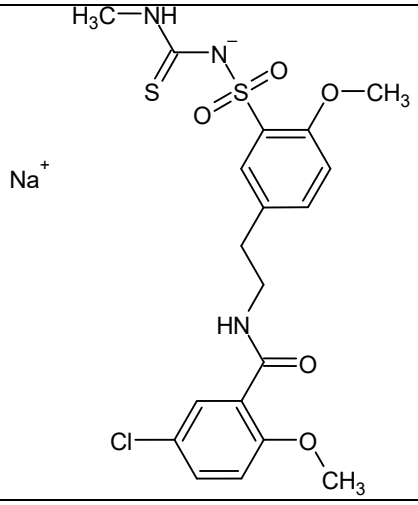
Appendix A

Supplementary Material

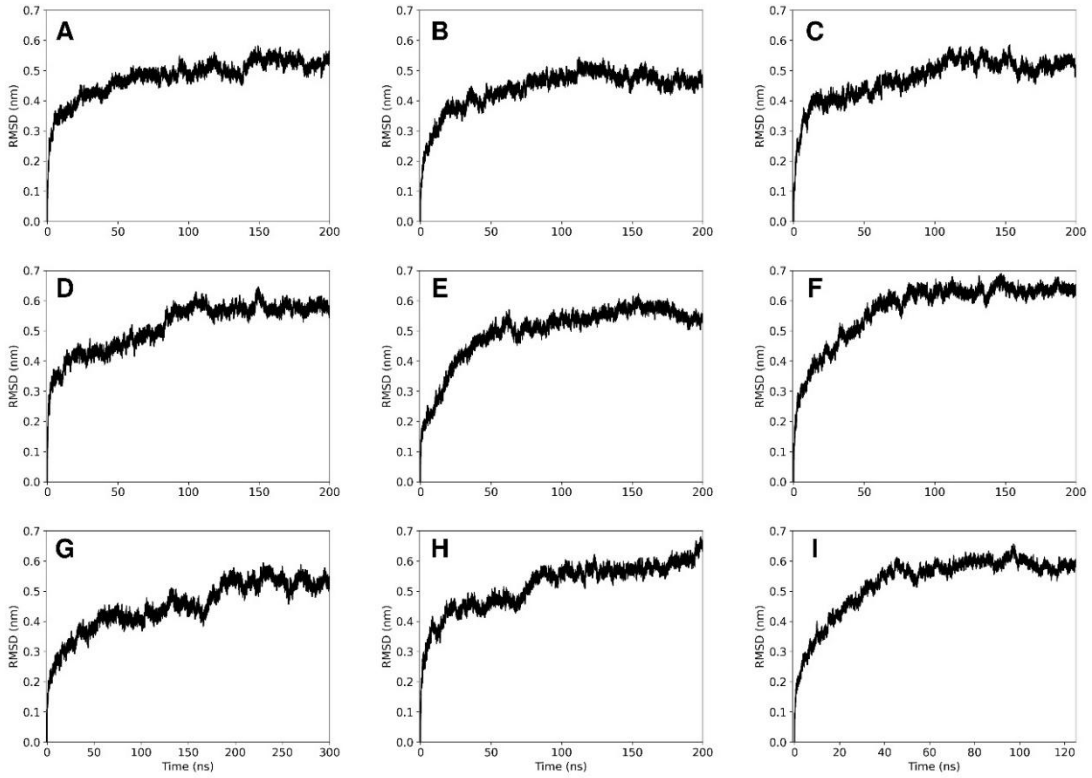
A.1 Supplementary Material for Section 2.3

Supplementary Table 1: Molport IDs and chemical structures of the tested, commercially available compounds with high similarity to the prioritised candidates, chosen from the ZINC15 database. Chemical structures were drawn using ACD/ChemSketch version 2024.2.3 (Advanced Chemistry Development, Canada).

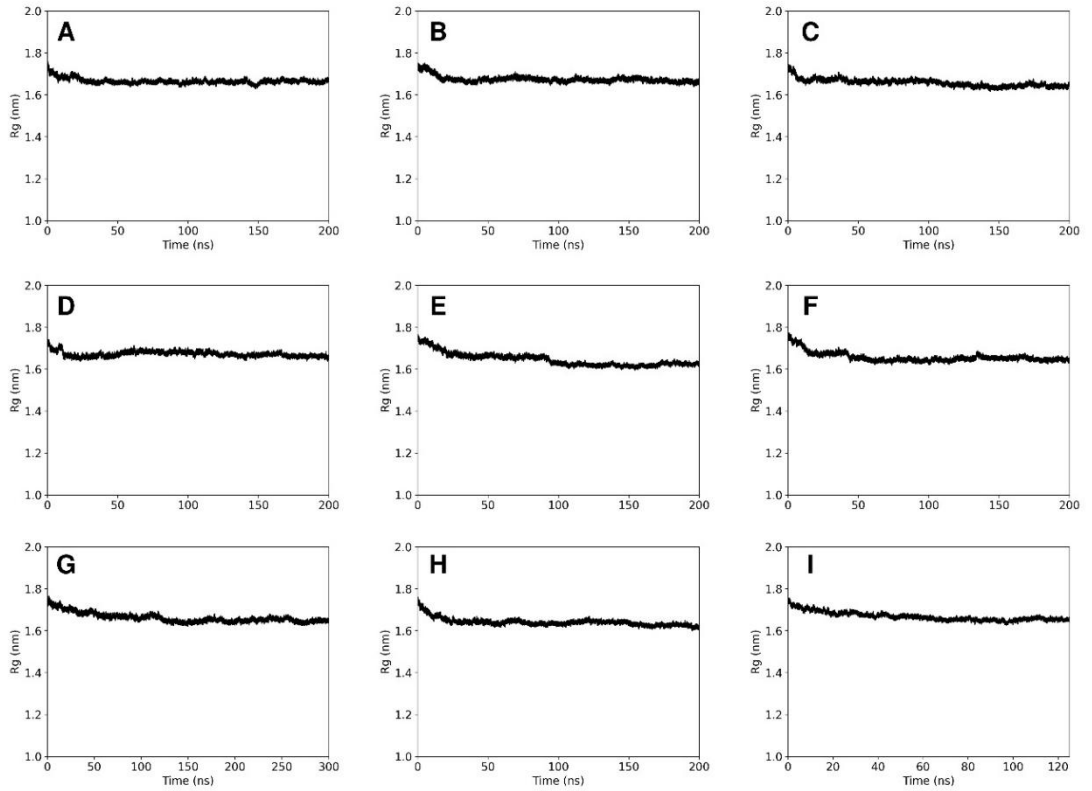
Molport ID	Lead compound	CC_{50} [µM]	Chemical structure
MolPort-027-939-308	L3	40	
MolPort-038-394-572	L4	150	

MolPort-038-419-202	L1	20	
MolPort-046-573-024	L7	>1000	
Molport-027-882-992	L2	>1000	
MolPort-042-665-757	L5	500	

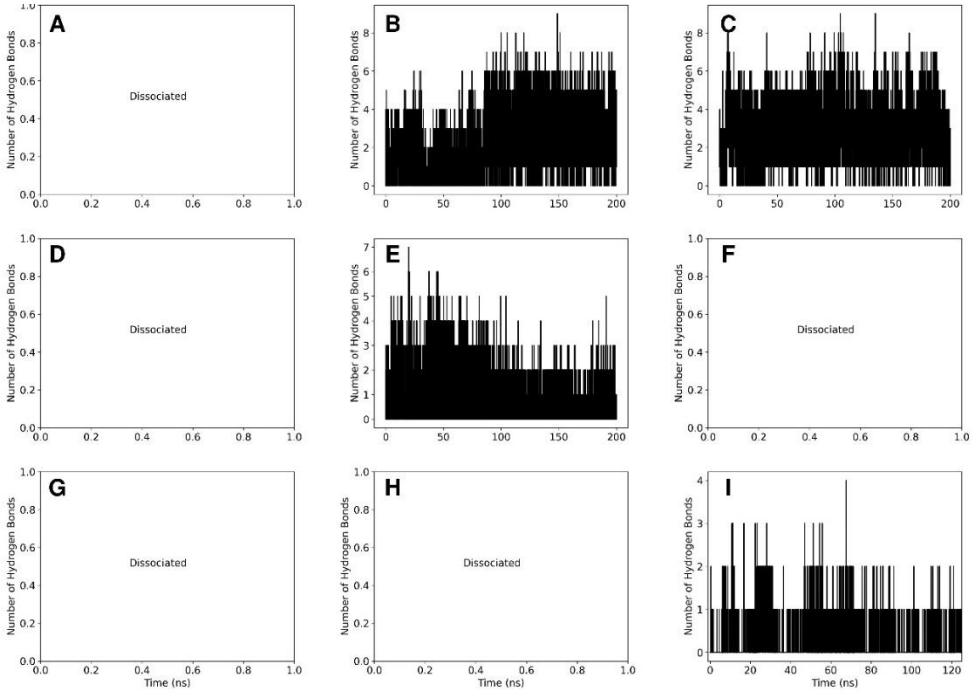
A.2 Supplementary Material for Section 3.1.1



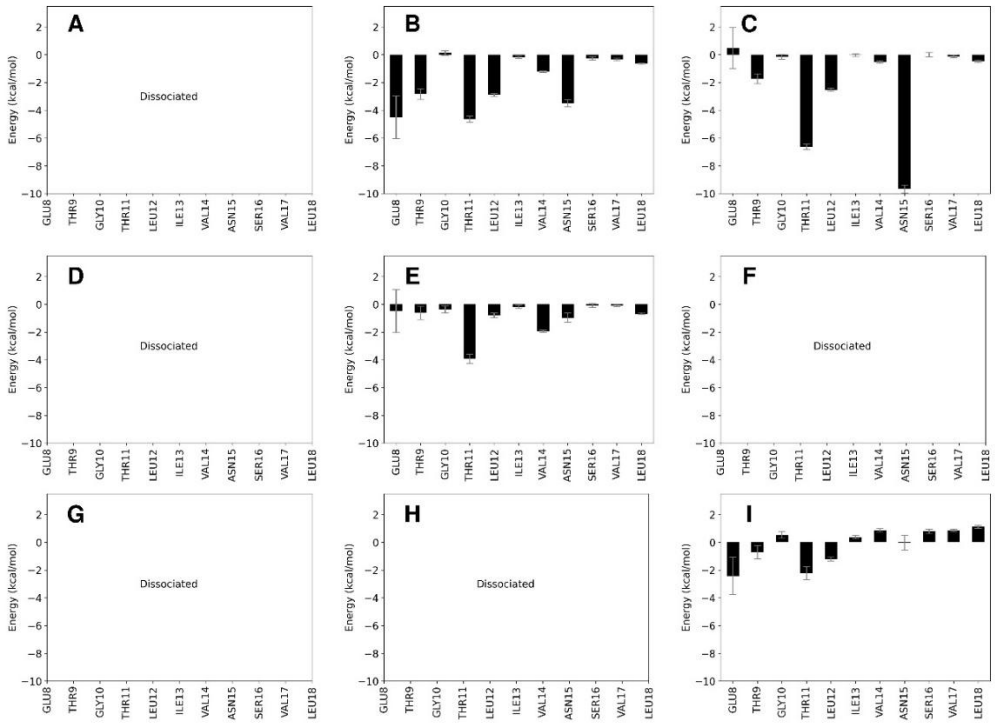
Supplementary Figure 1: Protein's C-α RMSD as a function of simulation time for the final ligand selection of L1–L8 and RMT corresponding to A-I, respectively [27].



Supplementary Figure 2: Protein's radius of gyration as a function of simulation time for the final ligand selection. Labels are the same as in Supplementary Figure 1 [27].



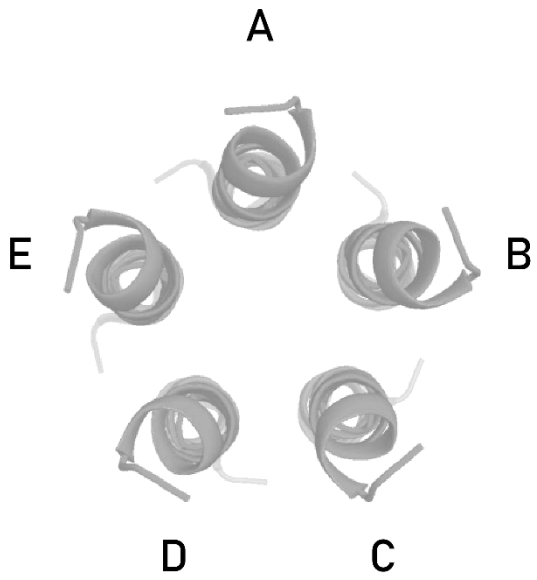
Supplementary Figure 3: Number of hydrogen bonds formed between the protein and the ligand as a function of simulation time for the final ligand selection. Labels are the same as in Supplementary Figure 1 [27].



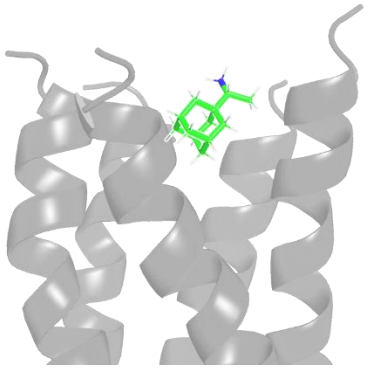
Supplementary Figure 4: Total MM-PBSA per-residue binding free energy contributions for the final ligand selection. Labels are the same as in Supplementary Figure 1 [27].

Supplementary Table 2: MM-PBSA binding free energies of individual protein residues, ΔG_{bind}^{res}, for which ΔG_{bind}^{res} <−1.80 kcal/mol. SARS-CoV-2 Epro subunit labels are shown in Supplementary Figure 5 [27].

Candidate	Residue	ΔG_{bind}^{res} [kcal/mol]
L2	C:LEU:12	-1.8 ± 0.3
	D:GLU:8	-3.5 ± 0.6
L3	B:THR:11	-2.5 ± 0.4
	C:ASN:15	-2.5 ± 0.3
	D:ASN:15	-2.7 ± 0.3
	E:ASN:15	-3.4 ± 0.4
	C:LEU:12	-2.3 ± 0.5

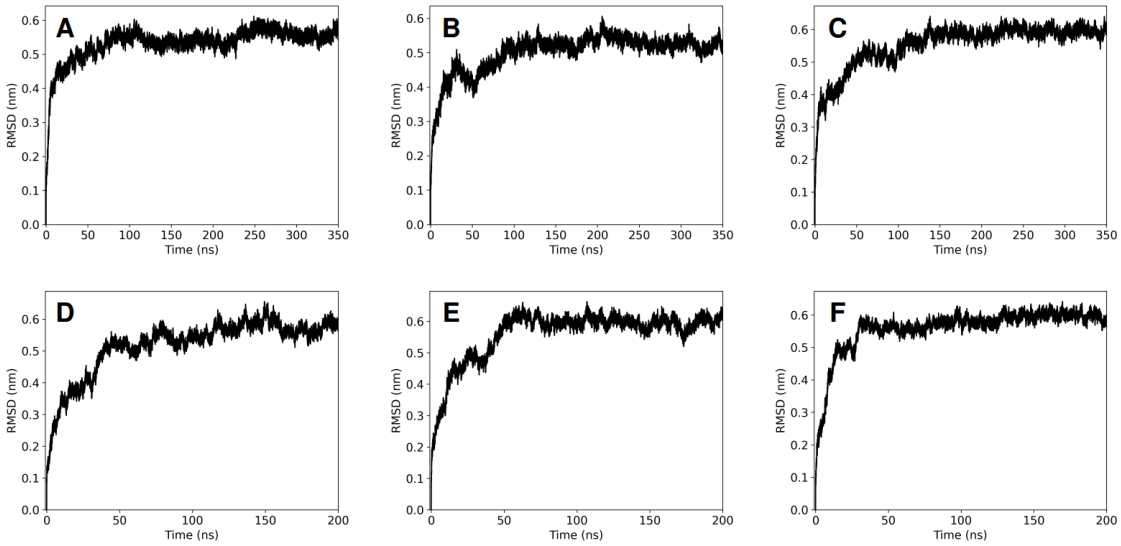


Supplementary Figure 5: Subunit labels of the homopentameric SARS-CoV-2 envelope protein [27].

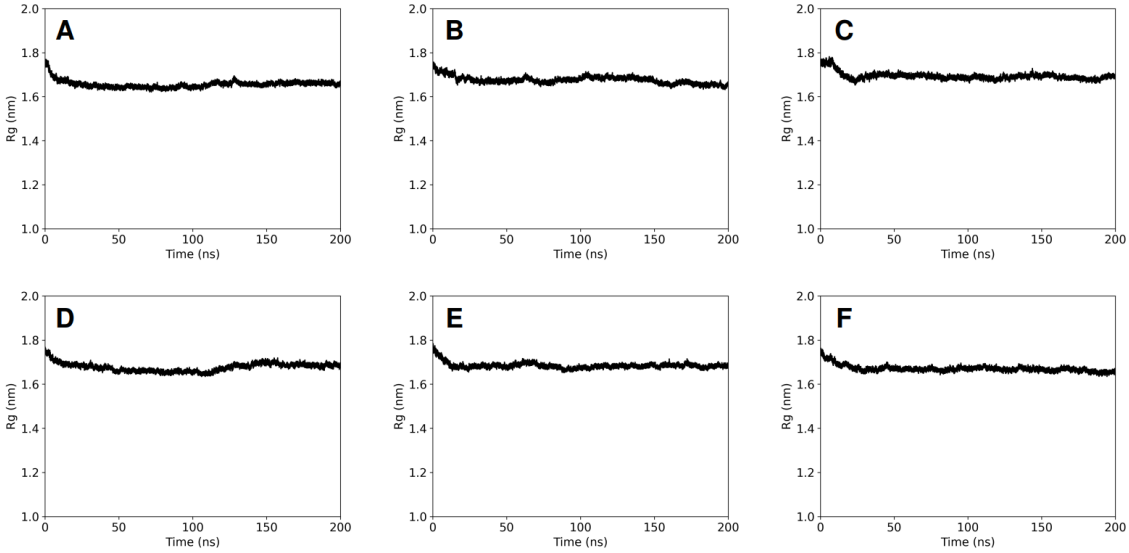


Supplementary Figure 6: Most representative cluster depicting the binding pose of RMT. Protein moieties are depicted in blue [27].

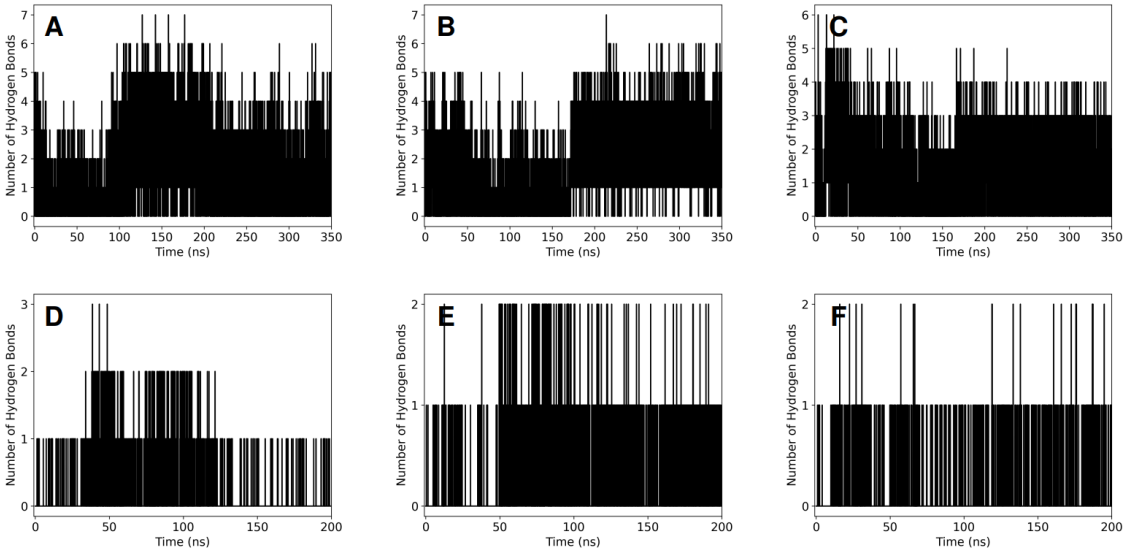
A.3 Supplementary Material for Section 3.1.2



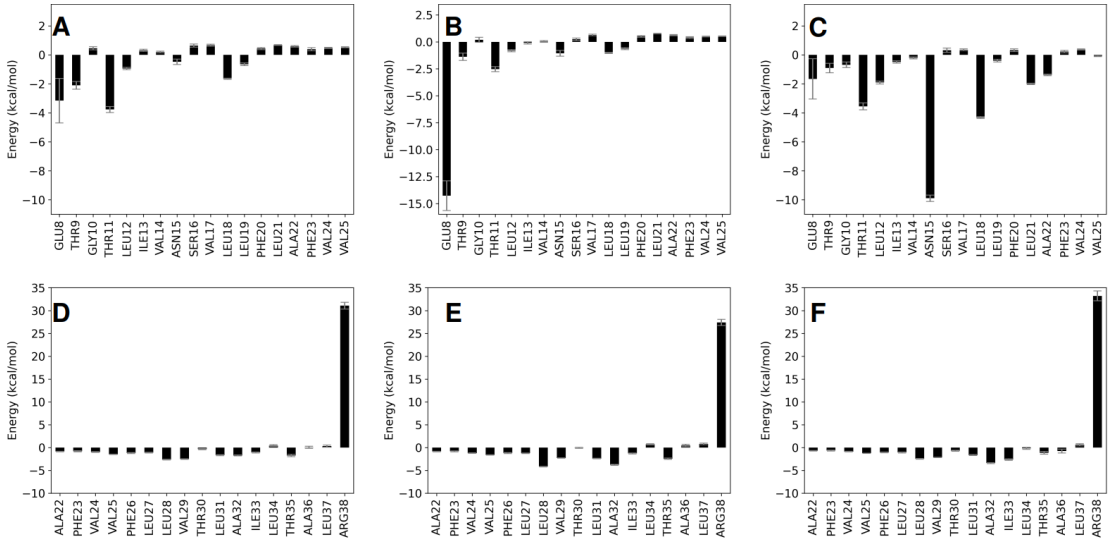
Supplementary Figure 7: Protein's C-α RMSD as a function of simulation time for the final ligand selection of LC (replicas 1–3) and RMT-C-Epro (replicas 1–3) corresponding to **A**–**F**, respectively [169].



Supplementary Figure 8: Protein's radius of gyration as a function of simulation time for the final ligand selection. Labels are the same as in Supplementary Figure 7 [169].



Supplementary Figure 9: Number of hydrogen bonds formed between the protein and the ligand as a function of simulation time for the final ligand selection. Labels are the same as in Supplementary Figure 7 [169].



Supplementary Figure 10: Total MM-PBSA per-residue binding free energy contributions for the final ligand selection. Labels are the same as in Supplementary Figure 7 [169].

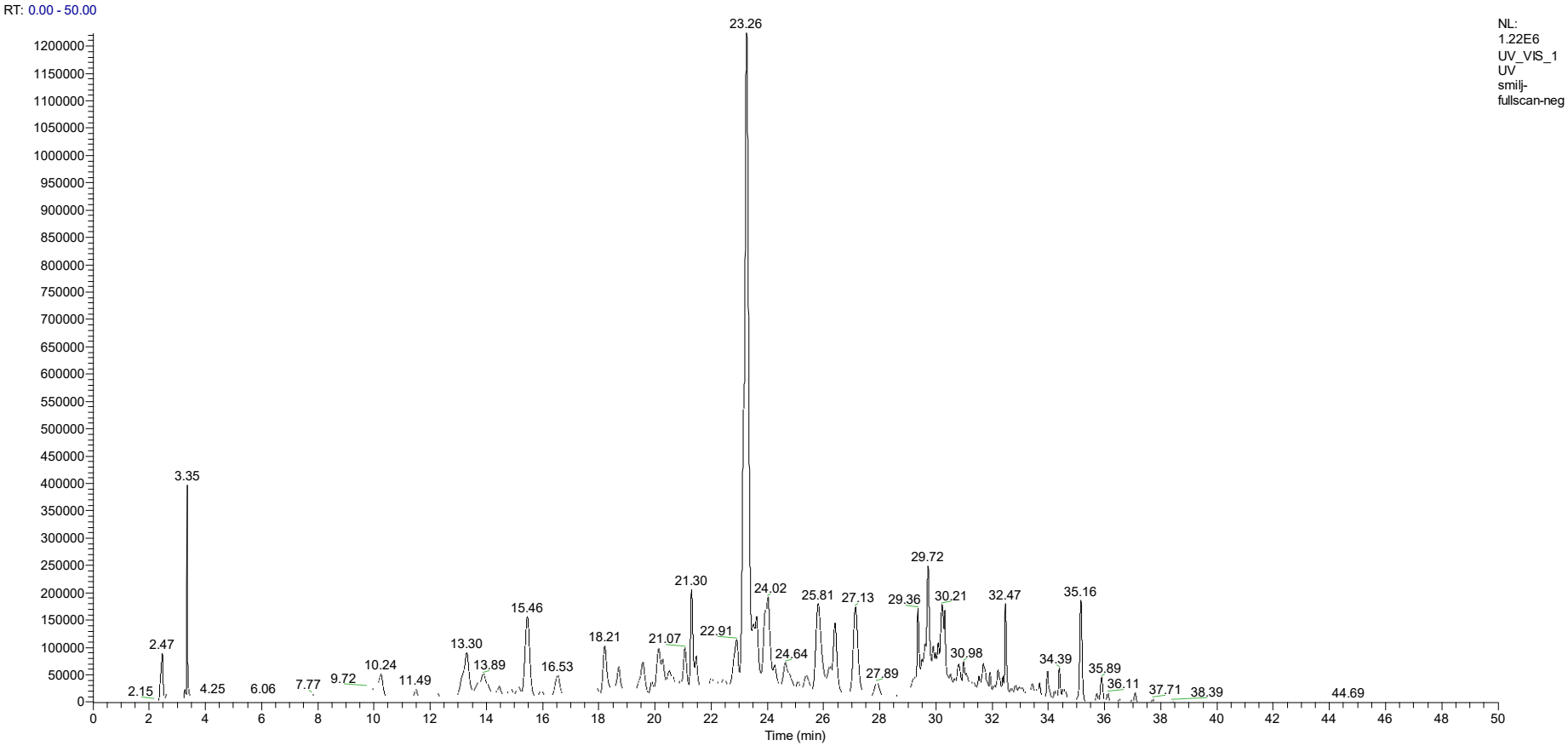
Supplementary Table 3: MM-PBSA binding free energies of individual protein residues, ΔG^{res}_{bind}, for which ΔG^{res}_{bind} <-1.80 kcal/mol. SARS-CoV-2 Epro subunit labels are shown in Supplementary Figure 5 [169].

Compound	Residue	ΔG^{res}_{bind}[kcal/mol]
LC N-terminal Replica 1	B:GLU:8	-1.9 ± 0.8
LC N-terminal Replica 2	C:GLU:8	-12.7 ± 0.7
LC N-terminal Replica 3	A:ASN:15 B:ASN:15 B:LEU:18	-5.7 ± 0.3 -2.5 ± 0.3 2.2 ± 0.2
RMT C-terminal Replica 1	-	-
RMT C-terminal Replica 2	-	-
RMT C-terminal Replica 3	-	-

A.4 Supplementary Material for Section 3.2.3.4

Supplementary Table 4: Tentative identification of phenolic compounds in ethanolic extract of *Helichrysum italicum* by MS/MS. Rt = retention time; $[M\text{-}H]^-$ = main mass of substance in negative ion mode; MS^2 = first fragmentation; MS^3 = second fragmentation; MS^4 = third fragmentation

Number	Compound name	Rt (min)	$[M-H]^-$ (m/z)	MS^2 (m/z)	MS^3 (m/z)	MS^4 (m/z)
1	3-caffeoylquinic acid (neochlorogenic acid)	7.77	353	191 (100), 179 (7)		
2	5-caffeoylquinic acid (chlorogenic acid)	9.72	353	191 (100), 179 (47), 135 (7)		
3	3-caffeoylquinic acid derivative 1	10.01	451	**353 (100)**	191 (100), 179 (46), 161 (30), 135 (6)	
4	3-caffeoylquinic acid derivative 2	10.24	451	**353 (100)**	191 (100), 179 (46), 161 (29), 135 (7)	
5	4-caffeoylquinic acid	13.30	353	173 (100), 179 (55), 191 (19), 135 (4)		
6	3-caffeoylquinic acid isomer	13.89	353	191 (100), 179 (8)		
7	caffeoyl hexaric acid	14.46	371	191 (100), 173 (20)		
8	5-caffeoylquinic acid isomer	15.46	353	191 (100), 179 (4), 135 (3)		
9	dicaffeoyl hexaric acid 1	16.53	533	**353 (100)**	191 (100), 179 (45), 173 (14), 135 (7)	
10	dicaffeoyl hexaric acid 2	18.21	533	**353 (100)**, 371 (76), 515 (30)	191 (100), 179 (49), 173 (14), 135 (7)	
11	myricetin 3-*O*-glucoside	18.65	479	317 (100), 316 (20)		
12	isorhamnetin 3-*O*-glucoside	20.13	477	315 (100)		
13	1, 3-dicaffeoylquinic acid-hexoside	20.40	677	**515 (100)**, 353 (16)	**353 (100)**, 323 (29)	179 (100), 191 (90), 173 (19)
14	quercetin-3-*O*-glucoside	21.30	463	301 (100)		
15	1, 3-dicaffeoylquinic acid derivative 1	22.91	724	**515 (100)**, 353 (40)	**353 (100)**	191 (100), 179 (25), 173 (20), 135 (4)
16	1, 3-dicaffeoylquinic acid	23.42	515	**353 (100)**	191 (100), 179 (28), 173 (25), 135 (3)	
17	1, 3-dicaffeoylquinic acid	23.68	515	**353 (100)**	191 (100), 179 (51), 173 (22), 135 (7)	
18	3,4-dicaffeoylquinic acid	24.02	515	**353 (100)**	173 (100), 191 (64), 179 (62), 135 (3)	
19	1,3-dicaffeoylquinic acid malonyl	24.64	601	**557 (100)**, 395 (57)	**395 (100)**	191 (100), 173 (40), 179 (30)
20	tricaffeoylhexaric acid 1	25.81	695	533 (100), 371 (39)	371 (100), 209 (5), 353 (5)	
21	quercetin-*O*-coumaroylglucoside 1	26.41	609	463 (100), 301 (10)	301 (100)	



Supplementary Figure 11: Representative HPLC-MS chromatogram of the ethanolic extract of *Helichrysum italicum* recorded in negative ion mode. Peaks correspond to phenolic compounds identified by MS^n fragmentation (Supplementary Table 4).

References

[1] F. S. Cohen, 'How Viruses Invade Cells', *Biophys J*, vol. 110, no. 5, pp. 1028–1032, Mar. 2016, doi: 10.1016/j.bpj.2016.02.006.

[2] W.-S. Ryu, *Molecular Virology of Human Pathogenic Viruses*, vol. 2017.

[3] B. Marintcheva, 'Introduction to Viral Structure, Diversity and Biology', in *Harnessing the Power of Viruses*, Elsevier, 2018, pp. 1–26. doi: 10.1016/B978-0-12-810514-6.00001-5.

[4] K. Wisskirchen, J. Lucifora, T. Michler, and U. Protzer, 'New pharmacological strategies to fight enveloped viruses', *Trends in Pharmacological Sciences*, vol. 35, no. 9, pp. 470–478, Sep. 2014, doi: 10.1016/j.tips.2014.06.004.

[5] L. Liang, A. Ahamed, L. Ge, X. Fu, and G. Lisak, 'Advances in Antiviral Material Development', *ChemPlusChem*, vol. 85, no. 9, pp. 2105–2128, Sep. 2020, doi: 10.1002/cplu.202000460.

[6] J. L. Geoghegan, A. M. Senior, F. Di Giallonardo, and E. C. Holmes, 'Virological factors that increase the transmissibility of emerging human viruses', *Proc. Natl. Acad. Sci. U.S.A.*, vol. 113, no. 15, pp. 4170–4175, Apr. 2016, doi: 10.1073/pnas.1521582113.

[7] K. R. Wigginton and A. B. Boehm, 'Environmental Engineers and Scientists Have Important Roles to Play in Stemming Outbreaks and Pandemics Caused by Enveloped Viruses', *Environ. Sci. Technol.*, vol. 54, no. 7, pp. 3736–3739, Apr. 2020, doi: 10.1021/acs.est.0c01476.

[8] Y. Mahmoud, A. Hathout, R. A. Amen, S. Desouky, R. M. Shady, and H. M. Fahmy, 'COVID-19 omicron variant: variation from other variants, immune response, and vaccination against this rapidly spreading pandemic', *Reviews and Research in Medical Microbiology*, vol. 36, no. 1, pp. 38–47, Jan. 2025, doi: 10.1097/MRM.0000000000000386.

[9] Z. Nie, T. Sun, and F. Zhao, 'Safety and Efficacy of Antiviral Drugs for the Treatment of COVID-19: A Systematic Review', *Infection and Drug Resistance*, vol. Volume 15, pp. 4457–4466, Aug. 2022, doi: 10.2147/IDR.S362946.

[10] B. Cao *et al.*, 'A Trial of Lopinavir–Ritonavir in Adults Hospitalized with Severe Covid-19', *New England Journal of Medicine*, vol. 382, no. 19, pp. 1787–1799, May 2020, doi: 10.1056/NEJMoa2001282.

[11] F. Kabinger *et al.*, 'Mechanism of molnupiravir-induced SARS-CoV-2 mutagenesis', *Nat Struct Mol Biol*, vol. 28, no. 9, pp. 740–746, Sep. 2021, doi: 10.1038/s41594-021-00651-0.

[12] S. Gandhi *et al.*, 'De novo emergence of a remdesivir resistance mutation during treatment of persistent SARS-CoV-2 infection in an immunocompromised patient: a case report', *Nat Commun*, vol. 13, no. 1, p. 1547, Mar. 2022, doi: 10.1038/s41467-022-29104-y.

[13] A. Heyer *et al.*, 'Remdesivir-induced emergence of SARS-CoV2 variants in patients with prolonged infection', *Cell Reports Medicine*, vol. 3, no. 9, p. 100735, Sep. 2022, doi: 10.1016/j.xcrm.2022.100735.

[14] H. Pan *et al.*, 'Remdesivir and three other drugs for hospitalised patients with COVID-19: final results of the WHO Solidarity randomised trial and updated meta-analyses', *The Lancet*, vol. 399, no. 10339, pp. 1941–1953, May 2022, doi: 10.1016/S0140-6736(22)00519-0.

[15] J. I. Hogan *et al.*, 'Remdesivir Resistance in Transplant Recipients With Persistent Coronavirus Disease 2019', *Clinical Infectious Diseases*, vol. 76, no. 2, pp. 342–345, Jan. 2023, doi: 10.1093/cid/ciac769.

[16] T. Sanderson *et al.*, 'A molnupiravir-associated mutational signature in global SARS-CoV-2 genomes', *Nature*, vol. 623, no. 7987, pp. 594–600, Nov. 2023, doi: 10.1038/s41586-023-06649-6.

[17] L. D. Saravolatz, S. Depcinski, and M. Sharma, 'Molnupiravir and Nirmatrelvir-Ritonavir: Oral Coronavirus Disease 2019 Antiviral Drugs', *Clinical Infectious Diseases*, vol. 76, no. 1, pp. 165–171, Jan. 2023, doi: 10.1093/cid/ciac180.

[18] N. R. Aggarwal *et al.*, 'Real-world use of nirmatrelvir–ritonavir in outpatients with COVID-19 during the era of omicron variants including BA.4 and BA.5 in Colorado, USA: a retrospective cohort study', *The Lancet Infectious Diseases*, vol. 23, no. 6, pp. 696–705, Jun. 2023, doi: 10.1016/S1473-3099(23)00011-7.

[19] Y. Duan *et al.*, 'Molecular mechanisms of SARS-CoV-2 resistance to nirmatrelvir', *Nature*, vol. 622, no. 7982, pp. 376–382, Oct. 2023, doi: 10.1038/s41586-023-06609-0.

[20] S. Zhou *et al.*, 'SARS-CoV-2 E protein: Pathogenesis and potential therapeutic development', *Biomedicine & Pharmacotherapy*, vol. 159, p. 114242, Mar. 2023, doi: 10.1016/j.biopha.2023.114242.

[21] U. Breitinger, C. A. Sedky, H. Sticht, and H.-G. Breitinger, 'Patch-clamp studies and cell viability assays suggest a distinct site for viroporin inhibitors on the E protein of SARS-CoV-2', *Virol J*, vol. 20, no. 1, p. 142, Jul. 2023, doi: 10.1186/s12985-023-02095-y.

[22] D. Kim, J.-Y. Lee, J.-S. Yang, J. W. Kim, V. N. Kim, and H. Chang, 'The Architecture of SARS-CoV-2 Transcriptome', *Cell*, vol. 181, no. 4, pp. 914-921.e10, May 2020, doi: 10.1016/j.cell.2020.04.011.

[23] S. Laha, J. Chakraborty, S. Das, S. K. Manna, S. Biswas, and R. Chatterjee, 'Characterizations of SARS-CoV-2 mutational profile, spike protein stability and viral transmission', *Infection, Genetics and Evolution*, vol. 85, p. 104445, Nov. 2020, doi: 10.1016/j.meegid.2020.104445.

[24] D. Chaudhuri, S. Majumder, J. Datta, and K. Giri, 'In Silico Study of Mutational Stability of SARS-CoV-2 Proteins', *Protein J*, vol. 40, no. 3, pp. 328–340, Jun. 2021, doi: 10.1007/s10930-021-09988-3.

[25] O. E. Omotoso, J. O. Olugbami, and M. A. Gbadegesin, 'Assessment of intercontinents mutation hotspots and conserved domains within SARS-CoV-2 genome', *Infection, Genetics and Evolution*, vol. 96, p. 105097, Dec. 2021, doi: 10.1016/j.meegid.2021.105097.

[26] V. S. Mandala, M. J. McKay, A. A. Shcherbakov, A. J. Dregni, A. Kolocouris, and M. Hong, 'Structure and drug binding of the SARS-CoV-2 envelope protein transmembrane domain in lipid bilayers', *Nat Struct Mol Biol*, vol. 27, no. 12, pp. 1202–1208, Dec. 2020, doi: 10.1038/s41594-020-00536-8.

[27] N. Kobe *et al.*, 'In silico determination of novel SARS-CoV-2 envelope protein ion channel inhibitors', *Computational and Structural Biotechnology Journal*, p. S2001037025002557, Jun. 2025, doi: 10.1016/j.csbj.2025.06.036.

[28] P. Venkatagopalan, S. M. Daskalova, L. A. Lopez, K. A. Dolezal, and B. G. Hogue, 'Coronavirus envelope (E) protein remains at the site of assembly', *Virology*, vol. 478, pp. 75–85, Apr. 2015, doi: 10.1016/j.virol.2015.02.005.

[29] D. Cabrera-Garcia, R. Bekdash, G. W. Abbott, M. Yazawa, and N. L. Harrison, 'The envelope protein of SARS-CoV-2 increases intra-Golgi pH and forms a cation channel that is regulated by pH', *The Journal of Physiology*, vol. 599, no. 11, pp. 2851–2868, Jun. 2021, doi: 10.1113/JP281037.

[30] L. Kuo and P. S. Masters, 'The Small Envelope Protein E Is Not Essential for Murine Coronavirus Replication', *J Virol*, vol. 77, no. 8, pp. 4597–4608, Apr. 2003, doi: 10.1128/JVI.77.8.4597-4608.2003.

[31] J. L. Nieto-Torres *et al.*, 'Subcellular location and topology of severe acute respiratory syndrome coronavirus envelope protein', *Virology*, vol. 415, no. 2, pp. 69–82, Jul. 2011, doi: 10.1016/j.virol.2011.03.029.

[32] M. J. B. Raamsman *et al.*, 'Characterization of the Coronavirus Mouse Hepatitis Virus Strain A59 Small Membrane Protein E', *J Virol*, vol. 74, no. 5, pp. 2333–2342, Mar. 2000, doi: 10.1128/JVI.74.5.2333-2342.2000.

[33] F. Fischer, C. F. Stegen, P. S. Masters, and W. A. Samsonoff, 'Analysis of Constructed E Gene Mutants of Mouse Hepatitis Virus Confirms a Pivotal Role for E Protein in Coronavirus Assembly', *J Virol*, vol. 72, no. 10, pp. 7885–7894, Oct. 1998, doi: 10.1128/JVI.72.10.7885-7894.1998.

[34] K. M. Curtis, B. Yount, and R. S. Baric, 'Heterologous Gene Expression from Transmissible Gastroenteritis Virus Replicon Particles', *J Virol*, vol. 76, no. 3, pp. 1422–1434, Feb. 2002, doi: 10.1128/JVI.76.3.1422-1434.2002.

[35] C. Castaño-Rodriguez *et al.*, 'Role of Severe Acute Respiratory Syndrome Coronavirus Viroporins E, 3a, and 8a in Replication and Pathogenesis', *mBio*, vol. 9, no. 3, pp. e02325-17, Jul. 2018, doi: 10.1128/mBio.02325-17.

[36] B. Xia *et al.*, 'SARS-CoV-2 envelope protein causes acute respiratory distress syndrome (ARDS)-like pathological damages and constitutes an antiviral target', *Cell Res*, vol. 31, no. 8, pp. 847–860, Aug. 2021, doi: 10.1038/s41422-021-00519-4.

[37] Y. Cao *et al.*, 'Characterization of the SARS-CoV-2 E Protein: Sequence, Structure, Viroporin, and Inhibitors', *Protein Science*, vol. 30, no. 6, pp. 1114–1130, Jun. 2021, doi: 10.1002/pro.4075.

[38] D. Blanco-Melo *et al.*, 'Imbalanced Host Response to SARS-CoV-2 Drives Development of COVID-19', *Cell*, vol. 181, no. 5, pp. 1036-1045.e9, May 2020, doi: 10.1016/j.cell.2020.04.026.

[39] L. Monarca *et al.*, 'Electrophysiological Impact of SARS-CoV-2 Envelope Protein in U251 Human Glioblastoma Cells: Possible Implications in Gliomagenesis?', *IJMS*, vol. 25, no. 12, p. 6669, Jun. 2024, doi: 10.3390/ijms25126669.

[40] J. K. Sethi and G. S. Hotamisligil, 'Metabolic Messengers: tumour necrosis factor', *Nat Metab*, vol. 3, no. 10, pp. 1302–1312, Oct. 2021, doi: 10.1038/s42255-021-00470-z.

[41] P. Feng *et al.*, 'Regulation of bitter taste responses by tumor necrosis factor', *Brain, Behavior, and Immunity*, vol. 49, pp. 32–42, Oct. 2015, doi: 10.1016/j.bbi.2015.04.001.

[42] C. Sala *et al.*, 'Stable expression of SARS-CoV-2 envelope viroporin promotes intracellular calcium depletion in human cells: relevance for endoplasmic reticulum stress, cell proliferation, pluripotency and lineage differentiation', *Cell Calcium*, vol. 128, p. 103032, Jun. 2025, doi: 10.1016/j.ceca.2025.103032.

[43] U. Breitinger, N. S. Farag, H. Sticht, and H.-G. Breitinger, 'Viroporins: Structure, function, and their role in the life cycle of SARS-CoV-2', *The International Journal of Biochemistry & Cell Biology*, vol. 145, p. 106185, Apr. 2022, doi: 10.1016/j.biocel.2022.106185.

[44] M. Ajel *et al.*, 'Investigation of the Mutations in the SARS-CoV-2 Envelope Protein and Its Interaction with the PALS1 by Molecular Docking', *rbmb.net*, vol. 13, no. 1, pp. 124–136, Apr. 2024, doi: 10.61186/rbmb.13.1.124.

[45] A. Asghari, M. Naseri, H. Safari, E. Saboory, and N. Parsamanesh, 'The Novel Insight of SARS-CoV-2 Molecular Biology and Pathogenesis and Therapeutic Options', *DNA and Cell Biology*, vol. 39, no. 10, pp. 1741–1753, Oct. 2020, doi: 10.1089/dna.2020.5703.

[46] K.-T. Teoh *et al.*, 'The SARS Coronavirus E Protein Interacts with PALS1 and Alters Tight Junction Formation and Epithelial Morphogenesis', *MBoC*, vol. 21, no. 22, pp. 3838–3852, Nov. 2010, doi: 10.1091/mbc.e10-04-0338.

[47] D. R. Hout *et al.*, 'Substitution of the transmembrane domain of Vpu in simian–human immunodeficiency virus (SHIVKU1bMC33) with that of M2 of influenza A results in a virus that is sensitive to inhibitors of the M2 ion channel and is pathogenic for pig-tailed macaques', *Virology*, vol. 344, no. 2, pp. 541–559, Jan. 2006, doi: 10.1016/j.virol.2005.08.022.

[48] D. R. Hout *et al.*, 'Scrambling of the amino acids within the transmembrane domain of Vpu results in a simian-human immunodeficiency virus (SHIVTM) that is less pathogenic for pig-tailed macaques', *Virology*, vol. 339, no. 1, pp. 56–69, Aug. 2005, doi: 10.1016/j.virol.2005.04.038.

[49] M. Takeda, A. Pekosz, K. Shuck, L. H. Pinto, and R. A. Lamb, 'Influenza A Virus M_2 Ion Channel Activity Is Essential for Efficient Replication in Tissue Culture', *J Virol*, vol. 76, no. 3, pp. 1391–1399, Feb. 2002, doi: 10.1128/JVI.76.3.1391-1399.2002.

[50] T. Sakaguchi, G. P. Leser, and R. A. Lamb, 'The ion channel activity of the influenza virus M2 protein affects transport through the Golgi apparatus.', *The Journal of cell biology*, vol. 133, no. 4, pp. 733–747, May 1996, doi: 10.1083/jcb.133.4.733.

[51] D. Dey, S. Borkotoky, and M. Banerjee, 'In silico identification of Tretinoin as a SARS-CoV-2 envelope (E) protein ion channel inhibitor', *Computers in Biology and Medicine*, vol. 127, p. 104063, Dec. 2020, doi: 10.1016/j.compbiomed.2020.104063.

[52] Y. Wang *et al.*, 'Discovery of SARS-CoV-2-E channel inhibitors as antiviral candidates', *Acta Pharmacol Sin*, vol. 43, no. 4, pp. 781–787, Apr. 2022, doi: 10.1038/s41401-021-00732-2.

[53] G. D. Ewart, K. Mills, G. B. Cox, and P. W. Gage, 'Amiloride derivatives block ion channel activity and enhancement of virus-like particle budding caused by HIV-1 protein Vpu', *Eur Biophys J*, vol. 31, no. 1, pp. 26–35, Mar. 2002, doi: 10.1007/s002490100177.

[54] P. H. Jalily *et al.*, 'Mechanisms of Action of Novel Influenza A/M2 Viroporin Inhibitors Derived from Hexamethylene Amiloride', *Molecular Pharmacology*, vol. 90, no. 2, pp. 80–95, Aug. 2016, doi: 10.1124/mol.115.102731.

[55] L. Wilson, P. Gage, and G. Ewart, 'Hexamethylene amiloride blocks E protein ion channels and inhibits coronavirus replication', *Virology*, vol. 353, no. 2, pp. 294–306, Sep. 2006, doi: 10.1016/j.virol.2006.05.028.

[56] A. Premkumar, L. Wilson, G. D. Ewart, and P. W. Gage, 'Cation-selective ion channels formed by p7 of hepatitis C virus are blocked by hexamethylene amiloride', *FEBS Letters*, vol. 557, no. 1–3, pp. 99–103, Jan. 2004, doi: 10.1016/S0014-5793(03)01453-4.

[57] V. M. Deyde *et al.*, 'Surveillance of Resistance to Adamantanes among Influenza A(H3N2) and A(H1N1) Viruses Isolated Worldwide', *J INFECT DIS*, vol. 196, no. 2, pp. 249–257, Jul. 2007, doi: 10.1086/518936.

[58] P. Intharathep *et al.*, 'How amantadine and rimantadine inhibit proton transport in the M2 protein channel', *Journal of Molecular Graphics and Modelling*, vol. 27, no. 3, pp. 342–348, Oct. 2008, doi: 10.1016/j.jmgm.2008.06.002.

[59] U. Breitinger, N. K. M. Ali, H. Sticht, and H.-G. Breitinger, 'Inhibition of SARS CoV Envelope Protein by Flavonoids and Classical Viroporin Inhibitors', *Front. Microbiol.*, vol. 12, p. 692423, Jul. 2021, doi: 10.3389/fmicb.2021.692423.

[60] S. Yousefbeigi and F. Marsusi, 'Advanced Computational Approaches to Evaluate the Potential of New-Generation Adamantane-Based Drugs as Viroporin Inhibitors: A Case Study on SARS-CoV-2', *J. Phys. Chem. B*, vol. 129, no. 32, pp. 8127–8143, Aug. 2025, doi: 10.1021/acs.jpcb.5c02898.

[61] Y. Zhou *et al.*, 'Efficacy of Ion-Channel Inhibitors Amantadine, Memantine and Rimantadine for the Treatment of SARS-CoV-2 In Vitro', *Viruses*, vol. 13, no. 10, p. 2082, Oct. 2021, doi: 10.3390/v13102082.

[62] S. P. Smieszek, B. P. Przychodzen, and M. H. Polymeropoulos, 'Amantadine disrupts lysosomal gene expression: A hypothesis for COVID19 treatment', *International Journal of Antimicrobial Agents*, vol. 55, no. 6, p. 106004, Jun. 2020, doi: 10.1016/j.ijantimicag.2020.106004.

[63] M. G. Jeppesen, T. L. Toft-Bertelsen, T. N. Kledal, and M. M. Rosenkilde, 'Amantadin has potential for the treatment of COVID-19 because it targets known and novel ion channels encoded by SARS-CoV-2', Dec. 15, 2020, *Research Square*. doi: 10.21203/rs.3.rs-121743/v1.

[64] K. Fink, A. Nitsche, M. Neumann, M. Grossegesse, K.-H. Eisele, and W. Danysz, 'Amantadine Inhibits SARS-CoV-2 In Vitro', *Viruses*, vol. 13, no. 4, Mar. 2021, doi: 10.3390/v13040539.

[65] T. L. Toft-Bertelsen *et al.*, 'Amantadine inhibits known and novel ion channels encoded by SARS-CoV-2 in vitro', *Commun Biol*, vol. 4, no. 1, p. 1347, Dec. 2021, doi: 10.1038/s42003-021-02866-9.

[66] P. P. Singh Tomar and I. T. Arkin, 'SARS-CoV-2 E protein is a potential ion channel that can be inhibited by Gliclazide and Memantine', *Biochemical and Biophysical Research Communications*, vol. 530, no. 1, pp. 10–14, Sep. 2020, doi: 10.1016/j.bbrc.2020.05.206.

[67] S. Hasanagic and F. Serdarevic, 'Potential role of memantine in the prevention and treatment of COVID-19: its antagonism of nicotinic acetylcholine receptors and beyond', *Eur Respir J*, vol. 56, no. 2, p. 2001610, Aug. 2020, doi: 10.1183/13993003.01610-2020.

[68] S. H. Park *et al.*, 'Interactions of SARS-CoV-2 envelope protein with amilorides correlate with antiviral activity', *PLoS Pathog*, vol. 17, no. 5, p. e1009519, May 2021, doi: 10.1371/journal.ppat.1009519.

[69] Md. O. Rafi *et al.*, 'Combination of QSAR, molecular docking, molecular dynamic simulation and MM-PBSA: analogues of lopinavir and favipiravir as potential drug candidates against COVID-19', *Journal of Biomolecular Structure and Dynamics*, vol. 40, no. 8, pp. 3711–3730, May 2022, doi: 10.1080/07391102.2020.1850355.

[70] A. Sharma, J. Vora, D. Patel, S. Sinha, P. C. Jha, and N. Shrivastava, 'Identification of natural inhibitors against prime targets of SARS-CoV-2 using molecular docking, molecular dynamics simulation and MM-PBSA approaches', *Journal of Biomolecular Structure and Dynamics*, vol. 40, no. 7, pp. 3296–3311, May 2022, doi: 10.1080/07391102.2020.1846624.

[71] P. P. Kushwaha *et al.*, 'Identification of Natural Inhibitors Against SARS-CoV-2 Drugable Targets Using Molecular Docking, Molecular Dynamics Simulation, and MM-PBSA Approach', *Front. Cell. Infect. Microbiol.*, vol. 11, Aug. 2021, doi: 10.3389/fcimb.2021.730288.

[72] A. Hospital, J. R. Goñi, M. Orozco, and J. L. Gelpí, 'Molecular dynamics simulations: advances and applications', *Advances and Applications in Bioinformatics and Chemistry*, vol. 8, pp. 37–47, Nov. 2015, doi: 10.2147/AABC.S70333.

[73] D. Brahim Belhaouari *et al.*, 'The Strengths of Scanning Electron Microscopy in Deciphering SARS-CoV-2 Infectious Cycle', *Front. Microbiol.*, vol. 11, Aug. 2020, doi: 10.3389/fmicb.2020.02014.

[74] C. Aoki-Utsubo, M. Chen, and H. Hotta, 'Time-of-addition and Temperature-shift Assays to Determine Particular Step(s) in the Viral Life Cycle that is Blocked by Antiviral Substance(s)', *BIO-PROTOCOL*, vol. 8, no. 9, p. e2830, 2018, doi: 10.21769/BioProtoc.2830.

[75] S. Zangooie, R. Ghanbari, F. A. Jalilian, S. Mahmoudvand, and A. Teimoori, 'Antiviral potential of phenolic compounds against HSV-1: In-vitro study', *Antiviral Therapy*, vol. 29, no. 5, p. 13596535241271589, Oct. 2024, doi: 10.1177/13596535241271589.

[76] S.-Y. Lyu, J.-Y. Rhim, and W.-B. Park, 'Antiherpetic activities of flavonoids against herpes simplex virus type 1 (HSV-1) and type 2 (HSV-2)in vitro', *Arch Pharm Res*, vol. 28, no. 11, pp. 1293–1301, Nov. 2005, doi: 10.1007/BF02978215.

[77] S. Lee, H. H. Lee, Y. S. Shin, H. Kang, and H. Cho, 'The anti-HSV-1 effect of quercetin is dependent on the suppression of TLR-3 in Raw 264.7 cells', *Arch. Pharm. Res.*, vol. 40, no. 5, pp. 623–630, May 2017, doi: 10.1007/s12272-017-0898-x.

[78] F. Carmona and A. M. Soares Pereira, 'Herbal medicines: Old and new concepts, truths and misunderstandings', *Revista Brasileira de Farmacognosia*, vol. 23, no. 2, pp. 379–385, Mar. 2013, doi: 10.1590/S0102-695X2013005000018.

[79] J. Rahul and M. Stavroula, 'Mediterranean climate affects the biosynthesis of secondary metabolites in common medicinal plants', vol. 2016, Accessed: Mar. 12, 2026. [Online]. Available: https://www.academia.edu/29203508/MEDITERRANEAN_CLIMATE_AFFECTS_THE_BIOSYNTHESIS_OF_SECONDARY_METABOLITES_IN_COMMON_MEDICINAL_PLANTS

[80] D. Antunes Viegas, A. Palmeira-de-Oliveira, L. Salgueiro, J. Martinez-de-Oliveira, and R. Palmeira-de-Oliveira, 'Helichrysum italicum: From traditional use to scientific data', *Journal of Ethnopharmacology*, vol. 151, no. 1, pp. 54–65, Jan. 2014, doi: 10.1016/j.jep.2013.11.005.

[81] S. N. Jimenez-Garcia, M. A. Vazquez-Cruz, R. Guevara-González, I. Torres-Pacheco, A. Cruz-Hernandez, and A. A. Feregrino-Perez, 'Current Approaches for Enhanced Expression of Secondary Metabolites as Bioactive Compounds in Plants for Agronomic and Human Health Purposes', *Pol. J. Food Nutr. Sci.*, vol. 63, no. 2, pp. 67–78, Jun. 2013, doi: 10.2478/v10222-012-0072-6.

[82] A. Giovanni Battista, F. Pollastro, A. Minassi, M. Andrea, and M. Ballero, 'Helichrysum italicum: Sleeping giant of the mediterranean herbal medicine', *Herbalgram*, vol. 105, pp. 36–47, Jan. 2015.

[83] T. Ninčević, M. Grdiša, Z. Šatović, and M. Jug-Dujaković, 'Helichrysum italicum (Roth) G. Don: Taxonomy, biological activity, biochemical and genetic diversity', *Industrial Crops and Products*, vol. 138, p. 111487, Oct. 2019, doi: 10.1016/j.indcrop.2019.111487.

[84] D. Bandelj, M. Hladnik, K. Kramberger, and A. Baruca Arbeiter, *Spoznajmo laški smilj*. Založba Univerze na Primorskem, 2020. doi: 10.26493/978-961-293-005-9.

[85] M. Galbany-Casals, L. Sáez, and C. Benedí, 'A taxonomic revision of Helichrysum sect. Stoechadina (Asteraceae, Gnaphalieae)', *Can. J. Bot.*, vol. 84, no. 8, pp. 1203–1232, Aug. 2006, doi: 10.1139/b06-082.

[86] E. Guinoiseau *et al.*, 'Biological properties and resistance reversal effect of Helichrysum italicum (Roth) G. Don', 2013, pp. 1073–1080.

[87] S. Herrando-Moraira, J. M. Blanco-Moreno, L. Sáez, and M. Galbany-Casals, 'Reevaluación del complejo Helichrysum italicum (Compositae: Gnaphalieae): una nueva especie en Mallorca (Islas Baleares)', *Collect. Bot.*, vol. 35, p. e009, Dec. 2016, doi: 10.3989/collectbot.2016.v35.009.

[88] R. Maffei Facino, M. Carini, M. Mariani, and C. Cipriani, 'Anti-erythematous and photoprotective activities in guinea pigs and man of topically applied flavonoids from Helichrysum italicum G. Don', 1988, Accessed: Dec. 26, 2025. [Online]. Available: https://air.unimi.it/handle/2434/184783

[89] R. M. Facino, M. Carini, L. Franzoi, O. Pirola, and E. Bosisio, 'Phytochemical characterization and radical scavenger activity of flavonoids from *Helichrysum italicum* G. Don (compositae)', *Pharmacological Research*, vol. 22, no. 6, pp. 709–721, Nov. 1990, doi: 10.1016/S1043-6618(05)80097-0.

[90] E. Guinoiseau *et al.*, 'Biological properties and resistance reversal effect of Helichrysum italicum (Roth) G. Don', 2013, pp. 1073–1080.

[91] J. Sendker and H. Sheridan, 'Composition and Quality Control of Herbal Medicines', in *Toxicology of Herbal Products*, O. Pelkonen, P. Duez, P. M. Vuorela, and H. Vuorela, Eds, Cham: Springer International Publishing, 2017, pp. 29–65. doi: 10.1007/978-3-319-43806-1_3.

[92] S. Maksimovic, V. Tadic, D. Skala, and I. Zizovic, 'Separation of phytochemicals from *Helichrysum italicum*: An analysis of different isolation techniques and biological activity of prepared extracts', *Phytochemistry*, vol. 138, pp. 9–28, Jun. 2017, doi: 10.1016/j.phytochem.2017.01.001.

[93] C. Manach, A. Scalbert, C. Morand, C. Rémésy, and L. Jiménez, 'Polyphenols: food sources and bioavailability', *The American Journal of Clinical Nutrition*, vol. 79, no. 5, pp. 727–747, May 2004, doi: 10.1093/ajcn/79.5.727.

[94] G. Appendino *et al.*, 'Arzanol, an Anti-inflammatory and Anti-HIV-1 Phloroglucinol α-Pyrone from Helichrysum italicum ssp. microphyllum', *J. Nat. Prod.*, vol. 70, no. 4, pp. 608–612, Apr. 2007, doi: 10.1021/np060581r.

[95] K. Kramberger, S. Kenig, Z. Jenko Pražnikar, N. Kočevar Glavač, and D. Barlič-Maganja, 'A Review and Evaluation of the Data Supporting Internal Use of Helichrysum italicum', *Plants*, vol. 10, no. 8, p. 1738, Aug. 2021, doi: 10.3390/plants10081738.

[96] D. J. Charles and J. E. Simon, 'Volatile Compounds of the Curry Plant', *HortSci*, vol. 26, no. 1, pp. 69–70, Jan. 1991, doi: 10.21273/HORTSCI.26.1.69.

[97] S. Andreani, A. Uehara, P. Blagojević, N. Radulović, A. Muselli, and N. Baldovini, 'Key odorants of industrially-produced Helichrysum italicum subsp. italicum essential oil', *Industrial Crops and Products*, vol. 132, pp. 275–282, Jun. 2019, doi: 10.1016/j.indcrop.2019.02.008.

[98] C. G. Pereira *et al.*, 'Chemical profiling of infusions and decoctions of Helichrysum italicum subsp. picardii by UHPLC-PDA-MS and in vitro biological activities comparatively with green tea (Camellia sinensis) and rooibos tisane (Aspalathus linearis)', *Journal of Pharmaceutical and Biomedical Analysis*, vol. 145, pp. 593–603, Oct. 2017, doi: 10.1016/j.jpba.2017.07.007.

[99] K. Kramberger *et al.*, 'HPLC-DAD-ESI-QTOF-MS Determination of Bioactive Compounds and Antioxidant Activity Comparison of the Hydroalcoholic and Water Extracts from Two Helichrysum italicum Species', *Metabolites*, vol. 10, no. 10, p. 403, Oct. 2020, doi: 10.3390/metabo10100403.

[100] G. G. Zapesochnaya, T. V. Dzyadevich, and B. S. Karasartov, 'Phenolic compounds of Helichrysum italicum', *Chem Nat Compd*, vol. 26, no. 3, pp. 342–343, May 1990, doi: 10.1007/BF00597869.

[101] G. G. Zapesochnaya *et al.*, 'Dicaffeolyquinic acids from Helichrysum italicum and Achillea cartilaginea', *Chem Nat Compd*, vol. 28, no. 1, pp. 40–44, 1992, doi: 10.1007/BF00629790.

[102] A. Sala *et al.*, 'Anti-inflammatory and antioxidant properties of *Helichrysum italicum*', *Journal of Pharmacy and Pharmacology*, vol. 54, no. 3, pp. 365–371, Mar. 2002, doi: 10.1211/0022357021778600.

[103] A. Sala *et al.*, 'Assessment of the anti-inflammatory activity and free radical scavenger activity of tiliroside', *European Journal of Pharmacology*, vol. 461, no. 1, pp. 53–61, Feb. 2003, doi: 10.1016/S0014-2999(02)02953-9.

[104] A. L. De La Garza *et al.*, 'Helichrysum and Grapefruit Extracts Inhibit Carbohydrate Digestion and Absorption, Improving Postprandial Glucose Levels and Hyperinsulinemia in Rats', *J. Agric. Food Chem.*, vol. 61, no. 49, pp. 12012–12019, Dec. 2013, doi: 10.1021/jf4021569.

[105] A. Mari, A. Napolitano, M. Masullo, C. Pizza, and S. Piacente, 'Identification and quantitative determination of the polar constituents in Helichrysum italicum flowers and derived food supplements', *Journal of Pharmaceutical and Biomedical Analysis*, vol. 96, pp. 249–255, Aug. 2014, doi: 10.1016/j.jpba.2014.04.005.

[106] A. Rosa *et al.*, 'Evaluation of the antioxidant and cytotoxic activity of arzanol, a prenylated α-pyrone–phloroglucinol etherodimer from Helichrysum italicum subsp.microphyllum', *Chemico-Biological Interactions*, vol. 165, no. 2, pp. 117–126, Jan. 2007, doi: 10.1016/j.cbi.2006.11.006.

[107] O. Taglialatela-Scafati *et al.*, 'Antimicrobial Phenolics and Unusual Glycerides from *Helichrysum italicum* subsp. *microphyllum*', *J. Nat. Prod.*, vol. 76, no. 3, pp. 346–353, Mar. 2013, doi: 10.1021/np3007149.

[108] M. Galbany-Casals, J. M. Blanco-Moreno, N. Garcia-Jacas, I. Breitwieser, and R. D. Smissen, 'Genetic variation in Mediterranean Helichrysum italicum (Asteraceae; Gnaphalieae): do disjunct populations of subsp. microphyllum have a common origin?', *Plant Biology*, vol. 13, no. 4, pp. 678–687, 2011, doi: 10.1111/j.1438-8677.2010.00411.x.

[109] A. Nostro *et al.*, 'Evaluation of antiherpesvirus-1 and genotoxic activities of Helichrysum italicum extract', *New Microbiol*, vol. 26, no. 1, pp. 125–128, Jan. 2003.

[110] A. M. Dzamic, K. S. Mileski, A. D. Ciric, M. S. Ristic, M. D. Sokovic, and P. D. Marin, 'Essential Oil Composition, Antioxidant and Antimicrobial Properties of Essential Oil and Deodorized Extracts of *Helichrysum italicum* (Roth) G. Don', *Journal of Essential Oil Bearing Plants*, vol. 22, no. 2, pp. 493–503, Mar. 2019, doi: 10.1080/0972060X.2019.1611487.

[111] M. Kazazic, 'Antioxidant activity of water extracts of some medicinal plants from Herzegovina region', *Int. J. Pure App. Biosci.*, vol. 4, no. 2, pp. 85–90, Apr. 2016, doi: 10.18782/2320-7051.2251.

[112] A. Rosa *et al.*, 'Protective role of arzanol against lipid peroxidation in biological systems', *Chemistry and Physics of Lipids*, vol. 164, no. 1, pp. 24–32, Jan. 2011, doi: 10.1016/j.chemphyslip.2010.09.009.

[113] J. Bauer *et al.*, 'Arzanol, a prenylated heterodimeric phloroglucinyl pyrone, inhibits eicosanoid biosynthesis and exhibits anti-inflammatory efficacy in vivo', *Biochemical Pharmacology*, vol. 81, no. 2, pp. 259–268, Jan. 2011, doi: 10.1016/j.bcp.2010.09.025.

[114] P. S. Kothavade, D. M. Nagmoti, V. D. Bulani, and A. R. Juvekar, 'Arzanol, a Potent mPGES-1 Inhibitor: Novel Anti-Inflammatory Agent', *The Scientific World Journal*, vol. 2013, no. 1, p. 986429, Jan. 2013, doi: 10.1155/2013/986429.

[115] J.-I. Lee and G. J. Burckart, 'Nuclear Factor Kappa B: Important Transcription Factor and Therapeutic Target', *The Journal of Clinical Pharmacology*, vol. 38, no. 11, pp. 981–993, 1998, doi: 10.1177/009127009803801101.

[116] D. Bojilov *et al.*, 'HPLC Analysis and In Vitro and In Silico Evaluation of the Biological Activity of Polyphenolic Components Separated with Solvents of Various Polarities from Helichrysum italicum', *Molecules*, vol. 28, no. 17, p. 6198, Aug. 2023, doi: 10.3390/molecules28176198.

[117] B. T. T. Luyen *et al.*, 'Anti-inflammatory components of Chrysanthemum indicum flowers', *Bioorganic & Medicinal Chemistry Letters*, vol. 25, no. 2, pp. 266–269, Jan. 2015, doi: 10.1016/j.bmcl.2014.11.054.

[118] U. Huss, T. Ringbom, P. Perera, L. Bohlin, and M. Vasänge, 'Screening of Ubiquitous Plant Constituents for COX-2 Inhibition with a Scintillation Proximity Based Assay', *J. Nat. Prod.*, vol. 65, no. 11, pp. 1517–1521, Nov. 2002, doi: 10.1021/np020023m.

[119] P. Cebollada, N. G. M. Gomes, P. B. Andrade, and V. López, 'An integrated in vitro approach on the enzymatic and antioxidant mechanisms of four commercially available essential oils (Copaifera officinalis, Gaultheria fragrantissima, Helichrysum italicum, and Syzygium aromaticum) traditionally used topically for their anti-inflammatory effects', *Front. Pharmacol.*, vol. 14, p. 1310439, Jan. 2024, doi: 10.3389/fphar.2023.1310439.

[120] M. C. Souza, A. C. Siani, M. F. S. Ramos, O. J. Menezes-de-Lima, and M. G. M. O. Henriques, 'Evaluation of anti-inflammatory activity of essential oils from two Asteraceae species', *Pharmazie*, vol. 58, no. 8, pp. 582–586, Aug. 2003.

[121] A. T. Rufino *et al.*, 'Anti-inflammatory and Chondroprotective Activity of (+)-α-Pinene: Structural and Enantiomeric Selectivity', *J. Nat. Prod.*, vol. 77, no. 2, pp. 264–269, Feb. 2014, doi: 10.1021/np400828x.

[122] J. Mastelic, O. Politeo, I. Jerkovic, and N. Radosevic, 'Composition and Antimicrobial Activity of Helichrysum italicum Essential Oil and Its Terpene and

Terpenoid Fractions', *Chem Nat Compd*, vol. 41, no. 1, pp. 35–40, Jan. 2005, doi: 10.1007/s10600-005-0069-z.

[123] I. Chinou, V. Roussis, D. Perdetzoglou, and A. Loukis, 'Chemical and Biological Studies on Two *Helichrysum* Species of Greek Origin', *Planta Med*, vol. 62, no. 04, pp. 377–379, Aug. 1996, doi: 10.1055/s-2006-957914.

[124] P.-G. Rossi *et al.*, 'Antibacterial Action of Essential Oils from Corsica', *Journal of Essential Oil Research*, vol. 19, no. 2, pp. 176–182, Mar. 2007, doi: 10.1080/10412905.2007.9699254.

[125] H. Cui, C. Zhao, and L. Lin, 'Antibacterial Activity of *H elichrysum italicum* Oil on Vegetables and Its Mechanism of Action: *Helichrysum Italicum* Oil Antibacterial Activity', *Journal of Food Processing and Preservation*, vol. 39, no. 6, pp. 2663–2672, Dec. 2015, doi: 10.1111/jfpp.12516.

[126] V. Lorenzi *et al.*, 'Geraniol Restores Antibiotic Activities against Multidrug-Resistant Isolates from Gram-Negative Species', *Antimicrob Agents Chemother*, vol. 53, no. 5, pp. 2209–2211, May 2009, doi: 10.1128/AAC.00919-08.

[127] B. Djihane, N. Wafa, S. Elkhamssa, D. H. J. Pedro, A. E. Maria, and Z. Mohamed Mihoub, 'Chemical constituents of Helichrysum italicum (Roth) G. Don essential oil and their antimicrobial activity against Gram-positive and Gram-negative bacteria, filamentous fungi and Candida albicans', *Saudi Pharmaceutical Journal*, vol. 25, no. 5, pp. 780–787, Jul. 2017, doi: 10.1016/j.jsps.2016.11.001.

[128] A. Nostro, G. Bisignano, M. Angela Cannatelli, G. Crisafi, M. Paola Germanò, and V. Alonzo, 'Effects of *Helichrysum italicum* extract on growth and enzymatic activity of *Staphylococcus aureus*', *International Journal of Antimicrobial Agents*, vol. 17, no. 6, pp. 517–520, Jun. 2001, doi: 10.1016/S0924-8579(01)00336-3.

[129] A. Nostro, M. A. Cannatelli, G. Crisafi, A. D. Musolino, F. Procopio, and V. Alonzo, 'Modifications of hydrophobicity, in vitro adherence and cellular aggregation of Streptococcus mutans by Helichrysum italicum extract', *Lett. Appl. Microbiol.*, vol. 38, no. 5, pp. 423–427, May 2004, doi: 10.1111/j.1472-765X.2004.01509.x.

[130] R. Tundis *et al.*, 'Influence of environmental factors on composition of volatile constituents and biological activity of *Helichrysum italicum* (Roth) Don (Asteraceae)', *Natural Product Research*, vol. 19, no. 4, pp. 379–387, Jun. 2005, doi: 10.1080/14786410420002619 69.

[131] F. Tomás-Barberán, E. Iniesta-Sanmartín, F. Tomás-Lorente, and A. Rumbero, 'Antimicrobial phenolic compounds from three Spanish Helichrysum species', *Phytochemistry*, vol. 29, no. 4, pp. 1093–1095, Jan. 1990, doi: 10.1016/0031-9422(90)85410-H.

[132] J. B. Sindambiwe *et al.*, 'Screening of seven selected Rwandan medicinal plants for antimicrobial and antiviral activities', *Journal of Ethnopharmacology*, vol. 65, no. 1, pp. 71–77, Apr. 1999, doi: 10.1016/S0378-8741(98)00154-8.

[133] N. Lall, A. A. Hussein, and J. J. M. Meyer, 'Antiviral and antituberculous activity of Helichrysum melanacme constituents', *Fitoterapia*, vol. 77, no. 3, pp. 230–232, Apr. 2006, doi: 10.1016/j.fitote.2006.01.007.

[134] I. Kutluk, M. Aslan, I. E. Orhan, and B. Özçelik, 'Antibacterial, antifungal and antiviral bioactivities of selected Helichrysum species', *South African Journal of Botany*, vol. 119, pp. 252–257, Nov. 2018, doi: 10.1016/j.sajb.2018.09.009.

[135] I. Mucsi, Z. Gyulai, and I. Béládi, 'Combined effects of flavonoids and acyclovir against herpesviruses in cell cultures', *Acta Microbiol Hung*, vol. 39, no. 2, pp. 137–147, Jan. 1992.

[136] M. Wleklik, M. Luczak, W. Panasiak, M. Kobus, and E. Lammer-Zarawska, 'Structural basis for antiviral activity of flavonoids-naturally occurring compounds', *Acta Virol*, vol. 32, no. 6, pp. 522–525, Nov. 1988.

[137] F. Piras, V. Sogos, F. Pollastro, G. Appendino, and A. Rosa, 'Arzanol, a natural phloroglucinol α-pyrone, protects HaCaT keratinocytes against H_2 O_2 -induced oxidative stress, counteracting cytotoxicity, reactive oxygen species generation, apoptosis, and mitochondrial depolarization', *J of Applied Toxicology*, vol. 44, no. 5, pp. 720–732, May 2024, doi: 10.1002/jat.4570.

[138] K. Kramberger, Priprava in biološki učinki tradicionalnih pripravkov iz smilja *(Helichrysum italicum)* na model črevesnih celičnih linij, vol. 2023.

[139] E. Mrhar, 'Optimisation of the cultivation process and evaluation of the antiviral activity of compounds on model viruses', Master's thesis, University in Ljubljana, Biotechnical Faculty, Ljubljana, 2025.

[140] W. Earle, 'Production of Malignancy in Vitro. IV. The Mouse Fibroblast Cultures and Changes Seen in the Living Cells', *JNCI: Journal of the National Cancer Institute*, Oct. 1943, doi: 10.1093/jnci/4.2.165.

[141] R. I. Freshney, *Culture of Animal Cells: A Manual of Basic Technique and Specialized Applications*, 7. Auflage. New York, NY: John Wiley & Sons, 2016.

[142] *Biological evaluation of medical devices – Part 5: Tests for in vitro cytotoxicity*, ISO 10993-5, 2009.

[143] J. Hou *et al.*, 'Antiviral activity of PHA767491 against human herpes simplex virus in vitro and in vivo', *BMC Infect Dis*, vol. 17, no. 1, p. 217, Dec. 2017, doi: 10.1186/s12879-017-2305-0.

[144] W. C. Raschke, S. Baird, P. Ralph, and I. Nakoinz, 'Functional macrophage cell lines transformed by abelson leukemia virus', *Cell*, vol. 15, no. 1, pp. 261–267, Sep. 1978, doi: 10.1016/0092-8674(78)90101-0.

[145] D. M. Mosser and J. P. Edwards, 'Exploring the full spectrum of macrophage activation', *Nat Rev Immunol*, vol. 8, no. 12, pp. 958–969, Dec. 2008, doi: 10.1038/nri2448.

[146] M. Pope *et al.*, 'Resistance to Murine Hepatitis Virus Strain 3 Is Dependent on Production of Nitric Oxide', *Journal of Virology*, vol. 72, no. 9, pp. 7084–7090, Sep. 1998, doi: 10.1128/jvi.72.9.7084-7090.1998.

[147] T. Kitamoto *et al.*, 'Viral Population Changes during Murine Norovirus Propagation in RAW 264.7 Cells', *Front. Microbiol.*, vol. 8, Jun. 2017, doi: 10.3389/fmicb.2017.01091.

[148] Y. Yasumura and Y. Kawakita, 'Studies on SV40 in tissue culture – preliminary step for cancer research "in vitro"', *Nihon Rinsho*, vol. 1963, no. 21, pp. 1201–1215, 1963.

[149] J. M. Emeny and M. J. Morgan, 'Regulation of the Interferon System: Evidence that Vero Cells have a Genetic Defect in Interferon Production', *Journal of General Virology*, vol. 43, no. 1, pp. 247–252, Apr. 1979, doi: 10.1099/0022-1317-43-1-247.

[150] J. Harcourt *et al.*, 'Severe Acute Respiratory Syndrome Coronavirus 2 from Patient with Coronavirus Disease, United States', *Emerg. Infect. Dis.*, vol. 26, no. 6, pp. 1266–1273, Jun. 2020, doi: 10.3201/eid2606.200516.

[151] S. Rottem and M. F. Barile, 'Beware of mycoplasmas', *Trends Biotechnol*, vol. 11, no. 4, pp. 143–151, Apr. 1993, doi: 10.1016/0167-7799(93)90089-R.

[152] S. Razin, D. Yogev, and Y. Naot, 'Molecular Biology and Pathogenicity of Mycoplasmas', *Microbiol Mol Biol Rev*, vol. 62, no. 4, pp. 1094–1156, Dec. 1998, doi: 10.1128/mmbr.62.4.1094-1156.1998.

[153] S. R. Weiss and J. L. Leibowitz, 'Coronavirus Pathogenesis', in *Advances in Virus Research*, vol. 81, Elsevier, 2011, pp. 85–164. doi: 10.1016/B978-0-12-385885-6.00009-2.

[154] P. S. Masters, 'The Molecular Biology of Coronaviruses', in *Advances in Virus Research*, vol. 66, Elsevier, 2006, pp. 193–292. doi: 10.1016/S0065-3527(06)66005-3.

[155] F.-Y. Nan, C.-J. Wu, J.-H. Su, and L.-Q. Ma, 'Potential mouse models of coronavirus-related immune injury', *Front. Immunol.*, vol. 13, p. 943783, Sep. 2022, doi: 10.3389/fimmu.2022.943783.

[156] Z. Zhao *et al.*, 'Glycyrrhizic Acid Nanoparticles as Antiviral and Anti-inflammatory Agents for COVID-19 Treatment', *ACS Appl. Mater. Interfaces*, vol. 13, no. 18, pp. 20995–21006, May 2021, doi: 10.1021/acsami.1c02755.

[157] R. Burrer *et al.*, 'Antiviral Effects of Antisense Morpholino Oligomers in Murine Coronavirus Infection Models', *J Virol*, vol. 81, no. 11, pp. 5637–5648, Jun. 2007, doi: 10.1128/JVI.02360-06.

[158] S. M. Karst, C. E. Wobus, M. Lay, J. Davidson, and H. W. Virgin, 'STAT1-Dependent Innate Immunity to a Norwalk-Like Virus', *Science*, vol. 299, no. 5612, pp. 1575–1578, Mar. 2003, doi: 10.1126/science.1077905.

[159] C. E. Wobus *et al.*, 'Replication of Norovirus in Cell Culture Reveals a Tropism for Dendritic Cells and Macrophages', *PLoS Biol*, vol. 2, no. 12, p. e432, Nov. 2004, doi: 10.1371/journal.pbio.0020432.

[160] J. L. Cannon, E. Papafragkou, G. W. Park, J. Osborne, L.-A. Jaykus, and J. Vinjé, 'Surrogates for the Study of Norovirus Stability and Inactivation in the Environment: A Comparison of Murine Norovirus and Feline Calicivirus', *Journal of Food Protection*, vol. 69, no. 11, pp. 2761–2765, Nov. 2006, doi: 10.4315/0362-028X-69.11.2761.

[161] D. M. Knipe and P. M. Howley, *Fields' Virology*. Lippincott Williams & Wilkins, 2007.

[162] A. M. Munis, E. M. Bentley, and Y. Takeuchi, 'A tool with many applications: vesicular stomatitis virus in research and medicine', *Expert Opinion on Biological Therapy*, vol. 20, no. 10, pp. 1187–1201, Oct. 2020, doi: 10.1080/14712598.2020.1787981.

[163] R. Blumenthal, A. Bali-Puri, A. Walter, D. Covell, and O. Eidelman, 'pH-dependent fusion of vesicular stomatitis virus with Vero cells. Measurement by dequenching of octadecyl rhodamine fluorescence.', *Journal of Biological Chemistry*, vol. 262, no. 28, pp. 13614–13619, Oct. 1987, doi: 10.1016/S0021-9258(19)76472-2.

[164] Q. Shao, J. Huang, and J. Li, 'Intracellular Replication Inhibitory Effects of Tea Tree Oil on Vesicular Stomatitis Virus and Anti-inflammatory Activities in Vero Cells', *Front Vet Sci*, vol. 8, p. 759812, Nov. 2021, doi: 10.3389/fvets.2021.759812.

[165] M. Kamil Hussain, M. Saquib, and M. Faheem Khan, 'Techniques for Extraction, Isolation, and Standardization of Bio-active Compounds from Medicinal Plants', in *Natural Bio-active Compounds*, M. K. Swamy and M. S. Akhtar, Eds, Singapore: Springer Singapore, 2019, pp. 179–200. doi: 10.1007/978-981-13-7205-6_8.

[166] A. Meden *et al.*, 'Tryptophan-derived butyrylcholinesterase inhibitors as promising leads against Alzheimer's disease', *Chem. Commun.*, vol. 55, no. 26, pp. 3765–3768, 2019, doi: 10.1039/C9CC01330J.

[167] L. J. Reed and H. Muench, 'A SIMPLE METHOD OF ESTIMATING FIFTY PER CENT ENDPOINTS12', *American Journal of Epidemiology*, vol. 27, no. 3, pp. 493–497, May 1938, doi: 10.1093/oxfordjournals.aje.a118408.

[168] E. Y. Gong, Ed., *Antiviral Methods and Protocols*, vol. 1030. in Methods in Molecular Biology, vol. 1030. Totowa, NJ: Humana Press, 2013. doi: 10.1007/978-1-62703-484-5.

[169] N. Kobe *et al.*, '*In silico* characterisation of a novel SARS-CoV-2 envelope protein inhibitor and *in vitro* validation against murine coronavirus', *Bioorganic Chemistry*, vol. 178, p. 109949, Aug. 2026, doi: 10.1016/j.bioorg.2026.109949.

[170] T. Zamljen, R. Veberic, and M. C. Grohar, 'Impact of salinity and harvest date on the yield, phenolic and volatile contents of thyme (Thymus vulgaris L.), coriander (Coriandrum sativum L.) and dill (Anethum graveolens L.)', *Scientia Horticulturae*, vol. 352, p. 114445, Oct. 2025, doi: 10.1016/j.scienta.2025.114445.

[171] D. G. Besselsen, A. M. Wagner, and J. K. Loganbill, 'Detection of Rodent Coronaviruses by Use of Fluorogenic Reverse Transcriptase-Polymerase Chain Reaction Analysis', *Comparative Medicine*, vol. 52, no. 2, pp. 111–116, 2002.

[172] D. Dobnik *et al.*, 'Accurate Quantification and Characterization of Adeno-Associated Viral Vectors', *Front. Microbiol.*, vol. 10, p. 1570, Jul. 2019, doi: 10.3389/fmicb.2019.01570.

[173] T. Sterling and J. J. Irwin, 'ZINC 15 – Ligand Discovery for Everyone', *J. Chem. Inf. Model.*, vol. 55, no. 11, pp. 2324–2337, Nov. 2015, doi: 10.1021/acs.jcim.5b00559.

[174] U. Grošelj and Č. Podlipnik, 'FKKTLib'. Accessed: Dec. 11, 2025. [Online]. Available: https://knjiznica-spojin.fkkt.uni-lj.si/si/index.html

[175] G. Madhavi Sastry, M. Adzhigirey, T. Day, R. Annabhimoju, and W. Sherman, 'Protein and ligand preparation: parameters, protocols, and influence on virtual screening enrichments', *J Comput Aided Mol Des*, vol. 27, no. 3, pp. 221–234, Mar. 2013, doi: 10.1007/s10822-013-9644-8.

[176] *Schrödinger Release 2024-4*. (2024). Schrödinger LLC, New York, NY.

[177] C. A. Lipinski, F. Lombardo, B. W. Dominy, and P. J. Feeney, 'Experimental and computational approaches to estimate solubility and permeability in drug discovery and development settings', *Advanced Drug Delivery Reviews*, vol. 23, no. 1–3, pp. 3–25, Jan. 1997, doi: 10.1016/S0169-409X(96)00423-1.

[178] D. F. Veber, S. R. Johnson, H.-Y. Cheng, B. R. Smith, K. W. Ward, and K. D. Kopple, 'Molecular Properties That Influence the Oral Bioavailability of Drug Candidates', *J. Med. Chem.*, vol. 45, no. 12, pp. 2615–2623, Jun. 2002, doi: 10.1021/jm020017n.

[179] J. B. Baell and G. A. Holloway, 'New Substructure Filters for Removal of Pan Assay Interference Compounds (PAINS) from Screening Libraries and for Their Exclusion in Bioassays', *J. Med. Chem.*, vol. 53, no. 7, pp. 2719–2740, Apr. 2010, doi: 10.1021/jm901137j.

[180] W. P. Walters and M. Namchuk, 'Designing screens: how to make your hits a hit', *Nat Rev Drug Discov*, vol. 2, no. 4, pp. 259–266, Apr. 2003, doi: 10.1038/nrd1063.

[181] N. Nikitina, M. Manzyuk, Č. Podlipnik, and M. Jukić, 'Performance Estimation of a BOINC-Based Desktop Grid for Large-Scale Molecular Docking', in *Parallel Computing*

Technologies, vol. 12942, V. Malyshkin, Ed., in Lecture Notes in Computer Science, vol. 12942. , Cham: Springer International Publishing, 2021, pp. 348–356. doi: 10.1007/978-3-030-86359-3_26.

[182] N. Nikitina, M. Manzyuk, M. Jukić, Č. Podlipnik, I. Kurochkin, and A. Albertian, 'Toward Crowdsourced Drug Discovery: Start-Up of the Volunteer Computing Project SiDock@home', in *Supercomputing*, vol. 1510, V. Voevodin and S. Sobolev, Eds, in Communications in Computer and Information Science, vol. 1510. , Cham: Springer International Publishing, 2021, pp. 513–524. doi: 10.1007/978-3-030-92864-3_39.

[183] 'Schrödinger LLC. Schrödinger Release 2024-4: Glide. New York, NY. 2024. Software version 2024-4.'

[184] E. Chovancova *et al.*, 'CAVER 3.0: A Tool for the Analysis of Transport Pathways in Dynamic Protein Structures', *PLoS Comput Biol*, vol. 8, no. 10, p. e1002708, Oct. 2012, doi: 10.1371/journal.pcbi.1002708.

[185] S. Jo, T. Kim, V. G. Iyer, and W. Im, 'CHARMM-GUI: A web-based graphical user interface for CHARMM', *J Comput Chem*, vol. 29, no. 11, pp. 1859–1865, Aug. 2008, doi: 10.1002/jcc.20945.

[186] J. Lee, X. Cheng, S. Jo, A. D. MacKerell, J. B. Klauda, and W. Im, 'CHARMM-GUI Input Generator for NAMD, Gromacs, Amber, Openmm, and CHARMM/OpenMM Simulations using the CHARMM36 Additive Force Field', *Biophysical Journal*, vol. 110, no. 3, p. 641a, Feb. 2016, doi: 10.1016/j.bpj.2015.11.3431.

[187] E. L. Wu *et al.*, 'CHARMM-GUI *Membrane Builder* toward realistic biological membrane simulations', *J. Comput. Chem.*, vol. 35, no. 27, pp. 1997–2004, Oct. 2014, doi: 10.1002/jcc.23702.

[188] S. Jo, J. B. Lim, J. B. Klauda, and W. Im, 'CHARMM-GUI Membrane Builder for Mixed Bilayers and Its Application to Yeast Membranes', *Biophysical Journal*, vol. 97, no. 1, pp. 50–58, Jul. 2009, doi: 10.1016/j.bpj.2009.04.013.

[189] S. Jo, T. Kim, and W. Im, 'Automated Builder and Database of Protein/Membrane Complexes for Molecular Dynamics Simulations', *PLoS ONE*, vol. 2, no. 9, p. e880, Sep. 2007, doi: 10.1371/journal.pone.0000880.

[190] S. Park, Y. K. Choi, S. Kim, J. Lee, and W. Im, 'CHARMM-GUI Membrane Builder for Lipid Nanoparticles with Ionizable Cationic Lipids and PEGylated Lipids', *J. Chem. Inf. Model.*, vol. 61, no. 10, pp. 5192–5202, Oct. 2021, doi: 10.1021/acs.jcim.1c00770.

[191] J. B. Klauda *et al.*, 'Update of the CHARMM All-Atom Additive Force Field for Lipids: Validation on Six Lipid Types', *J. Phys. Chem. B*, vol. 114, no. 23, pp. 7830–7843, Jun. 2010, doi: 10.1021/jp101759q.

[192] R. M. Venable *et al.*, 'CHARMM All-Atom Additive Force Field for Sphingomyelin: Elucidation of Hydrogen Bonding and of Positive Curvature', *Biophysical Journal*, vol. 107, no. 1, pp. 134–145, Jul. 2014, doi: 10.1016/j.bpj.2014.05.034.

[193] B. R. Brooks *et al.*, 'CHARMM: The biomolecular simulation program', *J Comput Chem*, vol. 30, no. 10, pp. 1545–1614, Jul. 2009, doi: 10.1002/jcc.21287.

[194] J. Lee, M. Hitzenberger, M. Rieger, N. R. Kern, M. Zacharias, and W. Im, 'CHARMM-GUI supports the Amber force fields', *The Journal of Chemical Physics*, vol. 153, no. 3, p. 035103, Jul. 2020, doi: 10.1063/5.0012280.

[195] C. J. Dickson, R. C. Walker, and I. R. Gould, 'Lipid21: Complex Lipid Membrane Simulations with AMBER', *J. Chem. Theory Comput.*, vol. 18, no. 3, pp. 1726–1736, Mar. 2022, doi: 10.1021/acs.jctc.1c01217.

[196] 'Case DA, Aktulga HM, Belfon K, Ben-Shalom I, Brozell SR, Cerutti DS, et al. Amber 2021. San Francisco: University of California; 2021.'

[197] D. A. Case *et al.*, 'AmberTools', *J. Chem. Inf. Model.*, vol. 63, no. 20, pp. 6183–6191, Oct. 2023, doi: 10.1021/acs.jcim.3c01153.

[198] M. S. Valdés-Tresanco, M. E. Valdés-Tresanco, P. A. Valiente, and E. Moreno, 'gmx_MMPBSA: A New Tool to Perform End-State Free Energy Calculations with GROMACS', *J. Chem. Theory Comput.*, vol. 17, no. 10, pp. 6281–6291, Oct. 2021, doi: 10.1021/acs.jctc.1c00645.

[199] I. F. De Castro, L. Volonté, and C. Risco, 'Virus factories: biogenesis and structural design: Biogenesis and architecture of virus factories', *Cell Microbiol*, vol. 15, no. 1, pp. 24–34, Jan. 2013, doi: 10.1111/cmi.12029.

[200] S. Eymieux *et al.*, 'Ultrastructural modifications induced by SARS-CoV-2 in Vero cells: a kinetic analysis of viral factory formation, viral particle morphogenesis and virion release', *Cell. Mol. Life Sci.*, vol. 78, no. 7, pp. 3565–3576, Apr. 2021, doi: 10.1007/s00018-020-03745-y.

[201] M. M. Angelini, M. Akhlaghpour, B. W. Neuman, and M. J. Buchmeier, 'Severe Acute Respiratory Syndrome Coronavirus Nonstructural Proteins 3, 4, and 6 Induce Double-Membrane Vesicles', *mBio*, vol. 4, no. 4, pp. e00524-13, Aug. 2013, doi: 10.1128/mbio.00524-13.

[202] D. Oudshoorn *et al.*, 'Expression and Cleavage of Middle East Respiratory Syndrome Coronavirus nsp3-4 Polyprotein Induce the Formation of Double-Membrane Vesicles That Mimic Those Associated with Coronaviral RNA Replication', *mBio*, vol. 8, no. 6, pp. e01658-17, Dec. 2017, doi: 10.1128/mbio.01658-17.

[203] H. M. N. Al-Mulla *et al.*, 'Competitive Fitness in Coronaviruses Is Not Correlated with Size or Number of Double-Membrane Vesicles under Reduced-Temperature Growth Conditions', *mBio*, vol. 5, no. 2, pp. e01107–e01113, May 2014, doi: 10.1128/mbio.01107-13.

[204] S. Stertz *et al.*, 'The intracellular sites of early replication and budding of SARS-coronavirus', *Virology*, vol. 361, no. 2, pp. 304–315, May 2007, doi: 10.1016/j.virol.2006.11.027.

[205] R. Gosert, A. Kanjanahaluethai, D. Egger, K. Bienz, and S. C. Baker, 'RNA Replication of Mouse Hepatitis Virus Takes Place at Double-Membrane Vesicles', *J Virol*, vol. 76, no. 8, pp. 3697–3708, Apr. 2002, doi: 10.1128/JVI.76.8.3697-3708.2002.

[206] H. J. Maier *et al.*, 'Extensive coronavirus-induced membrane rearrangements are not a determinant of pathogenicity', *Sci Rep*, vol. 6, no. 1, p. 27126, Jun. 2016, doi: 10.1038/srep27126.

[207] K. Knoops *et al.*, 'SARS-Coronavirus Replication Is Supported by a Reticulovesicular Network of Modified Endoplasmic Reticulum', *PLoS Biol*, vol. 6, no. 9, p. e226, Sep. 2008, doi: 10.1371/journal.pbio.0060226.

[208] R. Jaiswal, H. Müller, A. Müller, M. G. E. Karar, and N. Kuhnert, 'Identification and characterization of chlorogenic acids, chlorogenic acid glycosides and flavonoids from Lonicera henryi L. (Caprifoliaceae) leaves by LC–MS', *Phytochemistry*, vol. 108, pp. 252–263, Dec. 2014, doi: 10.1016/j.phytochem.2014.08.023.

[209] M. N. Clifford, K. L. Johnston, S. Knight, and N. Kuhnert, 'Hierarchical Scheme for LC-MS ^{n} Identification of Chlorogenic Acids', *J. Agric. Food Chem.*, vol. 51, no. 10, pp. 2900–2911, May 2003, doi: 10.1021/jf026187q.

[210] A. Vallverdú-Queralt, O. Jáuregui, G. Di Lecce, C. Andrés-Lacueva, and R. M. Lamuela-Raventós, 'Screening of the polyphenol content of tomato-based products through accurate-mass spectrometry (HPLC–ESI-QTOF)', *Food Chemistry*, vol. 129, no. 3, pp. 877–883, Dec. 2011, doi: 10.1016/j.foodchem.2011.05.038.

[211] M. Gil and D. Wianowska, 'Chlorogenic acids – their properties, occurrence and analysis', *aa*, vol. 72, no. 1, p. 61, Dec. 2017, doi: 10.17951/aa.2017.72.1.61.

[212] M. N. Clifford, S. Knight, and N. Kuhnert, 'Discriminating between the Six Isomers of Dicaffeoylquinic Acid by LC-MS ^{n} ', *J. Agric. Food Chem.*, vol. 53, no. 10, pp. 3821–3832, May 2005, doi: 10.1021/jf050046h.

[213] S. Gonçalves, E. Moreira, C. Grosso, P. B. Andrade, P. Valentão, and A. Romano, 'Phenolic profile, antioxidant activity and enzyme inhibitory activities of extracts from aromatic plants used in Mediterranean diet', *J Food Sci Technol*, vol. 54, no. 1, pp. 219–227, Jan. 2017, doi: 10.1007/s13197-016-2453-z.

[214] N. Kłeczek, B. Michalak, J. Malarz, A. K. Kiss, and A. Stojakowska, 'Carpesium divaricatum Sieb. & Zucc. Revisited: Newly Identified Constituents from Aerial Parts of the Plant and Their Possible Contribution to the Biological Activity of the Plant', *Molecules*, vol. 24, no. 8, p. 1614, Apr. 2019, doi: 10.3390/molecules24081614.

[215] M. Takenaka, X. Yan, H. Ono, M. Yoshida, T. Nagata, and T. Nakanishi, 'Caffeic Acid Derivatives in the Roots of Yacon (*Smallanthus sonchifolius*)', *J. Agric. Food Chem.*, vol. 51, no. 3, pp. 793–796, Jan. 2003, doi: 10.1021/jf020735i.

[216] R. Gevrenova *et al.*, 'Phytochemical Profiling, Antioxidant and Cognitive-Enhancing Effect of Helichrysum italicum ssp. italicum (Roth) G. Don (Asteraceae)', *Plants*, vol. 12, no. 15, Jul. 2023, doi: 10.3390/plants12152755.

[217] J. Kaur, V. Dhiman, S. Bhadada, O. Katare, and G. Ghoshal, 'LC/MS guided identification of metabolites of different extracts of Cissus quadrangularis', *Food Chemistry Advances*, vol. 1, p. 100084, Oct. 2022, doi: 10.1016/j.focha.2022.100084.

[218] S. Podder, A. Ghosh, and T. Ghosh, 'Mutations in membrane-fusion subunit of spike glycoprotein play crucial role in the recent outbreak of COVID-19', *Journal of Medical Virology*, vol. 93, no. 5, pp. 2790–2798, May 2021, doi: 10.1002/jmv.26598.

[219] S. Zhou *et al.*, 'SARS-CoV-2 E protein: Pathogenesis and potential therapeutic development', *Biomedicine & Pharmacotherapy*, vol. 159, p. 114242, Mar. 2023, doi: 10.1016/j.biopha.2023.114242.

[220] X. Jing *et al.*, 'Functional studies indicate amantadine binds to the pore of the influenza A virus M2 proton-selective ion channel', *Proc. Natl. Acad. Sci. U.S.A.*, vol. 105, no. 31, pp. 10967–10972, Aug. 2008, doi: 10.1073/pnas.0804958105.

[221] C. Wang, K. Takeuchi, L. H. Pinto, and R. A. Lamb, 'Ion channel activity of influenza A virus M2 protein: characterization of the amantadine block', *J Virol*, vol. 67, no. 9, pp. 5585–5594, Sep. 1993, doi: 10.1128/jvi.67.9.5585-5594.1993.

[222] R. A. Bright *et al.*, 'Incidence of adamantane resistance among influenza A (H3N2) viruses isolated worldwide from 1994 to 2005: a cause for concern', *The Lancet*, vol. 366, no. 9492, pp. 1175–1181, Oct. 2005, doi: 10.1016/S0140-6736(05)67338-2.

[223] G. E. Aranda-Abreu, J. D. Aranda-Martínez, R. Araújo, M. E. Hernández-Aguilar, D. Herrera-Covarrubias, and F. Rojas-Durán, 'Observational study of people infected with SARS-Cov-2, treated with amantadine', *Pharmacol. Rep*, vol. 72, no. 6, pp. 1538–1541, Dec. 2020, doi: 10.1007/s43440-020-00168-1.

[224] K. Rejdak and P. Grieb, 'Adamantanes might be protective from COVID-19 in patients with neurological diseases: multiple sclerosis, parkinsonism and cognitive impairment', *Multiple Sclerosis and Related Disorders*, vol. 42, p. 102163, Jul. 2020, doi: 10.1016/j.msard.2020.102163.

[225] J. Mancilla-Galindo *et al.*, 'All-cause mortality among patients treated with repurposed antivirals and antibiotics for COVID-19 in Mexico City: A real-world observational study', *EXCLI Journal; 20:Doc199; ISSN 1611-2156*, 2021, doi: 10.17179/EXCLI2021-3413.

[226] C. Verdiá-Báguena *et al.*, 'Coronavirus E protein forms ion channels with functionally and structurally-involved membrane lipids', *Virology*, vol. 432, no. 2, pp. 485–494, Oct. 2012, doi: 10.1016/j.virol.2012.07.005.

[227] J. Torres, U. Maheswari, K. Parthasarathy, L. Ng, D. X. Liu, and X. Gong, 'Conductance and amantadine binding of a pore formed by a lysine-flanked transmembrane domain of SARS coronavirus envelope protein', *Protein Science*, vol. 16, no. 9, pp. 2065–2071, Sep. 2007, doi: 10.1110/ps.062730007.

[228] D. Schoeman and B. C. Fielding, 'Coronavirus envelope protein: current knowledge', *Virol J*, vol. 16, no. 1, p. 69, Dec. 2019, doi: 10.1186/s12985-019-1182-0.

[229] E. Steinmann, F. Penin, S. Kallis, A. H. Patel, R. Bartenschlager, and T. Pietschmann, 'Hepatitis C Virus p7 Protein Is Crucial for Assembly and Release of Infectious Virions', *PLoS Pathog*, vol. 3, no. 7, p. e103, Jul. 2007, doi: 10.1371/journal.ppat.0030103.

[230] M. J. Sarmento *et al.*, 'The expanding organelle lipidomes: current knowledge and challenges', *Cell. Mol. Life Sci.*, vol. 80, no. 8, p. 237, Aug. 2023, doi: 10.1007/s00018-023-04889-3.

[231] F. Chen *et al.*, 'In vitro susceptibility of 10 clinical isolates of SARS coronavirus to selected antiviral compounds', *Journal of Clinical Virology*, vol. 31, no. 1, pp. 69–75, Sep. 2004, doi: 10.1016/j.jcv.2004.03.003.

[232] U. Breitinger, N. S. Farag, N. K. M. Ali, M. Ahmed, M. A. El-Azizi, and H.-G. Breitinger, 'Cell viability assay as a tool to study activity and inhibition of hepatitis C p7 channels', *Journal of General Virology*, vol. 102, no. 3, Mar. 2021, doi: 10.1099/jgv.0.001571.

[233] S. Griffin, C. StGelais, A. M. Owsianka, A. H. Patel, D. Rowlands, and M. Harris, 'Genotype-dependent sensitivity of hepatitis C virus to inhibitors of the p7 ion channel', *Hepatology*, vol. 48, no. 6, pp. 1779–1790, Dec. 2008, doi: 10.1002/hep.22555.

[234] M. L. DeDiego *et al.*, 'A Severe Acute Respiratory Syndrome Coronavirus That Lacks the E Gene Is Attenuated In Vitro and In Vivo', *J Virol*, vol. 81, no. 4, pp. 1701–1713, Feb. 2007, doi: 10.1128/JVI.01467-06.

[235] J. M. Jimenez-Guardeño *et al.*, 'The PDZ-Binding Motif of Severe Acute Respiratory Syndrome Coronavirus Envelope Protein Is a Determinant of Viral Pathogenesis', *PLoS Pathog*, vol. 10, no. 8, p. e1004320, Aug. 2014, doi: 10.1371/journal.ppat.1004320.

[236] F. Alvarez *et al.*, 'The SARS-CoV-2 envelope PDZ binding motif acts as a virulence factor disrupting host's epithelial cell–cell junctions', *Cell Mol Biol Lett*, vol. 30, no. 1, p. 80, Jul. 2025, doi: 10.1186/s11658-025-00758-y.

[237] J. Ortego, J. E. Ceriani, C. Patiño, J. Plana, and L. Enjuanes, 'Absence of E protein arrests transmissible gastroenteritis coronavirus maturation in the secretory pathway', *Virology*, vol. 368, no. 2, pp. 296–308, Nov. 2007, doi: 10.1016/j.virol.2007.05.032.

[238] K. Miura *et al.*, 'Distinct motifs in the E protein are required for SARS-CoV-2 virus particle formation and lysosomal deacidification in host cells', *J Virol*, vol. 97, no. 10, pp. e00426-23, Oct. 2023, doi: 10.1128/jvi.00426-23.

[239] G. J. Pearson, H. V. Mears, M. Broncel, A. P. Snijders, D. L. V. Bauer, and J. G. Carlton, 'ER-export and ARFRP1/AP-1–dependent delivery of SARS-CoV-2 Envelope to lysosomes controls late stages of viral replication', *Sci. Adv.*, vol. 10, no. 14, p. eadl5012, Apr. 2024, doi: 10.1126/sciadv.adl5012.

[240] W.-A. Wang, A. Carreras-Sureda, and N. Demaurex, 'SARS-CoV-2 infection alkalinizes the ERGIC and lysosomes through the viroporin activity of the viral envelope protein', *Journal of Cell Science*, vol. 136, no. 6, p. jcs260685, Mar. 2023, doi: 10.1242/jcs.260685.

[241] S. Ghosh *et al.*, 'β-Coronaviruses Use Lysosomes for Egress Instead of the Biosynthetic Secretory Pathway', *Cell*, vol. 183, no. 6, pp. 1520-1535.e14, Dec. 2020, doi: 10.1016/j.cell.2020.10.039.

[242] P. Baudoux, C. Carrat, L. Besnardeau, B. Charley, and H. Laude, 'Coronavirus Pseudoparticles Formed with Recombinant M and E Proteins Induce Alpha Interferon Synthesis by Leukocytes', *J. Virol.*, vol. 72, no. 11, pp. 8636–8643, Nov. 1998, doi: 10.1128/JVI.72.11.8636-8643.1998.

[243] J. Maeda, A. Maeda, and S. Makino, 'Release of Coronavirus E Protein in Membrane Vesicles from Virus-Infected Cells and E Protein-Expressing Cells', *Virology*, vol. 263, no. 2, pp. 265–272, Oct. 1999, doi: 10.1006/viro.1999.9955.

[244] E. Corse and C. E. Machamer, 'Infectious Bronchitis Virus E Protein Is Targeted to the Golgi Complex and Directs Release of Virus-Like Particles', *J Virol*, vol. 74, no. 9, pp. 4319–4326, May 2000, doi: 10.1128/JVI.74.9.4319-4326.2000.

[245] A. L. Potter *et al.*, 'Deaths Due to COVID-19 in Patients With Cancer During Different Waves of the Pandemic in the US', *JAMA Oncol*, vol. 9, no. 10, p. 1417, Oct. 2023, doi: 10.1001/jamaoncol.2023.3066.

[246] N. L. Harrison *et al.*, 'How many SARS-CoV-2 "viroporins" are really ion channels?', *Commun Biol*, vol. 5, no. 1, p. 859, Aug. 2022, doi: 10.1038/s42003-022-03669-2.

[247] L. Hok, H. Rimac, J. Mavri, and R. Vianello, 'COVID-19 infection and neurodegeneration: Computational evidence for interactions between the SARS-CoV-2 spike protein and monoamine oxidase enzymes', *Computational and Structural Biotechnology Journal*, vol. 20, pp. 1254–1263, 2022, doi: 10.1016/j.csbj.2022.02.020.

[248] J. H. Meyer *et al.*, 'Elevated Monoamine Oxidase A Levels in the Brain: An Explanation for the Monoamine Imbalance of Major Depression', *Arch Gen Psychiatry*, vol. 63, no. 11, p. 1209, Nov. 2006, doi: 10.1001/archpsyc.63.11.1209.

[249] Y. Santin, J. Resta, A. Parini, and J. Mialet-Perez, 'Monoamine oxidases in age-associated diseases: New perspectives for old enzymes', *Ageing Research Reviews*, vol. 66, p. 101256, Mar. 2021, doi: 10.1016/j.arr.2021.101256.

[250] M. Pavlin, M. Repič, R. Vianello, and J. Mavri, 'The Chemistry of Neurodegeneration: Kinetic Data and Their Implications', *Mol Neurobiol*, vol. 53, no. 5, pp. 3400–3415, Jul. 2016, doi: 10.1007/s12035-015-9284-1.

[251] P. Riederer and T. Müller, 'Monoamine oxidase-B inhibitors in the treatment of Parkinson's disease: clinical–pharmacological aspects', *J Neural Transm*, vol. 125, no. 11, pp. 1751–1757, Nov. 2018, doi: 10.1007/s00702-018-1876-2.

[252] S. Manzoor and N. Hoda, 'A comprehensive review of monoamine oxidase inhibitors as Anti-Alzheimer's disease agents: A review', *European Journal of Medicinal Chemistry*, vol. 206, p. 112787, Nov. 2020, doi: 10.1016/j.ejmech.2020.112787.

[253] X. Xia, Y. Wang, and J. Zheng, 'COVID-19 and Alzheimer's disease: how one crisis worsens the other', *Transl Neurodegener*, vol. 10, no. 1, p. 15, Dec. 2021, doi: 10.1186/s40035-021-00237-2.

[254] B. Berta *et al.*, 'SARS-CoV-2 envelope protein alters calcium signaling via SERCA interactions', *Sci Rep*, vol. 14, no. 1, p. 21200, Sep. 2024, doi: 10.1038/s41598-024-71144-5.

[255] C. Duque-Soto, A. Ruiz-Vargas, A. Rueda-Robles, R. Quirantes-Piné, I. Borrás-Linares, and J. Lozano-Sánchez, 'Bioactive Potential of Aqueous Phenolic Extracts of Spices for Their Use in the Food Industry—A Systematic Review', *Foods*, vol. 12, no. 16, p. 3031, Aug. 2023, doi: 10.3390/foods12163031.

[256] S. Hapsari, I. Yohed, R. A. Kristianita, N. Jadid, H. W. Aparamarta, and S. Gunawan, 'Phenolic and flavonoid compounds extraction from Calophyllum inophyllum leaves', *Arabian Journal of Chemistry*, vol. 15, no. 3, p. 103666, Mar. 2022, doi: 10.1016/j.arabjc.2021.103666.

[257] K. Chojnacka, D. Skrzypczak, G. Izydorczyk, K. Mikula, D. Szopa, and A. Witek-Krowiak, 'Antiviral Properties of Polyphenols from Plants', *Foods*, vol. 10, no. 10, p. 2277, Sep. 2021, doi: 10.3390/foods10102277.

[258] K. Gescher, A. Hensel, W. Hafezi, A. Derksen, and J. Kühn, 'Oligomeric proanthocyanidins from Rumex acetosa L. inhibit the attachment of herpes simplex virus type-1', *Antiviral Research*, vol. 89, no. 1, pp. 9–18, Jan. 2011, doi: 10.1016/j.antiviral.2010.10.007.

[259] M. F. Montenegro-Landívar *et al.*, 'Polyphenols and their potential role to fight viral diseases: An overview', *Science of The Total Environment*, vol. 801, p. 149719, Dec. 2021, doi: 10.1016/j.scitotenv.2021.149719.

[260] V. R. Kudkyal, I. Matsuura, H. Hiramatsu, K. Hayashi, and T. Kawahara, 'Phenol Derivatives Obtained from Grape Seed Extract Show Virucidal Activity against Murine Norovirus', *Molecules*, vol. 27, no. 22, p. 7739, Nov. 2022, doi: 10.3390/molecules27227739.

[261] C. Oh, R. Chowdhury, L. Samineni, J. L. Shisler, M. Kumar, and T. H. Nguyen, 'Inactivation Mechanism and Efficacy of Grape Seed Extract for Human Norovirus Surrogate', *Applied and Environmental Microbiology*, vol. 88, no. 9, pp. e02247-21, Apr. 2022, doi: 10.1128/aem.02247-21.

[262] K. Ueda, R. Kawabata, T. Irie, Y. Nakai, Y. Tohya, and T. Sakaguchi, 'Inactivation of Pathogenic Viruses by Plant-Derived Tannins: Strong Effects of Extracts from Persimmon (Diospyros kaki) on a Broad Range of Viruses', *PLoS ONE*, vol. 8, no. 1, p. e55343, Jan. 2013, doi: 10.1371/journal.pone.0055343.

[263] M. L. De Pellegrin, A. Rohrhofer, P. Schuster, B. Schmidt, P. Peterburs, and A. Gessner, 'The potential of herbal extracts to inhibit SARS-CoV-2: a pilot study', *Clin Phytosci*, vol. 7, no. 1, p. 29, Mar. 2021, doi: 10.1186/s40816-021-00264-6.

[264] M. Tokusanai *et al.*, 'Prunus mume Extract Inhibits SARS-CoV-2 and Influenza Virus Infection In Vitro by Directly Targeting Viral Particles', *International Journal of Molecular Sciences*, vol. 26, no. 17, p. 8487, Jan. 2025, doi: 10.3390/ijms26178487.

[265] W. Wu *et al.*, 'Quercetin as an Antiviral Agent Inhibits Influenza A Virus (IAV) Entry', *Viruses*, vol. 8, no. 1, p. 6, Dec. 2015, doi: 10.3390/v8010006.

[266] H. J. Choi, J. H. Song, K. S. Park, and D. H. Kwon, 'Inhibitory effects of quercetin 3-rhamnoside on influenza A virus replication', *European Journal of Pharmaceutical Sciences*, vol. 37, no. 3–4, pp. 329–333, Jun. 2009, doi: 10.1016/j.ejps.2009.03.002.

[267] A. Kandeil *et al.*, 'Bioactive Polyphenolic Compounds Showing Strong Antiviral Activities against Severe Acute Respiratory Syndrome Coronavirus 2', *Pathogens*, vol. 10, no. 6, p. 758, Jun. 2021, doi: 10.3390/pathogens10060758.

[268] A. Di Petrillo, G. Orrù, A. Fais, and M. C. Fantini, 'Quercetin and its derivates as antiviral potentials: A comprehensive review', *Phytotherapy Research*, vol. 36, no. 1, pp. 266–278, Jan. 2022, doi: 10.1002/ptr.7309.

[269] G. Derosa, P. Maffioli, A. D'Angelo, and F. Di Pierro, 'A role for quercetin in coronavirus disease 2019 (COVID-19)', *Phytotherapy Research*, vol. 35, no. 3, pp. 1230–1236, Mar. 2021, doi: 10.1002/ptr.6887.

[270] T. L. A. Nguyen and D. Bhattacharya, 'Antimicrobial Activity of Quercetin: An Approach to Its Mechanistic Principle', *Molecules*, vol. 27, no. 8, p. 2494, Apr. 2022, doi: 10.3390/molecules27082494.

[271] K. H. Chiow, M. C. Phoon, T. Putti, B. K. H. Tan, and V. T. Chow, 'Evaluation of antiviral activities of Houttuynia cordata Thunb. extract, quercetin, quercetrin and cinanserin on murine coronavirus and dengue virus infection', *Asian Pacific Journal of Tropical Medicine*, vol. 9, no. 1, pp. 1–7, Jan. 2016, doi: 10.1016/j.apjtm.2015.12.002.

[272] S. Al-Arnoot *et al.*, 'Multitarget Antimicrobial Mechanisms of Plant Extracts: A Review of Harnessing Phytochemicals Against Drug-Resistant Pathogens', *jchm*, vol. 19, no. 4, pp. 292–309, Aug. 2025, doi: 10.59628/jchm.v19i4.1936.

[273] J. Mitrovic, V. Aleksic Sabo, G. Lazic, and P. Knezevic, 'Antiviral activity of selected plant-derived polyphenols against Varicellovirus bovinealpha1 (BoAHV-1)', *AMB Expr*, vol. 15, no. 1, p. 141, Sep. 2025, doi: 10.1186/s13568-025-01945-y.

[274] F. B. Üzer, N. Helvacı, M. Elmastaş, F. B. Üzer, N. Helvacı, and M. Elmastaş, 'Synergistic Phenolic Compounds in Medicinal Plant Extracts: Enhanced Furin Protease Inhibition via Solvent-Specific Extraction from Lamiaceae and Asteraceae Families', *Molecules*, vol. 30, no. 17, Aug. 2025, doi: 10.3390/molecules30173450.

Bibliography

Publications Related to the Thesis

Journal Articles

N. Kobe, L. Dreisewerd, M. Pavlin, P. Kogovšek, Č. Podlipnik, U. Grošelj, and M. Lukšič, "In silico determination of novel SARS-CoV-2 envelope protein ion channel inhibitors," *Computational and Structural Biotechnology Journal*, vol. 27, pp. 2823-2831, 2025.

N. Kobe, L. Dreisewerd, M. Lukšič, M. Pavlin, U. Grošelj, Č. Podlipnik, M. Janc, Ž. Lengar, P. Mrak, M. Tušek Žnidarič, M. Pompe Novak, U. Kuhar, P. Hostnik, F. Dattola, T. Carletti, A. Marcello, and P. Kogovšek, "In silico characterisation of a novel SARS-CoV-2 envelope protein inhibitor and in vitro validation against murine coronavirus," *Bioorganic Chemistry*, vol. 178, p. 109949, 2026.

N. Kobe, E. Mrhar, K. Kramberger, D. Barlič-Maganja, T. Zamljen, R. Veberič, F. Dattola, T. Carletti, A. Marcello, and P. Kogovšek, "Antiviral potential of Helichrysum italicum ethanolic extract and phenolic constituents against murine coronavirus in vitro," *Journal of Ethnopharmacology*, Under review. 2026

Other Publications

E. Mrhar, "Optimisation of the cultivation process and evaluation of the antiviral activity of compounds on model viruses, " Biotechnical Faculty, University of Ljubljana, Slovenia, 2025.

Biography

Nina Kobe was born in Novo mesto, Slovenia, in 1995. She obtained her BSc in Cosmetology from the Faculty of Pharmacy (UL FFA), University of Ljubljana in 2018 and her MSc in Biochemistry from the Faculty of Chemistry and Chemical Technology (UL FKKT), University of Ljubljana in 2021. Her BSc thesis, which she carried out in cooperation with the Blood Transfusion Centre of Slovenia under the supervision of Prof Dr Matjaž Jeras and Dr Urška Rahne Potokar, focused on immunology and medicine. In her MSc thesis, which she carried out at the NIB under the supervision of Prof Dr Kristina Gruden, she investigated the immune response of plants. In 2021, she joined NIB as a young researcher under the supervision of Dr Polona Kogovšek and enrolled in the PhD programme Nanosciences and Nanotechnologies at the Jožef Stefan International Postgraduate School. Her research focused on antiviral strategies against mammalian viruses, including SARS-CoV-2 and murine hepatitis virus (MHV). She established a cell virology laboratory and developed *in vitro* platforms for evaluating the antiviral activity of compounds from diverse origins, complemented by *in silico* approaches for the identification of novel antiviral agents. She collaborated closely with the Faculty of Chemistry and Chemical Technology (Ljubljana), the Faculty of Biotechnology (Ljubljana), the Faculty of Health Sciences (Izola), and the Veterinary Faculty (Ljubljana). In 2025, she completed an Erasmus internship at the International Centre for Genetic Engineering and Biotechnology (ICGEB) in Trieste, where she gained advanced expertise in antiviral research. She was also a working mentor to a master's student who completed her thesis. She has presented her work at international conferences and is actively engaged in science communication.